eXPRESS Polymer Letters Vol.8, No.10 (2014) 708
Available online at www.expresspolymlett.com
DOI: 10.3144/expresspolymlett.2014.73

Editorial corner – a personal view
Mechanochemical synthesis and modification of polymers

Gy. Bánhegyi[*]

Department of Advanced Materials and Processes Institute for Materials Science and Technology, Bay Zoltán Nonprofit Ltd. for Applied Research, Fehérvári út 130., H-1116 Budapest, Hungary

Polymers are usually synthesized in gas and liquid phases by polymerization, polycondensation, polyaddition. There have been extensive attempts at solid state polymerization induced by various kinds of irradiation, but the differences in lattice symmetry usually prevented the direct formation of crystalline polymers from monomers. Mechanochemical synthesis became a common route in inorganic solid state chemistry.

Recent publications (see e.g. DOI: 10.1021/mz500098r, DOI: 10.6000/1927-5951.2014.04.01.6) show, that ball milling can also be used for direct polymer synthesis and not only for the uniform distribution of fillers in a polymer matrix (see e.g. DOI: 10.1177/0731684412471230, DOI: 10.1002/app.35413) or for coating inorganic nano particles (DOI: 10.1016/j.powtec.2010.11.011, DOI: 10.1039/C1JM10819K).

In some cases embedding into a polymer goes parallel with ion doping (see e.g. DOI: 10.1021/am4056672, where Li doped Si is combined with poly-para-phenylene polymer for Li batteries). Mechanochemistry can be well utilized for the polymer-analog modification of already existing polymers (see e.g. DOI: 10.1021/cg500439f) or for block-polymerization (DOI: 10.1155/2014/127506). The mechanism of the latter is not much different from that used in compatibilization by reactive extrusion: radicals recombine with each other.

The advantage of the mechanochemical route is the reduced solvent consumption, or complete elimination of the solvent (environmentally benign processes, 'green chemistry'), parallel processes (breakdown of particles, surface grafting, embedding, polymerization, block-copolymer formation, compatibilization) may proceed and the specific energy can be very high. The resurgence of the interest in mechanochemical methods is partly due to their applicability in waste disposal and recycling (DOI: 10.1016/j.wasman.2009.08.017). Harmful chemicals may be mechanically degraded into less harmful products, partial network degradation of rubbers (DOI: 10.4028/www.scientific.net/AMR.239-242.2503) and thermoset polymers (DOI: 10.2417/spepro.005351, DOI: 10.4028/www.scientific.net/AMM.130-134.1708) can be achieved. Surface activation and treatment are performed simultaneously, which allows the production of active fillers from the otherwise intractable thermoset composite waste. Another aim is the wider utilization of natural polymers (DOI: 10.1039/B108255H, DOI: 10.1155/2013/425726), and even the synthesis of biomimetic polymers (DOI: 10.1038/nchem.1938). For the above reasons I foresee and expect an increased research and development activity in the field of mechanical synthesis and modification of polymers.

Dr. György Bánhegyi
Member of Executive Editorial Board

[*]Corresponding author, e-mail: gybanheg@t-online.hu

eXPRESS Polymer Letters Vol.8, No.10 (2014) 709–722
Available online at www.expresspolymlett.com
DOI: 10.3144/expresspolymlett.2014.74

New poly(*p*-phenylenevinylene) derivatives containing isosorbide unit in the side-chain

H. Zrida[1], *K. Hriz*[1], *N. Jaballah*[1], *N. Sakly*[1], *D. Kreher*[2], *M. Majdoub*[1*]

[1]Laboratoire des Interfaces et des Matériaux Avancés (LIMA), Faculté des Sciences de Monastir, Bd. de l'Environnement, 5019 Monastir, Université de Monastir, Tunisia
[2]Laboratoire de Chimie des polymères Université Pierre et Marie-Currie (UPMC), 4 Place Jussieu, 75005 Paris, France

Received 10 March 2014; accepted in revised form 18 May 2014

Abstract. New conjugated PPV derivatives containing the chiral isosorbide group (**P1-3**) have been synthesized via the Gilch reaction. The polymers are optically active, soluble in common organic solvents and show good film-forming abilities. High number-average molecular weights were determined by size exclusion chromatography (SEC) ($16 \cdot 10^3$–$21 \cdot 10^3$ g·mol^{-1}). The molecular structures of the polymers were confirmed by nuclear magnetic resonance (NMR) and Fourier transform infrared (FTIR) spectroscopies. Thermogravimetric analysis of the polymers showed good thermal stability up to 320°C. The optical properties of these π-conjugated materials were investigated by UV-vis absorption and photoluminescence (PL) spectroscopies. The polymers show a yellow fluorescence in dilute solution, and an orange emission is observed in thin films. The introduction of the polar isosorbide groups improved the PL intensity, and quantum yields between 50 and 73% were obtained. The HOMO-LUMO energy levels were estimated by cyclic voltammetry, and the electrochemical gaps were 1.81, 1.83 and 2.48 eV for **P1**, **P2** and **P3**, respectively. Single-layer diode devices were fabricated and show relatively low turn-on voltages between 3.1 and 3.4 V.

Keywords: *polymer synthesis, optically active polymers, semi-conducting polymers, isosorbide, photoluminescence*

1. Introduction

The discovery of electroluminescence in poly (*p*-phenylenevinylene) (PPV) in 1990 [1] created a new domain in polymeric material applications. Since then, enormous progress has been made in the macromolecular engineering of the π-conjugated polymers and in their uses as active materials in polymeric light-emitting diodes (PLEDs) [2–6]. These polymers are promising organic analogues of inorganic semi-conducting materials, and their exploitation in other electronic devices, such as thin-film transistors [7, 8], photovoltaic cells [9, 10], chemical sensors [11] and organic lasers [12] are currently expanding. The main advantages of using such functional polymers lie in their low production cost and easy processibility. In fact, these materials are compatible with solution processing techniques, thus eliminating the vacuum deposition steps usually required for the elaboration of inorganic semi-conducting thin layers. Solution processing also expands the repertoire of tolerant substrates and processing options, allowing flexible plastics to be used in combination with relatively simple methods such as spin coating and inkjet printing. Though, the major characteristic of the semi-conducting polymers is their adjustable macormolecular structure and consequently there tuneable opto-electronic properties [13–16].

Among π-conjugated polymers, the poly (*p*-phenylenevinylene) (PPV) and its derivatives are the most studied and exploited [17, 18]. Due to the high rigidity of the macromolecular structure, PPV is

*Corresponding author, e-mail: mustapha.majdoub@fsm.rnu.tn

insoluble in common organic solvents. This intractability has been addressed by chemically attaching aliphatic side-chains to the polymer backbone [19]. Hence, many PPV-type architectures are processed in a derivative form. The effects of the side-group structure on the opto-electronic properties have been extensively investigated [20]. However, most studies have involved nonpolar side-chains, and the effect of relatively polar side-groups was rarely reported (e.g PPV derivative containing ethylene oxide-type side chains) [12]. Here, we report the first PPV derivatives containing the polar and chiral isosorbide groups. In fact, the incorporation of chiral groups in polypyrroles and polythiophenes was reported. These groups confer original physico-chemical properties to the polymer [21–23]. Therefore, these optically active polymers were used to prepare chiral electrodes for asymmetric electrosynthesis, polarization-sensitive electro-optical devices, polarized photo- and electroluminescent devices and enantioselective sensors [24]. Herein, we present the synthesis and structural characterizations of the isosorbide-containing PPVs; the thermal, thin film surface, optical and electrochemical properties were investigated.

2. Experimental

2.1. Materials and measurements

The poly (2-hexyloxy-5-methoxy-*p*-phenylenevinylene) (**MH-PPV**) was synthesized by using Gilch condensation. Detailed synthesis procedure can be found elsewhere [20]. Isosorbide (98%, Acros Organics, France), 4-toluenesulfonyl chloride (98%, Sigma-Aldrich, France), 4-methoxyphenol (99%, Acros Organics, France), ethyl bromide (98%, Acros Organics, France), hexyl bromide (98%, Acros Organics, France), dodecyl bromide (98%, Acros Organics, France), potassium carbonate (99%, Acros Organics, France), potassium *tert*-butoxide (98%, Acros Organics, France), *t*-butanol (Acros Organics, France), sodium hydride (60% dispersion in mineral oil, Sigma-Aldrich, France), paraformaldehyde (96%, Acros Organics, France), sodium (Sigma Aldrich, France) and dimethylformamide (DMF) (Acros Organics, France) were used as received. Ethanol was dried over Mg/I_2 and freshly distilled before use. All the solvents used in this study were purchased from Sigma-Aldrich (France). Optical rotations were measured with Atago Polax-2L digital polarimeter (Atago, Japan). ^{1}H-NMR and ^{13}C-NMR spectral data were obtained on a Bruker AV 300 spectrometer (Biospin, Strasbourg, France). Fourier transform infrared (FTIR) spectra were acquired on a Perkin-Elmer BX FTIR (Perkin-Elmer, California, USA) system spectrometer by dispersing samples in KBr disks. Size exclusion chromatography (SEC) was performed on an Agilent Technologies 1200 HPLC (Agilent, France). The experiment was done at room temperature using THF as eluent with standard polystyrene calibration. Thermogravimetric analysis (TGA) was carried out on TA Instruments Q50 (TA Instruments, USA) under nitrogen at a heating rate of $10°C \cdot min^{-1}$. DSC was performed on a Mettler Toledo DSC1(Mettler Toledo, France) with a heating rate of $10°C \cdot min^{-1}$. UV-vis absorption spectra were recorded on a Cary 300 spectrophotometer (Agilent, France). Fluorescence spectra were obtained on a Jobin-Yvon spectrometer HR460 (HORIB, Kyoto, Japan) coupled to a nitrogen-cooled Si charged-coupled device (CCD). Samples were excited at 365 nm with a 450 W xenon lamp. The spectral sensitivity of the measurement system was calibrated using tungsten standard lamp. The PL quantum yields were measured in dilute chloroform solution according to a relative method using quinine sulfate (Sigma-Aldrich, France) (10^{-5} M solution of 0.5 H_2SO_4) [25]. Absorbance of the sample solutions was kept below 0.05 to avoid inner filter effect, and measurements were performed at room temperature using freshly prepared solutions. Both sample and reference solutions were excited at the same wavelength (365 nm), and the PL quantum efficiency of the quinine sulfate solution (Φ_r) was assumed to be 0.54 [26]. Hence, the PL quantum efficiency of the sample (Φ_s) can be calculated using Equation (1):

$$\frac{\Phi_s}{\Phi_r} = \frac{A_r}{A_s}\frac{F_s}{F_r}\frac{n_s^2}{n_r^2} \tag{1}$$

where A_r and F_r are the absorbance at the excitation wavelength and emission integration area for the reference, A_s and F_s are the absorbance and emission integral for the sample, while n_s and n_r are the refractive index of the polymer solution and quinine sulfate solution, respectively. For solid state optical measurements, the film was spin-coated onto a quartz substrate from 50 μL of a chloroform solution ($2 \cdot 10^{-2}$ M). The film thicknesses were measured by a Dektak profilometer (Sloan, USA) and were about 60 nm. Film thickness was controlled

by spinning rate to obtain comparable thicknesses and so similar refractive indices. Thus, the ratio of PL quantum yields of three film samples can be calculated according to Equation (2):

$$\frac{\Phi_s}{\Phi_r} = \frac{A_r}{A_s}\frac{F_s}{F_r} \quad (2)$$

The atomic force microscopy (AFM) analyses of the polymer coated glass surfaces were carried out using a Nanoscope III (Digital Instruments, Santa Barbara, CA) operating in the tapping mode. Contact angle measurements with three different liquids (DI water, formamide and diiodomethane) were performed with Digidrop (GBX, France) contact angle instrument. Every reported contact angle measurement represents an average value of at least three separated drops on different areas of the given wafer. The size and volume of the drops were kept constant. Cyclic voltammetry (CV) was performed on a CHI 660B electrochemical station (CH Instruments Inc., USA) in a three-electrode cell and using material films that were drop-cast onto an indium tin oxide (ITO/1 cm^2) working electrode. The measurements were carried out at a scanning rate of 50 $mV \cdot s^{-1}$ against an Ag/AgCl reference electrode, a counter electrode made with a Platinum wire (1 cm of length) using 0.1 M tetrabutylammoniumfluoroborate ($(n\text{-}Bu)_4NBF_4$) in acetonitrile as supporting electrolyte. The electrochemical cell was externally calibrated by ferrocene under the same conditions as the polymers. The measurements were performed at 25°C, and the cell was deoxygenated with argon before each reductive scan.

2.2. Synthesis of the monomers (e1-3)

Synthesis of 2,5-O-ditosyl-1,4:3,6-dianhydro-D-sorbitol **(a)**

120 mL of 5 M aqueous NaOH was added to 100 mL of 2 M isosorbide/THF solution. The mixture was cooled to 5°C. A solution of 4-toluenesulfonyl chloride (0.38 mol) in 100 mL of THF was added dropwise. After 2 h, the mixture was placed in a separating funnel and the phases were separated. The aqueous phase was extracted with dichloromethane (3×50 mL). The organic phases were combined and washed with water, dried over $MgSO_4$ and the solvent was evaporated. The product was obtained as a white solid. M.p: 98°C; yield: 95%; ^{1}H-NMR (300 MHz, $CDCl_3$, δ): 7.80–7.74 (m, 4H, Ar–H), 7.36–7.27 (m, 4H, Ar–H), 4.87–4.83 (m, 2H, H_2, H_5), 4.61 (m, 1H, H_3), 4.46 (d, J = 3 Hz, 1H, H_4), 3.96–3.80 (m, 3H, $H_1{}^b$, $H_6{}^a$, $H_6{}^b$), 3.65 (m, 1H, $H_1{}^a$), 2.46 (s, 6H, $SO_2C_6H_4CH_3$); ^{13}C-NMR (75.5 MHz, $CDCl_3$, δ): 144.80, 133.74, 129.90, 127.48, 84.50, 82.8, 83.70, 80.5, 73.30, 71.20, 21.62.

Synthesis of 1,4:3,6-dianhydro-5-[4-methoxyphenyloxy]-2-O-tosyl-5-deoxy-L-iditol **(b)**

A mixture of 4-methoxyphenol (10 mmol), potassium carbonate (10 mmol) and 2,5-O-ditosyl-1,4:3,6-dianhydro-D-sorbitol **(a)** (10 mmol) was stirred in 20 mL of DMF at 60°C. After 24 h the reaction mixture was poured into distilled water and extracted with dichloromethane. The extract was washed with distilled water, dried over anhydrous $MgSO_4$ and concentrated at reduced pressure. The resultant crude product was purified by recrystallization from chloroform/ethanol (1:5 v/v). The product is obtained as a white powder. M.p: 91°C; yield: 60%; ^{1}H-NMR (300 MHz, $CDCl_3$, δ): 7.82 (d, J = 9.0 Hz, 2H, Ar–H), 7.39 (d, J = 9.0 Hz, 2H, Ar–H), 6.83 (s, 4H, Ar–H), 4.94 (d, J = 3 Hz, 1H, H_2), 4.74–4.67 (m, 3H, H_3, H_4, H_5), 4.04–3.88 (m, 4H, $H_1{}^b$, $H_1{}^a$, $H_6{}^b$, $H_6{}^a$), 3.77 (s, 3H, OCH_3), 2.47 (s, 3H, CH_3); ^{13}C-NMR (75 MHz, $CDCl_3$, δ): 152.59, 148.78, 143.53, 128.25, 126.01, 114.60, 112.93, 83.49, 83.41, 81.09, 79.52, 70.67, 70.28, 53.83, 19.86.

Synthesis of 1,4:3,6-dianhydro-5-[4-methoxyphenyloxy]-5-deoxy-L-iditol **(c)**

The 1,4:3,6-dianhydro-5-[4-methoxyphenyloxy]-2-O-tosyl-5-deoxy-L-iditol **(b)** (10 mmol) was refluxed with sodium ethoxide in ethanol (1 M) for 4 h. After cooling to room temperature, the solution was concentrated. The residue was then poured into distilled water and extracted with dichloromethane. The organic layer was washed several times with distilled water and dried over anhydrous $MgSO_4$. The product was recuperated as a white powder by precipitation in petroleum ether. M.p: 82°C; yield 85%; ^{1}H-NMR (300 MHz, $CDCl_3$, δ): 6.90–6.82 (m, 4H, Ar–H), 4.78 (d, J = 3.9 Hz, 1H, H_5), 4.71 (m, 1H, H_4), 4.62 (d, J = 3.6 Hz, 1H, H_3), 4.36 (m, 1H, H_2), 4.05–3.89 (m, 4H, $H_1{}^a$, $H_1{}^b$, $H_6{}^a$, $H_6{}^b$), 3.77 (s, 3H, OCH_3), 2.5 (s, 1H, OH); ^{13}C-NMR (75 MHz, $CDCl_3$, δ): 154.33, 150.92, 116.48, 114.80, 87.88, 85.12, 81.73, 75.92, 74.49, 72.29, 55.71; FTIR (cm^{-1}): 3400 (w, C–H, stretching).

Synthesis of the 1,4:3,6-dianhydro-2-O-alkyl-5-[4-methoxyphenyloxy]-5-deoxy-L-iditols **(d1-3)**

A solution of 1,4:3,6-dianhydro-5-[4-methoxyphenyloxy]-5-deoxy-L-iditol **(c)** (10 mmol) in 10 mL of dry DMF was added dropwise under argon to a suspension of NaH (15 mmol) of a 60% dispersion in mineral oil; washed with hexane) in 10 mL of dry DMF. After stirring for 30 minutes at 0°C, a 12 mmol of alkyl bromide was added. The reaction mixture was stirred for 24 h at room temperature. The resulting mixture was then poured into distilled water and extracted with dichloromethane. The organic layer was washed several times with distilled water, then dried over anhydrous $MgSO_4$ and evaporated. The resultant crude product was purified by column chromatography with cyclohexane/ethyl acetate (90:10: v/v).

d1: R = ethyl; aspect: colorless oil; yield: 89%; ^{1}H-NMR (300 MHz, DMSO, δ): 6.90–6.88 (m, 4H, Ar–H), 4.73 (m, 1H, H_5), 4.58 (d, J = 6 Hz, 1H, H_4), 4.51 (d, J = 6 Hz, 1H, H_3), 3.95–3.78 (m, 5H, H_2, $H_1{}^a$, $H_1{}^b$, $H_6{}^a$, $H_6{}^b$), 3.70 (s, 3H, OCH_3), 3.53 (m, 2H, –OCH_2), 1.12 (t, J = 6 Hz, 3H, CH_3); ^{13}C-NMR (75 MHz, DMSO, δ): 153.83, 150.54, 116.47, 114.71, 85.18, 84.86, 82.63, 81.39, 71.57, 71.28, 64.06, 55.29, 15.11.

d2: R = hexyl; aspect colorless oil; yield: 85%. ^{1}H-NMR (300 MHz, $CDCl_3$, δ): 6.91–6.83 (m, 4H, Ar–H), 4.72–4.67 (m, 3H, H_3, H_4, H_5), 4.03–3.90 (m, 5H, $H_1{}^a$, $H_1{}^b$, $H_6{}^a$, $H_6{}^b$, H_2), 3.78 (s, 3H, OCH_3), 3.52 (td, ^{4}J = 3 Hz, ^{3}J = 9 Hz, 2H, –OCH_2), 1.63 (m, 2H, OCH_2–CH_2–CH_2), 1.36–1.30 (m, 6H, –$(CH_2)_3$–CH_3), 0.92 (t, J = 7.8 Hz, 3H, –CH_3); ^{13}C-NMR (75 MHz, $CDCl_3$, δ): 154.56, 151.29, 116.64, 115, 85.98, 85.56, 83.68, 82.06, 72.62, 72.39, 70.12, 55.89, 31.80, 29.90, 25.93, 22.76, 14.19.

d3: R = dodecyl; aspect: white solid. M.p.: 41°C; yield: 75%; ^{1}H-NMR (300 MHz, $CDCl_3$, δ): 6.91–6.83 (m, 4H, Ar–H), 4.72–4.67 (m, 3H, H_3, H_4, H_5), 4.03–3.91 (m, 5H, $H_1{}^a$, $H_1{}^b$, $H_6{}^a$, $H_6{}^b$, H_2), 3.78 (s, 3H, OCH_3), 3.54 (td, ^{4}J = 5.4 Hz, ^{3}J = 9 Hz, 2H, OCH_2), 1.57 (m, 2H, OCH_2–CH_2), 1.27 (m, 18H, –$(CH_2)_9$–CH_3), 0.92 (t, J = 6 Hz, 3H, CH_3); ^{13}C-NMR (75 MHz, $CDCl_3$, δ): 153.85, 150.58, 115.94, 114.31, 85.27, 84.85, 82.98, 81.35, 71.94, 71.70, 69.45, 55.20, 31.40, 29.24, 29.13, 29.11, 29.08, 29.05, 28.91, 28.83, 25.57, 22.17, 13.59.

Synthesis of the dichloromethyl aromatic derivatives **(e1-3)**

A mixture of the corresponding 1,4:3,6-dianhydro-2-O-alkyl-5-[4-methoxyphenyloxy]-5-deoxy-L-iditols **(d1-3)** (10 mmol), paraformaldehyde (15 mmol) and 37% aqueous HCl (16 mmol) in acetic acid was stirred at 60°C. The progress of the reaction was monitored by TLC (R = ethyl, hexyl or dodecyl; eluent: cyclohexane/acetate 6/1 v/v). The resulting mixture was then poured into distilled water and extracted with dichloromethane. The organic layer was washed several times with distilled water, then dried over anhydrous $MgSO_4$ and concentrated at reduced pressure. The resultant crude product was purified by recrystallization from an appropriate solvent.

e1: R = ethyl; recrystallization from dichloromethane/ethanol (1:5 v/v); aspect: white solid; yield: 85%; m.p.: 98°C; $[\alpha]_D$ = 42.5° (2, $CHCl_3$); ^{1}H-NMR (300 MHz, $CDCl_3$, δ): 7.01 (s, 1H, Ar–H), 6.94 (s, 1H, Ar–H), 4.82 (m, 1H, H_5), 4.76–4.72 (m, 2H, H_3, H_4), 4.67–4.57 (m, 4H, CH_2–Cl), 4.05–3.88 (m, 8H, $H_1{}^a$, $H_1{}^b$, $H_6{}^a$, $H_6{}^b$, H_2, OCH_3), 3.53 (m, 2H, OCH_2), 1.25 (t, J = 6.9 Hz, 3H, CH_3); ^{13}C-NMR (75 MHz, $CDCl_3$, δ): 151.82, 148.37, 127.96, 127.17, 115.55, 113.45, 85.85, 85.25, 83.26, 82.23, 72.51, 72.06, 65.18, 56.21, 41.06, 41.02, 15.28; FTIR (cm^{-1}): 670 (s, C–Cl stretching).

e2: R = hexyl; recrystallization from dichloromethane/ethanol (1:5 v/v); aspect: white solid; yield: 80%; m.p.: 70°C; $[\alpha]_D$ = 47.5° (2, $CHCl_3$); ^{1}H-NMR (300 MHz, $CDCl_3$, δ): 7.01 (s, 1H, Ar–H), 6.94 (s, 1H, Ar–H), 4.81 (m, 1H, H_5), 4.75–4.71 (m, 2H, H_3, H_4), 4.63 (s, 4H, CH_2–Cl), 4.08–3.87 (m, 8H, $H_1{}^a$, $H_1{}^b$, $H_6{}^a$, $H_6{}^b$, H_2, OCH_3), 3.55 (td, ^{4}J = 5.4 Hz, ^{3}J = 8.7 Hz, 2H, OCH_2), 1.60 (m, 2H, OCH_2–CH_2–CH_2), 1.39–1.30 (m, 6H, –$(CH_2)_3$–CH_3), 0.91 (t, J = 7.8 Hz, 3H, –CH_3); ^{13}C-NMR (75 MHz, $CDCl_3$, δ): 152.02, 148.59, 128.18, 127.38, 115.79, 113.66, 86.05, 85.47, 83.63, 82.49, 72.71, 72.26, 70.18, 56.41, 41.23, 31.80, 29.90, 25.93, 22.76, 14.19; FTIR (cm^{-1}): 672 (s, C–Cl stretching).

e3: R = dodecyl; recrystallization from chloroform/ethanol (1:5 v/v); aspect: white solid; yield: 75%; mp: 86°C; $[\alpha]_D$ = 49° (2, $CHCl_3$); ^{1}H-NMR (300 MHz, $CDCl_3$, δ): 7.01 (s, 1H, Ar–H), 6.94 (s, 1H, Ar–H), 4.82 (m, 1H, H_5), 4.73–4.71 (m, 2H, H_3, H_4), 4.64 (s,

4H, –CH_2Cl), 4.06–3.91 (m, 5H, H_1^a, H_1^b, H_6^a, H_6^b, H_2), 3.88 (s, 3H, OCH_3), 3.54 (td, ^4J = 5.4 Hz, ^3J = 8.7 Hz, 2H, OCH_2), 1.57 (m, 2H, OCH_2–CH_2–CH_2), 1.27 (m, 18H, –$(CH_2)_9$–CH_3), 0.92 (t, J = 6 Hz, 3H, CH_3); ^{13}C-NMR (75.5 MHz, $CDCl_3$, δ): 151.83, 148.39, 127.98, 127.18, 115.58, 113.44, 85.86, 85.27, 83.42, 82.28, 72.51, 72.06, 70, 56.21, 41.05, 41.01, 31.90, 29.74, 29.63, 29.61, 29.58, 29.55, 29.42, 29.33, 26.07, 22.67, 14.09; FTIR (cm^{-1}): 671 (s, C–Cl stretching).

2.3. Synthesis of the polymers (P1-3)

The corresponding dichloromethyl derivative (**e1-3**) (5 mmol) was dissolved in DMF (50 mL) under argon at room temperature. To the obtained solution was slowly added 27 mL of potassium *tert*-butoxide (0.75 M, in *t*-butanol). After 40 h, a second fraction (13.5 mL) of the base was gradually added while heating to 100°C. After 10 h, the resulting reaction mixture was cooled and 50 mL of methanol was added. The obtained precipitate was then filtered and dried under vacuum. Further purification of the polymer was carried out by two precipitations in methanol from chloroform solution.

P1: R = ethyl; aspect: red powder; yield: 50%; $[\alpha]_D$ = –2850° (0.23, $CHCl_3$); ^{1}H-NMR (300 MHz, $CDCl_3$, δ): 7.47–6.69 (m, aromatic and vinylic H), 4.9 (m, H_5, H_4, H_3), 4.15–3.97 (m, H_1^a, H_1^b, H_6^a, H_6^b, H_2, OCH_3), 3.59 (m, OCH_2), 1.23 (m, CH_3); ^{13}C-NMR (75.5 MHz, $CDCl_3$, δ): 152.36, 148.93, 127.42, 124.20, 123.47, 112.98, 109.23, 85.95, 85.66, 83.45, 77, 72.45, 71.93, 65.13, 56.32, 15.31; FTIR (cm^{-1}): 3062 (w, aromatic and vinylic C–H stretching), 2938, 2867 (w, aliphatic C–H stretching), 1650, 1560, 1505 (m, C=C stretching), 1243, 1198 (s, C–O–C asymmetric stretching), 1070 (m, C–O–C symmetric stretching), 962 (m, *E*–HC=CH out-of-plane bending), 790 (s, aromatic C–H out-of-plane bending).

P2: R = hexyl; aspect: red powder; yield: 51%; $[\alpha]_D$ = –3000° (0.15, $CHCl_3$); ^{1}H-NMR (300 MHz, $CDCl_3$, δ): 7.47–7.17(m, aromatic and vinylic H), 4.89 (m, H_5, H_4, H_3), 4.15–3.96 (m, H_1^a, H_1^b, H_6^a, H_6^b, H_2, OCH_3), 3.54–3.50 (m, OCH_2), 1.58–1.31 (m, –$(CH_2)_3$–CH_2), 0.9 (m, CH_3); ^{13}C-NMR (75.5 MHz, $CDCl_3$, δ): 152.46, 149, 123.97, 85.93, 85.67, 83.62, 77.42, 72.43, 71.98, 69.94, 56.28, 31.91, 29.76, 25.75, 22.67, 14.18; FTIR (cm^{-1}): 3061 (w, aromatic and vinylic C–H stretching), 2920, 2856 (w, aliphatic C–H stretching), 1510, 1467, 1412 (m, C=C stretching), 1254, 1205 (s, C–O–C asymmetric stretching), 1093 (m, C–O–C symmetric stretching), 964 (m, *E*–HC=CH out-of-plane bending), 783 (s, aromatic C–H out-of-plane bending).

P3: R = dodecyl; aspect: red powder; yield: 55%; $[\alpha]_D$ = –3500° (0.12, $CHCl_3$); ^{1}H-NMR (300 MHz, $CDCl_3$, δ): 7.39–7.07 (m, aromatic and vinylic H), 4.81 (m, H_5, H_4, H_3), 3.97–3.9 (m, H_1^a, H_1^b, H_6^a, H_6^b, H_2, OCH_3), 3.49–3.42 (m, OCH_2), 1.53–1.09 (m, $(CH_2)_{10}$), 0.81–0.76 (m, CH_3); ^{13}C-NMR (75.5 MHz, $CDCl_3$, δ): 152.36, 148.78, 123.57, 113.02, 109.02, 85.95, 85.59, 83.63, 76.57, 72.43, 72, 69.95, 56.27, 31.90, 29.78, 29.62, 29.47, 29.33, 26.09, 22.67, 14.09; FTIR (cm^{-1}): 3061 (w, aromatic and vinylic C–H stretching), 2920, 2856 (w, aliphatic C–H stretching), 1595, 1510, 1460 (m, C=C stretching), 1254, 1205 (s, C–O–C asymmetric stretching), 1084 (m, C–O–C symmetric stretching), 964 (m, *E*–CH=CH out-of-plane bending), 783 (s, aromatic C–H out-of-plane bending).

2.4. Fabrication and characterization of the diodes

Single-layer devices were elaborated as sandwich structures between an aluminium (Al) cathode and an indium tin oxide (ITO) (ITO-thickness of 100 nm, sheet resistance of 20 Ω/square) anode. Polymer solution ($2 \cdot 10^{-2}$ M in chloroform) was spin-cast (2500 rpm) onto ITO glass to obtain a film about 60 nm thick after annealing at 40°C for 1 h. A thin aluminium layer (150 nm) was deposited by thermal evaporation at $3 \cdot 10^{-6}$ Torr. The current-voltage (I–V) characteristics of the devices were recorded with a Keithley 236 source meter (Keithley, Les Ulis, France).

3. Results and discussion

3.1. Synthesis and characterization

New isosorbide-containing chiral monomers (**e1-3**) were synthesized following a five-step pathway (Figure 1). The 2,5-O-ditosyl-1,4:3,6-dianhydro-D-sorbitol **(a)** was prepared in THF/aqueous NaOH two-phase system, according a previously described procedure [27]. The tosylated isosorbide was treated with methoxyphenol in sodium carbonate/DMF system; thereby, a selective endo-monoalkylated isosorbide derivative **(b)** was obtained. Indeed, the exo position reactivity is limited by the steric hindrance effect [28]. The deprotection of the isosorbide exo hydroxyl group was carried out by sodium ethoxide in ethanol [29]. The obtained derivative

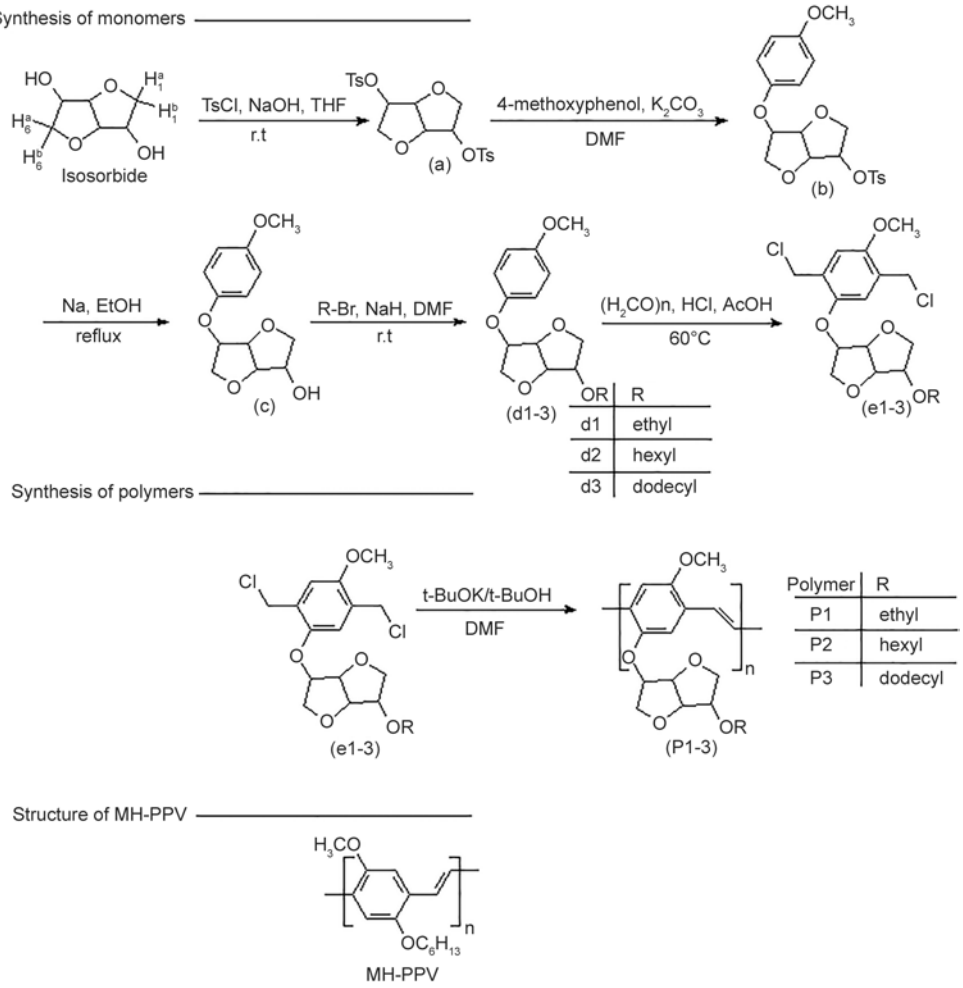

Figure 1. Synthetic route to the monomers and the polymers and macromolecular structure of **MH-PPV**

(c) was then O-alkylated with different aliphatic chain: ethyl, hexyl and dodecyl. The aromatic group of the isosorbide diethers (**d1-3**) was chloromethylated using the HCl/paraformaldehyde/acetic acid system [30] to obtain the corresponding isosorbide-containing monomers (**e1-3**). The PPV polymers (**P1-3**) were synthesized via the Gilch polycondensation of these aromatic dichloromethyl derivatives in DMF and using tert-butoxide as the basic condensing agent [20] (Figure 1). The PPV derivatives are optically active with a specific optical rotation ($[\alpha]_D$) of –2850, –3000 and –3500° for **P1**, **P2** and **P3**, respectively. The polymers were found to have good solubility in common organic solvents such as chloroform, dichloromethane, THF and toluene. The macromolecular structures were confirmed by NMR and FTIR spectroscopic analyses. The ^{1}H-NMR spectra (Figure 2) show a broad peak between 7.4 and 7.1 ppm, wich was assigned to the aromatic and vinylic protons. The CH_2O, CH_3O groups and dianhydro protons appear at the 4.9–3.3 ppm range and the aliphatic groups give rise to a multiplet between 1.6 and 1.1 ppm. For all polymers, the IR spectra (Figure 3) reveal an absorption band centered at 960 cm^{-1} which is assigned to the out-of-plane vibration of the *E*-vinylene groups. The *Z*-vinylene characteristic band (about 860 cm^{-1}) [19, 31] was not observed, indicating a dominant *E* configuration. The number-average molecular weights (M_n) were in the range of 16 000–21 000 g·mol^{-1} and the polydispersity indices (I_p) were between 2.6 and 2.9, as determined by SEC analysis (Table 1). The thermal properties of **P1-3** were investigated by thermogravimetric (TGA) and differential scanning calorimetry (DSC) under ambient atmospheric conditions. The thermograms indicate that the polymers begin to degrade at about 320°C, losing less than 5% of their weight (Figure 4). The major degradation takes place at 375°C; this process corresponds to the decomposition of the side-groups. The **P1-3** showed improved thermal stability, in comparison with the PPV derivatives containing aliphatic side-chains, which decompose below 300°C [32]. This behavior is due to the incor-

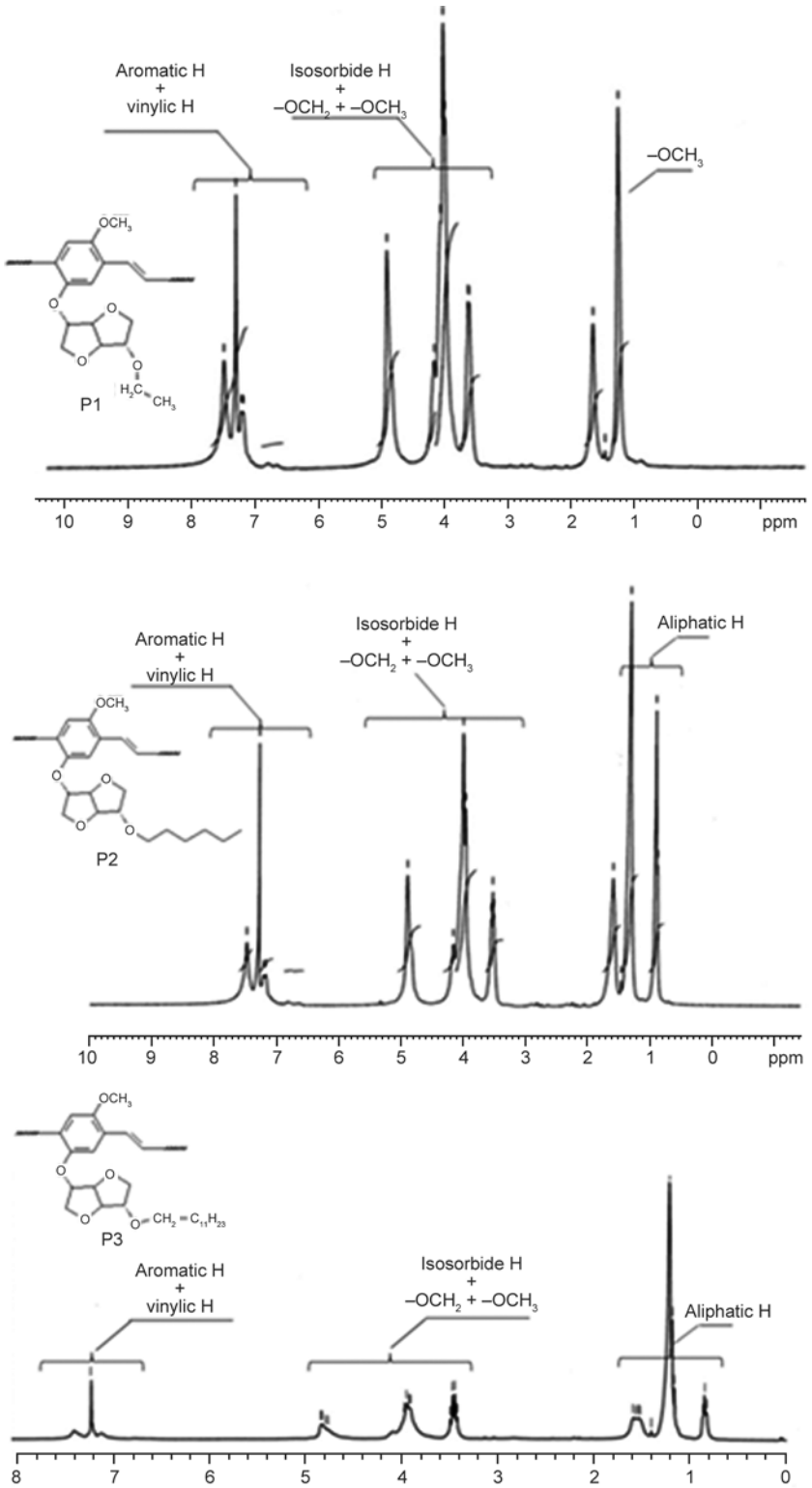

Figure 2. [1]H-NMR spectra of **P1-3**

Table 1. SEC characterizations

Polymer	$\overline{M}_n$ [(a)]	$\overline{M}_w$ [(b)]	I_p [(c)]	$\overline{DP}_n$ [(d)]
P1	16 420	47 770	2.91	54
P2	21 240	56 290	2.65	59
P3	17 760	46 530	2.62	40

[(a)]number average molecular weight; [(b)]weight average molecular weight; [(c)]polydispersity indices; [(d)]number average degree of polymerization.

poration of the rigid and polar isosorbide units in the side-chain. The DSC results indicate a glass transition temperature (T_g) about 75°C for **P1**, 50°C for **P2** and 100°C for **P3**. No melting or other thermal events were observed, which suggested that the polymers were completely amorphous.

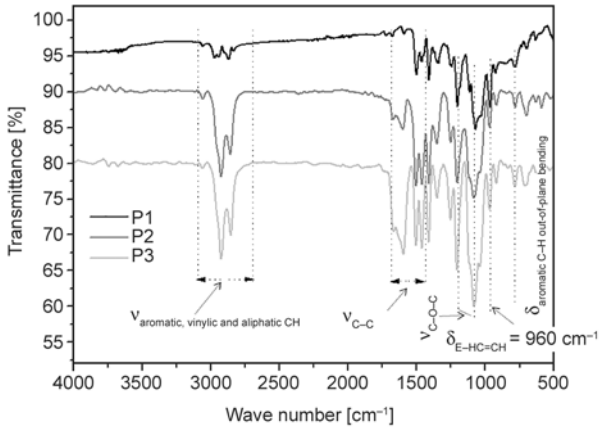

Figure 3. IR spectra of **P1-3**

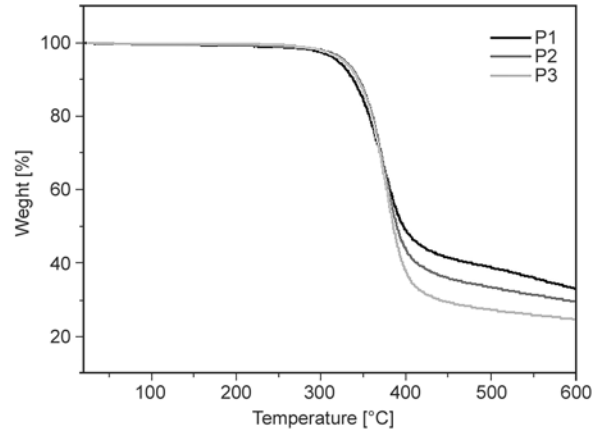

Figure 4. TGA thermograms of **P1-3** (under nitrogen; heating rate:10°C·min^{-1})

3.2. Thin-film surface properties

Polymer films on a glass substrate were prepared and characterized by atomic force microscopy (AFM) (Figure 5). The results show a smooth surface with a root-mean-square (RMS) of 2.5 nm for the dodecyloxy-containing polymer (**P3**). The surface roughness increases with decreasing side chain-length: RMS values of 4.3 and 7.1 nm were found for **P2** and **P1**, respectively. The thin films were also investigated by contact angle measurements, which provide a convenient way to characterize the surface polarity and reflect its functionality [33]. The van Oss-Chaudhury-Good model was exploited, using three test liquids (water, diiodomethane and formamide) [34].

Table 2. Surface characteristics of untreated and **P1-3** treated glass

	γ^+	γ^-	γ^{AB}	γ^{LW}	γ^S
Glass surface	2.0	47.8	19.5	36.7	56.1
P1	0.7	44.6	11.2	42.1	53.6
P2	1.0	26.6	10.3	47.6	57.7
P3	1.8	45.0	18.0	34.1	52.1

γ^+: acid energy component; γ^-: basic energy component ; $\gamma^{AB} = 2(\gamma^+\gamma^-)^{1/2}$: polar energy; γ^{LW}: apolar energy; $\gamma^S = \gamma^{AB} + \gamma^{LW}$: surface energy.

For all polymers, the basic energy component outweighs the acidic aspect, which is due to the presence of oxygen-rich isosorbide units. However, higher polar energy was obtained in the case of **P3** film, indicating a higher isosorbide density in its surface (Table 2).

3.3. Optical properties

The optical absorption and photoluminescence (PL) properties of the polymers were investigated both for chloroform solutions and thin solid films. The concentrations of the chloroform solutions were fixed at $5\cdot10^{-5}$ M in absorption and $2\cdot10^{-7}$ M and in PL. Uniform polymer films were prepared on quartz plates by spin-coating from chloroform solution at room temperature. The absorption and emission data for the polymers are summarized in Table 3.

Table 3. Optical data for **P1-3**

Dilute solution in chloroform							
	Absorption				**Photoluminescence**		
	λ_{max} [nm]	ε_{max} [$10^4\cdot M^{-1}\cdot cm^{-1}$]	FWHM[(b)] [nm]	λ_{onset} [nm]	λ_{max} [nm]	FWHM[(b)] [nm]	Φ_{fl}[(c)]
P1	480	2.38	97	544	543; 582[(a)]	67	0.51
P2	480	1.93	96	542	540; 583[(a)]	69	0.75
P3	470	1.93	109	542	543; 582[(a)]	70	0.73
Thin film							
	Absorption			**Photoluminescence**			
	λ_{max} [nm]	λ_{onset} [nm]	FWHM[(b)] [nm]	λ_{max} [nm]	FWHM[(b)] [nm]	Φ_{fl}[(c)](Pi)/Φ_{fl}[(c)](P1)	
P1	485	585	136	634	113	1.0	
P2	488	593	161	652; 699[(a)]	115	1.3	
P3	479	585	138	671; 697[(a)]	116	1.2	

[(a)]Shoulder, [(b)]Spectrum full width at half maximum, [(c)]PL quantum yields

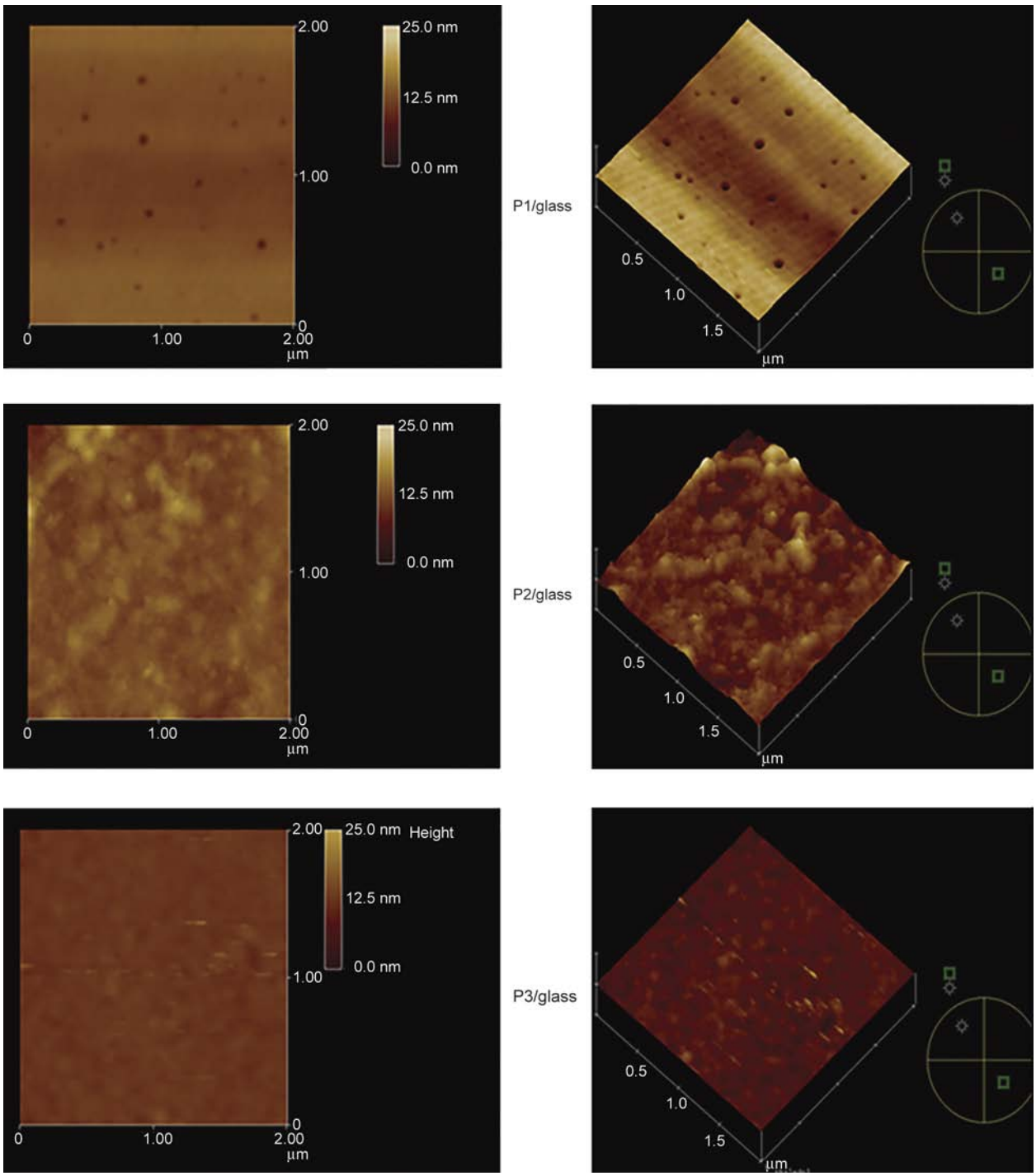

Figure 5. AFM images of [glass/polymer] layers

The absorption and PL spectra of **P1-3** solutions are illustrated in Figure 6. The UV-vis spectra show a similar form with a maximum absorption at 480 nm for **P1** and **P2** and at 470 nm for **P3**. The different behaviors can be explained by the change in the environment surrounding the PPV conjugate systems. Indeed, because **P3** has relatively long dodecyloxy side-chains, the environment of the π-conjugate system is less polar, therefore, its UV-vis absorption is blue-shifted compared to **P1** and **P2**. On the other hand, the spectra of the polymer solutions show the same absorption onset, indicating no effect of the side-group size on the effective conjugation length. The comparison of **P3** with the previously reported PPV derivative containing dodecyloxy side-chain [20] indicates a slight hypsochromic effect (~10 nm). Such behavior is probably due to the steric hindrance of the isosorbide groups, which decrease the planarity of the conjugated system, therefore, reduce the effective conjugation length. The polymer solu-

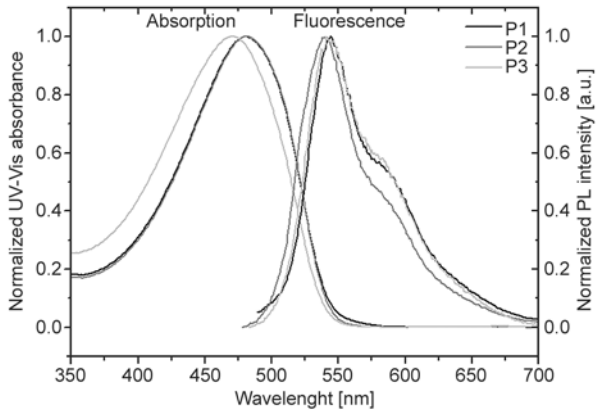

Figure 6. UV-vis absorption and PL spectra of polymers in chloroform ($5 \cdot 10^{-5}$ M in absorption and $2 \cdot 10^{-7}$ M in PL)

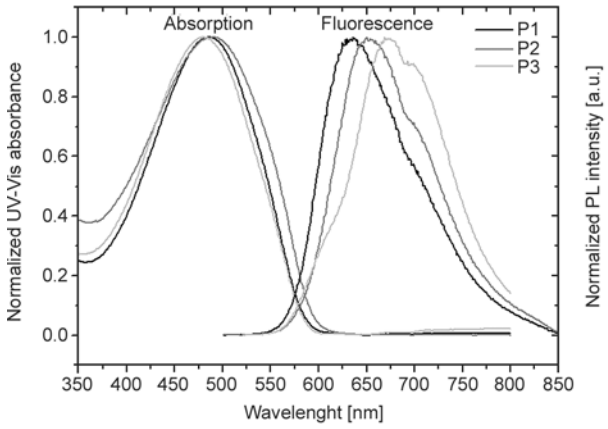

Figure 7. UV-vis absorption and PL spectra of polymers in thin films (60 nm)

tions exhibit a yellow fluorescence with a main emission band at 540 nm and a shoulder around 580 nm. Such vibrational structure is characteristic of the PPV system and is attributed to a coupling of the phenylene ring stretching modes with the π–π* electronic transitions [35]. The fluorescence quantum efficiencies of the isosorbide-based polymers were determined in dilute chloroform by a relative method using quinine sulfate as standard [26]. The obtained values are 51, 75 and 73% for **P1**, **P2** and **P3**, respectively. The polymer **P2** exhibits a significantly enhanced PL intensity in comparison with its isosorbide-free analogue **MH-PPV** (Figure 1), which shows a PL efficiency of 36%. This behavior can be attributed to the presence of the isosorbide moieties, which increase the rigidity of the macromolecular architecture. Besides, these polar groups may generate Keesom-type intramolecular interactions, which block the conformational changes. Hence, the available vibrational and rotational degrees of freedom were reduced and the loss of PL by such processes was considerably limited [36, 37].

The absorption and PL spectra of a solid film of **P1-3** are displayed in Figure 7. The polymer films present qualitatively the same absorption form as the corresponding solutions. Nevertheless, the spectra are broader and the absorption onsets significantly red-shifted. In fact, similar behavior is generally observed in π-conjugated polymers, and is attributed to the π-π interaction of the conjugated systems, hence, aggregate formation in the solid state [38]. The optical band gaps ($E_{g\text{-}op}$) estimated from the absorption onsets of the polymer films are 2.12, 2.09 and 2.12 eV for **P1**, **P2** and **P3**, respectively.

The PL spectra of the polymer films show an orange emission with similar features (Figure 7). In comparison with solution state, broader and red-shifted spectra were obtained (Table 3), as result of excimer formation [39]. However, the red-shift value increases from **P1** to **P3**, suggesting a higher inter-chain interaction in the **P3** film. This red-shift order is opposite to that obtained in our previously study of the isosorbide-free analogues of **P1-3** [20]. The difference can be explained by a more regular supramolecular organization in **P1-3**, as described in Figure 8 for the **P2** comparing with **MH-PPV**. According to these suggested arrangements of the PPV systems, the interactions between the conjugated sequences were limited by the aliphatic side-

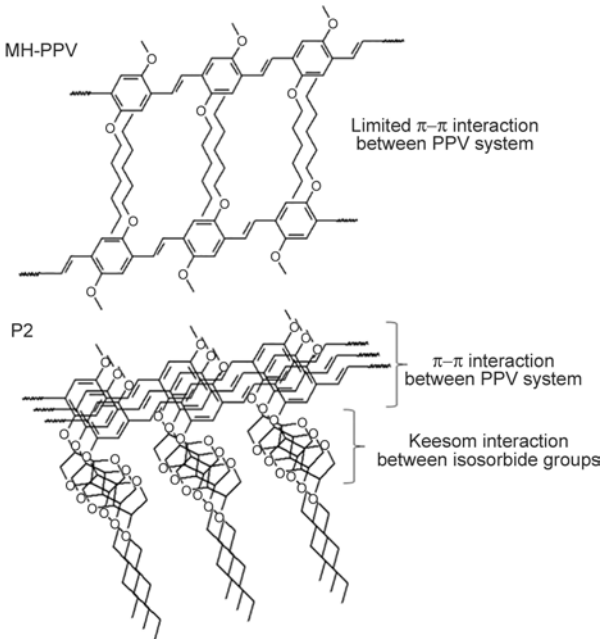

Figure 8. Suggested supramolecular organization of the PPV systems in **P2** and **MH-PPV**

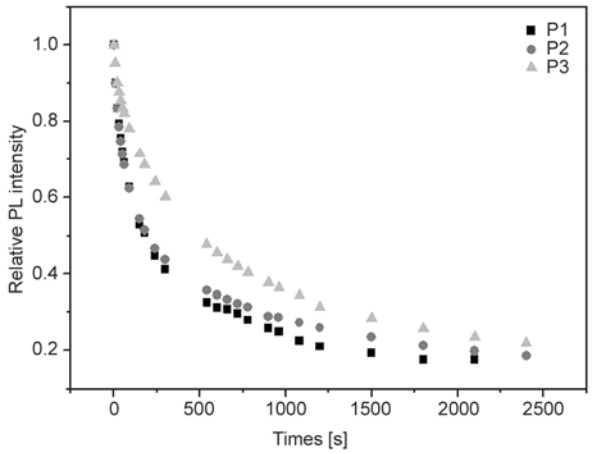

Figure 9. PL decay **P1-3** films upon irradiation at 480 nm

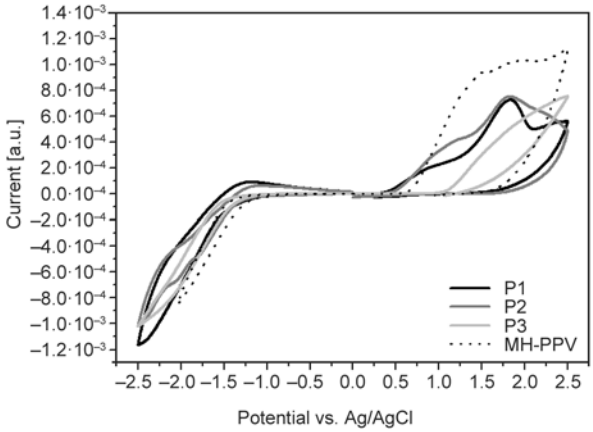

Figure 10. Cyclic voltammograms for polymer films coated onto ITO electrode (in 0.1 M (n-Bu)$_4$NBF$_4$/acetonitrile; scan rate: 50 mV·s^{-1})

chain in **MH-PPV**. Conversely, in **P2** film, the presence of the polar isosorbide groups improves the inter-chain stacking by the Keesom interaction and changes consequently the probable arrangement of the PPV backbone. In thin solid film, under the identical conditions, the **P2** shows the higher PL quantum yield as supported by the ratios of the polymer PL yields cited in Table 3. The Photobleaching of polymer films was examined under excitation at 480 nm. For all polymers, the emission spectra show no change in shape during irradiation for 40 nm. However, the fluorescence intensity decreases with time as presented in Figure 9. The results show that dodecyloxy containing polymer (**P3**) has the higher photo-oxidative stability.

3.4. Electrochemical and electrical characterization

Cyclic voltammetry (CV) was employed to investigate the redox behavior of the materials and to estimate their HOMO (Highest Occupied Molecular Orbital) and LUMO (Lowest Unoccupied Molecular Orbital) energy levels. Knowledge of these energy levels is of crucial importance to the selection of cathode and anode materials for OLED devices [40]. The use of CV analysis is reliable, as the electrochemical processes are similar to those involved in charge injection and transport processes in OLEDs [41]. The organic films were drop-coated onto an ITO glass substrate and scanned both positively and negatively in (*n*-Bu)$_4$NBF$_4$/acetonitrile. The cyclic voltammograms obtained are shown in Figure 10.

According to an empirical method [42] and by assuming that the energy level of the ferrocene/ferrocenium couple is 4.8 V below the vacuum level, the HOMO energy level (E_{HOMO}), LUMO energy level (E_{LUMO}) and the electrochemical gap ($E_{g\text{-}el}$) can be calculated as shown by Equations (3)–(5):

$$E_{HOMO}(\text{IP, ionization potential}) = -(V_{onset\text{-}ox} - V_{FOC} + 4.8)\ \text{eV} \quad (3)$$

$$E_{LUMO}(\text{EA, electron affinity}) = -(V_{onset\text{-}red} - V_{FOC} + 4.8)\ \text{eV} \quad (4)$$

$$E_{g\text{-}el} = (E_{LUMO} - E_{HOMO})\ \text{eV} \quad (5)$$

where V_{FOC} is the ferrocene half-wave potential (0.92 V), $V_{onset\text{-}ox}$ the polymer oxidation onset and $V_{onset\text{-}red}$ the polymer reduction onset, all measured versus Ag/AgCl. Accompanying the doping process, there was an obvious color change in the polymer film, i.e. orange in the neutral state and dark brown in the doped state, but no obvious reversible doping and dedoping process was observed. The HOMO and LUMO energy levels were estimated to be 4.27–4.97 and 2.46–2.54 eV, respectively. The electrochemical data-based energy diagram of polymers is presented in Figure 11. Analysis of the energy levels of the three polymers shows comparable electron affinities. However, the ionization potential increases with the side-chain length. The poly (2-hexyloxy-5-methoxy-*p*-phenylene vinylene) (**MH-PPV**) was used to compare the energy levels of HOMO and LUMO with that of its analogue with isosorbide group in side chain. It indicates that the HOMO level of **P2** is 0.2 eV higher in energy than that **MH-PPV**. Further, both polymers exhibit almost identical electronic affinities; hence, it showed a

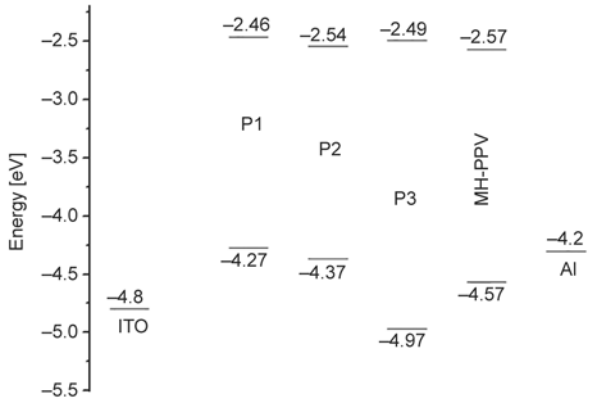

Figure 11. Energy diagram of ITO, **P1-3**, **MH-PPV** and Al

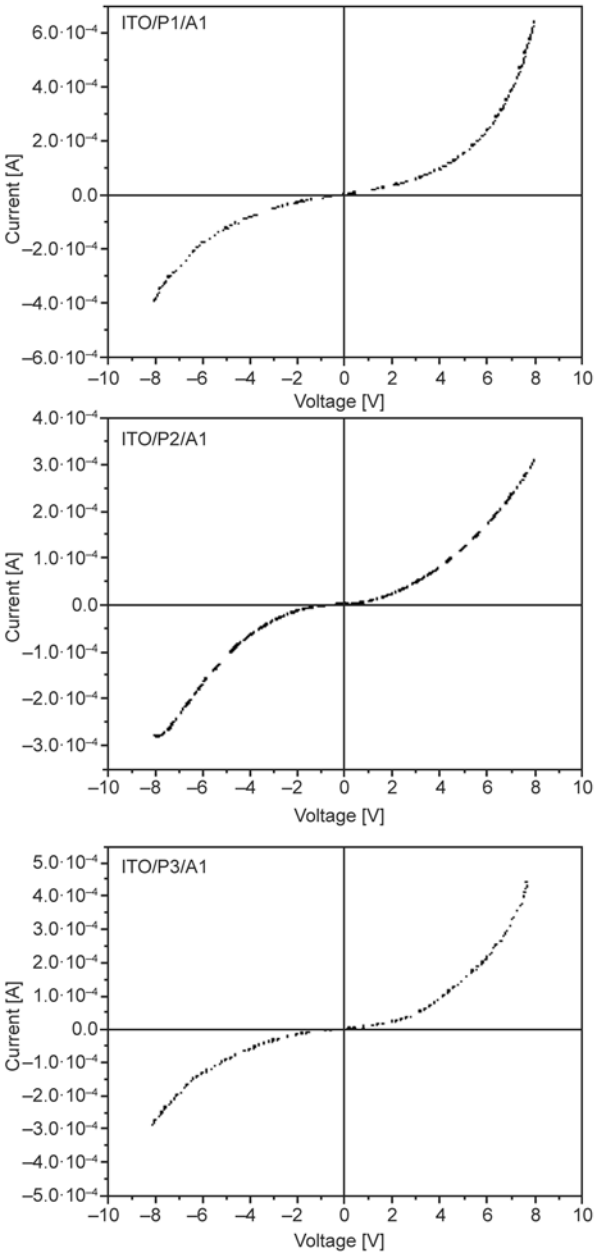

Figure 12. Current–voltage curve for [ITO/polymer/Al] devices

lower electrochemical gap. Three single-layer devices with the [ITO/polymer/Al] configuration were fabricated to investigate the current-voltage (I–V) characteristics of the isosorbide-PPV derivatives. As shown in Figure 12, the I–V curves indicate typical diode behavior with relatively low turn-on voltages of 3.41, 3.11 and 3.46 V for **P1**, **P2** and **P3**, respectively.

4. Conclusions

We have synthesized and investigated a series of semi-conducting isosorbide-PPVs: various side-chains were attached to the PPV system (ethyloxy: **P1**, hexyloxy: **P2** and dodecyloxy: **P3**). The polymers are prepared by Gilch polycondensation of chiral monomers. The synthesized polymers are optically active; they have good solubility and thermal stability going up to 320°C. The best homogeneity and the highest polarity were obtained for the **P3** film. The optical band gaps of the polymer thin films are around 2.1 eV. The polymer solutions exhibit a yellow fluorescence (540 nm) with relatively narrow emission spectra. The fluorescence quantum efficiencies of the isosorbide-containing polymers were determined in dilute solution and were 51, 75 and 73% for **P1**, **P2** and **P3**, respectively. The I–V characteristics of the devices with an ITO/polymer/Al configuration demonstrate typical diode behavior with relatively low turn-on voltages.

Acknowledgements

This work was supported by DGRS of the Ministry of High Education and Research fund of Tunisia. The authors thank Ms Amna Debbebi (Faculty of Sciences, Monastir) for the NMR measurements and Mr Haikel Hrichi (Laboratoire des Interfaces et Matériaux Avancés (LIMA), Faculty of Sciences, Monastir) for the electrical measurements. Special thanks go to John Lomas for his help in improving the quality of the English of this article and for his scientific remarks.

References

[1] Burroughes J. H., Bradley D. D. C., Brown A. R., Marks R. N., Mackay K., Friend R. H., Burns P. L., Holmes A. B.: Light-emitting diodes based on conjugated polymers. Nature, **347**, 539–541 (1990). DOI: 10.1038/347539a0

[2] Chen S-H., Li Y-R., Yu C-F., Lin C-F., Kao P-C.: Enhanced luminescence efficiency of Ag nanoparticles dispersed on indium tin oxide for polymer light-emitting diodes. Optics Express, **21**, 26236–26243 (2013). DOI: 10.1364/OE.21.026236

[3] Kim C-G., Koo M-S., Choi S-H., Lee D-H., Park D-K.: Enhanced performance in polymer light-emitting diodes (PLEDs) by using water soluble conjugation polymer. Bulletin of the Korean Chemical Society, **33**, 3087–3090 (2012). DOI: 10.5012/bkcs.2012.33.9.3087

[4] Zheng H., Zheng Y., Liu N., Ai N., Wang Q., Wu S., Zhou J., Hu D., Yu S., Han S., Xu W., Luo C., Meng Y., Jiang Z., Chen Y., Li D., Huang F., Wang J., Peng J., Cao Y.: All-solution processed polymer light-emitting diode displays. Nature Communications, **4**, 1–7 (2013). DOI: 10.1038/ncomms2971

[5] Deng X-Y.: Light-emitting devices with conjugated polymers. International Journal of Molecular Sciences, **12**, 1575–1594 (2011). DOI: 10.3390/ijms12031575

[6] Teichler A., Shu Z., Wild A., Bader C., Nowotny J., Kirchner G., Harkema S., Perelaer J., Schubert U. S.: Inkjet printing of chemically tailored light-emitting polymers. European Polymer Journal, **49**, 2186–2195 (2013). DOI: 10.1016/j.eurpolymj.2013.03.031

[7] Cataldo S., Pignataro B.: Polymeric thin films for organic electronics: Properties and adaptive structures. Materials, **6**, 1159–1190 (2013). DOI: 10.3390/ma6031159

[8] Lee J., Kim D. H., Kim J-Y., Yoo B., Chung J.W., Park J-I., Lee B-L., Jung J. Y., Park J. S., Koo B., Im S., Kim J. W., Song B., Jung M-H., Jang J. E., Jin Y. W., Lee S-Y.: Reliable and uniform thin-film transistor arrays based on inkjet-printed polymer semiconductors for full color reflective displays. Advanced Materials, **25**, 5886–5892 (2013). DOI: 10.1002/adma.201301257

[9] Kim Y., Lim E.: Development of polymer acceptors for organic photovoltaic cells. Polymers, **6**, 382–407 (2014). DOI: 10.3390/polym6020382

[10] Berger R., Domanski A. L., Weber S. A. L.: Electrical characterization of organic solar cell materials based on scanning force microscopy. European Polymer Journal, **49**, 1907–1915 (2013). DOI: 10.1016/j.eurpolymj.2013.03.005

[11] Palaparthy V. S., Baghini M. B., Singh D. N.: Review of polymer-based sensors for agriculture-related applications. Emerging Materials Research, **2**, 166–180 (2013). DOI: 10.1680/emr.13.00010

[12] Bisri S. Z., Takenobu T., Iwasa Y.: The pursuit of electrically-driven organic semiconductor lasers. Journal of Materials Chemistry C, **2**, 2827–2836 (2014). DOI: 10.1039/C3TC32206H

[13] Chen S. J., Zhang Q. Y., Gu J. W., Ma M. L., Zhang L., Zhou J., Zhou Y. Y.: A new conjugated polymer with donor-acceptor architectures based on alternating 1,4-divinyl-2,5-dioctyloxybenzene and 5,8-(2,3-dipyridyl)-quinoxaline: Synthesis, characterization, and photoinduced charge transfer. Express Polymer Letters, **6**, 454–464 (2012). DOI: 10.3144/expresspolymlett.2012.48

[14] Botiz I., Schaller R. D., Verduzco R., Darling S. B: Optoelectronic properties and charge transfer in donor-acceptor all-conjugated diblock copolymers. The Journal of Physical Chemistry C, **115**, 9260–9266 (2011). DOI: 10.1021/jp201344p

[15] Segura J. L.: The chemistry of electroluminescent organic materials. Acta Polymerica, **49**, 319–344 (1998). DOI: 10.1002/(SICI)1521-4044(199807)49:7<319::AID-APOL319>3.0.CO;2-Q

[16] Chochos C. L., Choulis S. A.: How the structural deviations on the backbone of conjugated polymers influence their optoelectronic properties and photovoltaic performance. Progress in Polymer Science, **36**, 1326–1414 (2011). DOI: 10.1016/j.progpolymsci.2011.04.003

[17] Junkers T., Vandenbergh J., Adriaensens P., Lutsen L., Vanderzande D.: Synthesis of poly(*p*-phenylene vinylene) materials *via* the precursor routes. Polymer Chemistry, **3**, 275–285 (2012). DOI: 10.1039/C1PY00345C

[18] Cacialli F.: Conjugated and electroluminescent polymers. Current Opinion in Colloid and Interface Science, **4**, 159–164 (1999). DOI: 10.1016/S1359-0294(99)00020-5

[19] Jaballah N., Chemli M., Hriz K., Fave J-L., Jouini M., Majdoub M.: Blue-luminescent poly(*p*-phenylene-vinylene) derivatives: Synthesis and effect of side-group size on the optical properties. European Polymer Journal, **47**, 78–87 (2011). DOI: 10.1016/j.eurpolymj.2010.10.017

[20] Trad H., Majdoub M., Davenas J.: Soluble PPVs with few structural defects: Synthesis and characterization. Materials Science and Engineering: C, **26**, 334–339 (2006). DOI: 10.1016/j.msec.2005.10.041

[21] Pu L.: The study of chiral conjugated polymers. Acta Polymerica, **48**, 116–141 (1997). DOI: 10.1002/actp.1997.010480402

[22] Kotkar D., Joshi V., Ghosh P.: Towards chiral metals. Synthesis of chiral conducting polymers from optically active thiophene and pyrrole derivatives. Journal of the Chemical Society, Chemical Communications, **14**, 917–918 (1988). DOI: 10.1039/C39880000917

[23] Lemaire M., Delabouglise D., Garreau R., Guy A., Roncali J.: Enantioselective chiral poly(thiophenes). Journal of the Chemical Society, Chemical Communications, **10**, 658–661 (1988). DOI: 10.1039/C39880000658

[24] Moore J. S., Gorman C. B., Grubbs R. H.: Soluble, chiral polyacetylenes: Syntheses and investigation of their solution conformation. Journal of the American Chemical Society, **113**, 1704–1712 (1991). DOI: 10.1021/ja00005a039

[25] Feng L., Chen Z.: Synthesis and photoluminescent properties of polymer containing perylene and fluorene units. Polymer, **46**, 3952–3956 (2005). DOI: 10.1016/j.polymer.2005.02.102

[26] Melhuish W. H.: Quantum efficiencies of fluorescence of organic substances: Effect of solvent and concentration of the fluorescent solute. The Journal of Physical Chemistry, **65**, 229–235 (1961). DOI: 10.1021/j100820a009

[27] Lauter U., Meyer W. H., Wegner G.: Molecular composites from rigid-rod poly(*p*-phenylene)s with oligo (oxyethylene) side chains as novel polymer electrolytes. Macromolecules, **30**, 2092–2101 (1997). DOI: 10.1021/ma961098y

[28] Cope A. C., Shen T. Y.: The stereochemistry of 1,4: 3,6-dianhydrohexitol derivatives. Journal of the American Chemical Society, **78**, 3177–3182 (1956). DOI: 10.1021/ja01594a055

[29] Lemieux R. U., McInnes A. G.: The preferential tosylation of the *endo*-5-hydroxyl group of 1,4;3,6-dianhydRO-D-glucitol. Canadian Journal of Chemistry, **38**, 136–140 (1960). DOI: 10.1139/v60-015

[30] Hriz K., Jaballah N., Chemli M., Fave J. L., Majdoub M.: Synthesis and characterization of new anthracene-based semiconducting polyethers. Journal of Applied Polymer Science, **119**, 1443–1449 (2011). DOI: 10.1002/app.32659

[31] Hriz K., Chemli M., Jaballah N., Fave J-L., Majdoub M.: Synthesis, characterization and optical properties of distyrylanthracene-based polymers. High Performance Polymers, **23**, 290–299 (2011). DOI: 10.1177/0954008311405866

[32] Gohil R. M.: Properties and strain hardening character of polyethylene terephthalate containing isosorbide. Polymer Engineering and Science, **49**, 544–553 (2009). DOI: 10.1002/pen.20840

[33] Rouis A., Echabaane M., Sakly N., Dumazet-Bonnamour I., Ben Ouadaa H.: Electrochemical analysis of a PPV derivative thin film doped with β-ketoimine calix[4]arene in the dark and under illumination for the detection of Hg^{2+} ions. Synthetic Metals, **164**, 78–87 (2013). DOI: 10.1016/j.synthmet.2013.01.005

[34] van Oss C. J., Chaudhury M. K., Good R. J.: Monopolar surfaces. Advances in Colloid and Interface Science, **28**, 35–64 (1987). DOI: 10.1016/0001-8686(87)80008-8

[35] Ton-That C., Stockton G., Phillips M. R., Nguyen T-P., Huang C. H., Cojocaru A.: Luminescence properties of poly-(phenylene vinylene) derivatives. Polymer International, **57**, 496–501 (2008). DOI: 10.1002/pi.2373

[36] Noordover B. A. J., van Staalduinen V. G., Duchateau R., Koning C. E., van Benthem R. A. T. M., Mak M., Heise A., Frissen A. E., Haveren J. V.: Co- and terpolyesters based on isosorbide and succinic acid for coating applications: Synthesis and characterization. Biomacromolecules, **7**, 3406–3416 (2006). DOI: 10.1021/bm060713v

[37] Henari F. Z., Manaa H., Kretsch K. P., Blau W. J., Rost H., Pfeiffer S., Teuschel A., Tillmann H., Hörhold H. H.: Effective stimulated emission and excited state absorption measurements in the phenylene–vinylene oligomer (1,4-bis-(alpha-cyanostyryl)-2,5-dimethoxybenzene)). Chemical Physics Letters, **307**, 163–166 (1999). DOI: 10.1016/S0009-2614(99)00536-9

[38] Peng K-Y., Chen S-A., Fann W-S., Chen S-H., Su A-C.: Well-packed chains and aggregates in the emission mechanism of conjugated polymers. The Journal of Physical Chemistry B, **109**, 9368–9373 (2005). DOI: 10.1021/jp044243f

[39] Huang Y. F., Shiu Y. J., Hsu J. H., Lin S. H., Su A. C., Peng K. Y., Chen S. A., Fann W. S.: Aggregate versus excimer emissions from poly(2,5-di-*n*-octyloxy-1,4-phenylenevinylene). The Journal of Physical Chemistry C, **111**, 5533–5540 (2007). DOI: 10.1021/jp067751t

[40] Fan B., Sun Q., Song N., Wang H., Fan H., Li Y.: Electroluminescent properties of a partially-conjugated hyperbranched poly(*p*-phenylene vinylene). Polymers for Advanced Technologies, **17**, 145–149 (2006). DOI: 10.1002/pat.705

[41] Cheng M., Xiao Y., Yu W-L., Chen Z-K., Lai Y-H., Huang W.: Synthesis and characterization of a cyano-substituted electroluminescent polymer with well-defined conjugation length. Thin Solid Films, **363**, 110–113 (2000). DOI: 10.1016/S0040-6090(99)01036-6

[42] Bredas J. L., Silbey R., Bordeaux D. S., Chance R. R.: Chain-length dependence of electronic and electrochemical properties of conjugated systems: Polyacetylene, polyphenylene, polythiophene, and polypyrrole. Journal of The American Chemical Society, **105**, 6555–6559 (1983). DOI: 10.1021/ja00360a004

eXPRESS Polymer Letters Vol.8, No.10 (2014) 723–732
Available online at www.expresspolymlett.com
DOI: 10.3144/expresspolymlett.2014.75

Epoxy resin/phosphonium ionic liquid/carbon nanofiller systems: Chemorheology and properties

H. Mąka, T. Spychaj[*]*, R. Pilawka*

West Pomeranian University of Technology in Szczecin, Polymer Institute, ul. Pulaskiego 10, 70-322 Szczecin, Poland

Received 21 March 2014; accepted in revised form 18 May 2014

Abstract. Epoxy nanocomposites with commercial carbon nanotubes (CNT) or graphene (GN) have been prepared using phosphonium ionic liquid [trihexyltetradecylphosphonium bis(2,4,4-trimethylpentyl) phosphinate, IL-f]. IL-f served simultaneously as nanofiller dispersing medium and epoxy resin catalytic curing agent. An influence of IL-f/epoxy weight ratio (3, 6 and 9/100, phr), carbon nanofiller type and content on viscosity of epoxy compositions during storage at ambient temperature was evaluated. Curing process was controlled for neat and CNT or GN modified epoxy compositions (0.25–1.0 wt% load) using differential scanning calorimetry and rheometry. Epoxy nanocomposites exhibited slightly increased glass transition temperature values (146 to 149°C) whereas tan δ and storage modulus decreased (0.30 to 0.27 and 2087 to 1070 MPa, respectively) as compared to reference material. Crosslink density regularly decreased for composites with increasing CNT content (11 094 to 7020 mol/m^3). Electrical volume resistivity of the nanocomposites was improved in case of CNT to $4 \cdot 10^1$ Ω·m and GN to $2 \cdot 10^5$ Ω·m (nanofiller content 1 wt%). Flame retardancy was found for modified epoxy materials with as low GN and phosphorus content as 0.25 and 0.7 wt%, respectively (increase of limiting oxygen index to 26.5%).

Keywords: *nanocomposites, epoxy resin, ionic liquid, carbon nanofillers*

1. Introduction

Ionic liquids (ILs) have been applied as sole crosslinkers for epoxy resin [1–5] or admixtures for epoxy systems cured with conventional hardeners that allowed to modify the properties of the final epoxy materials [3, 6–8]. ILs have been used together with polyamine or anhydride hardeners in order to modify epoxy curing process as well as materials glass transition temperature [7, 8], lubrication [6], or to improve (nano)filler dispersion [9–11].

The epoxy compositions with the most often used 1-alkyl-3-methylimidazolium ILs exhibited pot life at ambient temperature: 50–60 days where counteranions were chloride or tetrafluoroborate (3 wt parts/100 wt parts of epoxy resin, 3 phr) [4, 12]. That parameter was shortened to 30 days when 1-butyl-3-methylimidazolium (BMIM) with dicyanamide anion [2] or even to 3 days when BMIM with thiocyanate anion [5] was used (at 3 phr). Phosphonium ILs have also been tested as epoxy crosslinking agents by Soares *et al*. [6] and Silva *et al*. [13]. It has been found that aliphatic phosphonium IL [trihexyltetradecylphosphonium bis(2,4,4-trimethylpentyl) phosphinate, IL-f] allowed to obtain epoxy materials with good thermomechanical properties and high thermal stability [13]. Glass transition temperatures of the epoxy materials crosslinked solely with ILs were often above 150°C [2, 4, 5, 13].

The important advantages of applying ILs for liquid epoxy resin catalytic curing are their low loadings (typically 3–9 phr) as well as fast and easy miscibility with other liquid components resulting in technological feasibility [5]. However, there is another advantage of ILs, i.e. ability to disperse carbon

[*]Corresponding author, e-mail: Tadeusz.Spychaj@zut.edu.pl

nanofillers before or during their introduction into epoxy systems [9, 11, 14].

Nanocomposite materials with epoxy resin matrix including those modified with carbon nanofillers are widely applied as adhesives, encapsulants, and coatings in various areas of industry. An incorporation of carbon nanostructures, especially carbon nanotubes (CNT) and graphene (GN) into epoxy material is a great challenge. Successful enhancement of mechanical and electrical properties could be reached only when the nanofiller was well dispersed within polymer matrix. It makes possible to minimize carbon nanofiller content necessary to obtain electrical percolation. Generally, CNTs and GN have tendencies to form heavily entangled or agglomerated structures, respectively. It was found that using room temperature ILs was one of the effective approaches of dispersing carbon nanofillers [15–17].

Guo *et al*. [9] and Hameed *et al*. [11] applied imidazolium ILs as dispersing media for expanded graphite (EG) and multiwalled CNT (MWCNT) introduced subsequently into epoxy resins [curing agents were polyoxypropylene diamine (Jeffamine D230) or 4,4′-methylenedianiline, respectively]. EG was ground with IL (BMIM hexafluorophosphate) and mixed with epoxy resin under stirring [9]. MWCNT suspension in epoxy resin containing [BMIM] tetrafluoroborate was prepared by sonication and mechanical stirring [11].

In one of the recent works [5] GN (0.25–1.0 wt%) has been mixed with deep eutectic ionic solvent (based on choline chloride and trihydroxymethylpropane), then sonicated and afterwards simply mixed with epoxy resin containing BMIM thiocyanate. The term 'deep eutectic solvents' (DESs) describes mixtures of some cationic compound, typically ammonium halogenate (e.g. choline chloride) and polar compound bearing –OH, –COOH or $–CONH_2$ moieties able to form hydrogen bonds with anion of the former. DESs exhibit substantially lower melting point (usually below 100°C) than any of the components [18]. DESs share many ILs characteristics, however are inexpensive, easy to prepare, nontoxic and often biodegradable. These features allow them to play multiple roles in polymers and related materials [19].

Throckmorton *et al*. [14] used GN or single walled CNT (SWCNT) to obtain paste in IL (1-ethyl-3-methylimidazolium dicyanamide, EMIM). They used 3-roll mill with regulated rollers rotation, the number of repeated mixing cycles and constant gap between rollers (20 μm). Cured EMIM/epoxy resin materials (with high IL content 17.6 phr) exhibited very low electrical network percolations; $1.7 \cdot 10^{-2}$ and $8.6 \cdot 10^{-5}$ vol% for GN and SWCNT, respectively.

In literature more tedious methodology of epoxy resin/CNT/ionic liquid nanocomposite manufacturing was also reported [20, 21]. Wang and Guo group applied imidazolium IL chemically functionalized CNT for epoxy nanocomposites preparation. Multistep procedure was used: (i) sulfoxylation of –COOH groups present at CNT surface defects with $SOCl_2$, (ii) reaction of formed acid chloride moieties with $–NH_2$ groups of 3-aminopropylimidazole, (iii) introduction of epoxy groups on imidazole ring with simultaneous quaternization of nitrogen atom (thus creating imidazolium ionic liquid structure) as a result of reaction with epichlorohydrin, (iv) preparation of CNT-IL/curing agent solvent dispersion (aromatic diamine, EpiCure W, was used as a hardener) by sonication (4 h/room temperature + 3 h/60°C), (v) addition of epoxy resin into the CNT-IL/curing agent solvent dispersion; shear mixing (0.5 h/80°C) and additional sonication (0.5 h/80°C), (vi) degassing and curing (4 h/120°C). The final nanocomposite materials exhibited electrical conductivity $8.4 \cdot 10^{-3}$ S/cm (1 wt% CNT-IL loading) and tensile strength increased ca. 36% (0.5 wt% CNT-IL) [21].

Considering the studies mentioned above continuation of research on application of other ILs in conjunction with carbon nanofillers to develop high performance epoxy resin nanocomposites is reasonable. In this work, the epoxy resin/IL systems with the mentioned phosphonium IL-f and CNT or GN content were investigated with the aim of obtaining nanocomposite epoxy materials with improved thermomechanical, electrical as well as flame retardancy features.

2. Experimental

2.1. Materials

Epoxy resin: bisphenol A-based low molecular weight Epidian 6 (E6); epoxy equivalent 185 g, (viscosity 18 000 mPa·s at 23°C), Organika Sarzyna, Poland was used. Trihexyltetradecylphosphonium bis(2,4,4-trimethylpentyl)phosphinate (>95%, Sigma-Aldrich) was used as curing agent for epoxy

resin and as a medium for carbon nanofiller dispersing. Two different types of carbon nanoparticles were applied: (i) graphene obtained by vapor deposition technology with specific surface >750 m^2/g, layer thickness <2 nm, particle diameter <0.1 μm, carbon layer number <3 (Graphene Technologies, USA), and (ii) multiwall nanotubes, Nanocyl NC7000, with specific surface 250–300 m^2/g, average length 1.5 μm, average diameter 9.5 nm, carbon content 90 wt% (Nanocyl, Belgium).

2.2. Preparation of carbon dispersions and epoxy compositions

The neat epoxy compositions were obtained by mixing of epoxy resin with IL-f at ambient temperature. The IL-f content was 3, 6 and 9 wt parts/100 wt parts epoxy resin.

The carbon nanofillers were introduced into the epoxy compositions in two different ways. GN in the amount of 0.25, 0.5 or 1.0 wt% (relation to epoxy resin) was added into IL-f and then homogenized by sonication (2 h, amplitude 50%, frequency 50 Hz, UP 200S, Hielscher GmbH, Germany). Subsequently, GN dispersion in IL-f was manually mixed with epoxy resin for 10 min. CNTs (0.25, 0.5 or 1.0 wt% in relation to epoxy resin) were dispersed in epoxy resin by ultrasonication for 2 h. Next, IL-f was added into the epoxy composition and the systems mixed manually for 10 min. Constant amount of IL-f (9 phr) was adjusted in all epoxy compositions with carbon nanofillers. Eventually, the epoxy compositions were cured in teflon mold at 120°C for 2 h. The resultant samples were used for further investigations. Differentiation of carbon nanofiller dispersion methodology was performed because of specific features of GN and CNT nanofillers. Carbon nanotubes need a large amount of wetting agent, i.e. IL-f, to obtain a uniform dispersion with viscosity enabling handling. Applied amount of ionic liquid (9 phr) was too low to be efficiently used as CNT dispersing medium. For that reason CNTs were first dispersed in epoxy resin and afterwards IL-f was introduced into epoxy/CNT composition.

2.3. Methods

The viscosity of epoxy compositions with carbon nanoparticles was determined using stress rheometer (Rheometric Scientific, USA) at room temperature, a plate-plate system, ø = 40 mm, a gap of 1 mm. The storage time for epoxy resin/crosslinker compositions at ambient temperature was determined on a basis of viscosity measurements during storage at 23–25°C using rheometer.

The curing process of epoxy compositions was investigated using differential scanning calorimeter (DSC, Q-100, TA Instruments, USA), at a heating rate of 5°C/min in the temperature range of 30–220°C and rheometer (Rheometric Scientific) at the same measurement schedule.

The glass transition temperatures (T_g), tan δ values and storage moduli were determined using dynamic mechanical thermal analysis (DMTA, Q – 800, TA Instruments) with dual cantilever, at heating rate of 2°C/min from 30 to 250°C, frequency 1 Hz.

Thermogravimetric analysis (TGA, Q500, TA Instruments) was performed using platinum pan under 25 mL/min air flow, in temperature range 40–800°C at a heating rate of 10°C/min.

The volume electrical resistance of cured composites with different carbon nanofiller content was tested at room temperature in accordance with IEC 93:1980 and ASTM D 257-99 (Keithley 8009 with a set of electrodes, Keithley Instruments, Inc., USA).

The limiting oxygen index (LOI) of the nanocomposites was measured using oxygen concentration meter (GOX 100, Greisinger Electronic GmbH, Germany) at room temperature, in accordance with PN-EN ISO 4589-2. The test was based on the determination of oxygen content (%) in a gas mixture of O_2 and N_2. The thin strips (5×1×0.25 cm) of each material were clamped vertically and ignited at the top.

3. Results and discussion

3.1. Influence of storage time, nanofiller type and content on viscosity of epoxy compositions

Viscosity changes during storage of epoxy compositions with increasing IL-f content in a range 3–9 phr were controlled up to 8 days (Table 1). It was clear that introduction of IL-f into epoxy resin caused slight decrease of viscosity when measured directly after components mixing (day 0). However, after 2-days storage rather high differences were found, i.e.: (i) from 13.3 → 16.5 Pa·s for the composition with the lowest IL-f content, (ii) it was almost doubled for medium IL-f content (13.0 → 24.1 Pa·s, 6 phr), and (iii) up to 8-times increase (12.9 to ca. 105 Pa·s) for the system with the high-

Table 1. Viscosity change of epoxy compositions with various content of phosphonium phosphinate ionic liquid (IL-f) during storage at room temperature

Composition acronym	Viscosity (days after component mixing) [Pa·s]				
	0	2	4	7	8
E6/IL-f_3	13.3±0.10	16.5±0.4	18.3±0.2	520.4±1.5	gel
E6/IL-f_6	13.0±0.10	24.1±0.3	258.1±1.2	gel	–
E6/IL-f_9	12.9±0.01	104.8±0.8	gel	–	–

est IL content, (iv) extremely high viscosity jump was found for E6/IL-f_6 after 4-day storage (almost 20 times, i.e. to 258 Pa·s), whereas composition containing the highest amount of IL-f showed gelation (i.e. viscosity above 3000 Pa·s) after that time.

Silva *et al*. [13] have reported recently that the pot lives of epoxy compositions containing 2.5, 5 and 10 phr IL-f at room temperature were: 26, 8 and 4 days, respectively, i.e. slightly longer than reported in here (more significant difference was found for system with the lowest IL-f content). It does mean that IL-f belongs (together with [BMIM] thiocyanate [5]) to the most reactive ionic liquids applied up today for epoxy resin crosslinking.

From applied view point an effect of carbon nanofiller presence on relevant epoxy compositions viscosity (η) is essential. In Table 2 the viscosities of epoxy systems with the highest content of IL-f (9 phr) and CNTs or GNs (0.25–1 wt%) were collected. Slight increase of η could be observed for composition filled with GN, from 12.9 for neat system up to 16.9 Pa·s for composition with 1 phr load. As it was already mentioned, the compositions with GN were first dispersed in IL-f by sonication and then introduced into epoxy resin. More significant influence of CNT on epoxy systems viscosity was observed. Even low CNT content (0.25 wt%) resulted in almost 3.5-times increase of epoxy composition viscosity (12.9 → 47.7 Pa·s) whereas η increased 16-times (up to >200 Pa·s) for 1 wt% load. The procedure of composition preparation was in that case different: CNTs were introduced into epoxy resin, then the system was sonicated and mixed with the curing agent.

3.2. Curing process of epoxy compositions

Curing process of epoxy resin/IL-f systems with various crosslinking agent content (3–9 phr) was investigated by rheometric and DSC techniques in a range from 40 up to 220°C with temperature gradient increase 5°C/min.

The results were presented in Figure 1 and Table 3. Rheometric and heat flow curves were consistent. The relevant values for viscosity jumps followed the order 145°C > 130°C > 125°C for E6/IL-f with 3, 6 and 9 phr, respectively. The temperature of exothermal peak maximum determined by DSC were: 133°C > 123°C > 118°C, respectively. It was also found that onset exothermal temperatures for the investigated systems (evidenced start of gelation process) were influenced by IL-f amount rather in low extent (101–106°C). The effect of crosslinking exothermic reaction extended importantly when IL-f content in epoxy system increased from 3 to 6 phr

Table 3. Curing characteristics for the system E6/IL-f and for epoxy compositions with carbon nanofillers from DSC measurements

Composition acronym	Onset exotherm temperature [°C]	Maximum exotherm temperature [°C]	ΔH [J/g]
E6/IL-f_3	101	133	225
E6/IL-f_6	106	123	398
E6/IL-f_9	102	118	403
E6/(IL-f_9/GN_0.25)	100	125	388
E6/(IL-f_9/GN_0.50)	108	123	383
E6/(IL-f_9/GN_1.00)	101	122	417
(E6/CNT_0.25)/IL-f_9	100	126	388
(E6/CNT_0.50)/IL-f_9	101	126	382
(E6/CNT_1.00)/IL-f_9	99	126	394

Table 2. Viscosity of epoxy compositions with 9 phr of phosphonium phosphinate ionic liquid (IL-f) and various content of carbon nanofillers directly after preparation

Composition acronym [GN in IL]	Viscosity [Pa·s]*	Composition acronym [CNT in E6]	Viscosity [Pa·s]*
E6/(IL-f_9/GN_0.25)	15.1±0.10	(E6/CNT_0.25)/IL-f_9	47.7±0.3
E6/(IL-f_9/GN_0.50)	15.8±0.10	(E6/CNT_0.50)/IL-f_9	89.2±0.5
E6/(IL-f_9/GN_1.00)	16.9±0.05	(E6/CNT_1.00)/IL-f_9	206.5±0.8

*measured on rheometer, room temperature

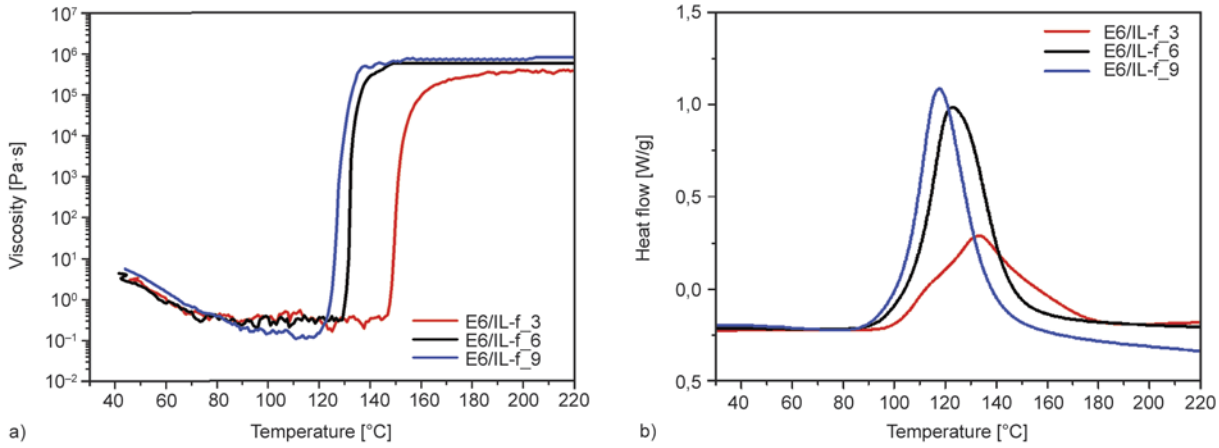

Figure 1. Change of viscosity – (a) and heat flow – (b) during curing process of epoxy resin with IL-f measured by rheometry and DSC, respectively

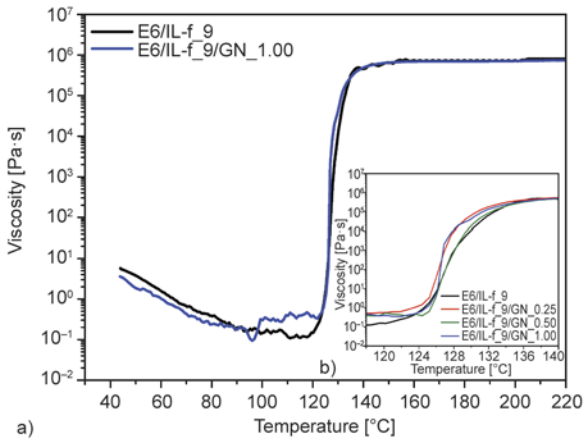

Figure 2. Rheometric curves of epoxy compositions with dispersion of IL-f_9 and various contents of GN (0.25–1.00 wt%) during curing process: at wide temperature range (40–220°C) – (a) and narrow temperature range (120–140°C) – (b)

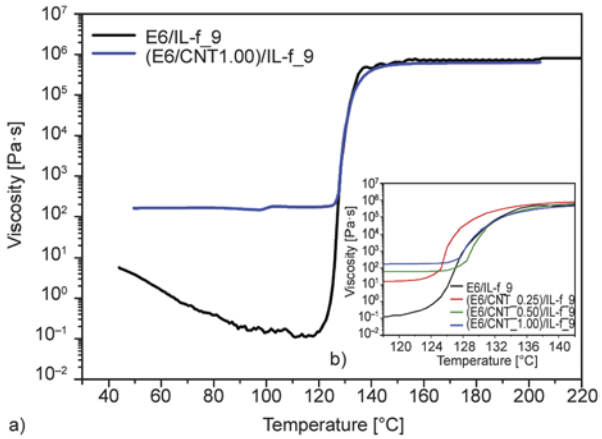

Figure 3. Rheometric curves of epoxy compositions with various contents of CNT dispersed in the resin (0.25–1.00 wt%) during curing process at wide temperature range (40–220°C) – (a) and narrow temperature range (120–140°C) – (b)

(225 → 398 J/g), whereas additional amount of the ionic liquid caused only minor ΔH increase (up to 403 J/g).

Curing of epoxy resin/IL-f/carbon nanofiller compositions was also followed by rheometric measurements (Figures 2 and 3). The following conclusion could be made on a basis of these results: (i) the viscosity of GN filled epoxy compositions decreased from 10 → 5 Pa·s during heating from 40 to 120°C. An influence of IL-f on viscosity is hardly visible. Fast gelation process was performed at 120–135°C. Slight shift of rheometric curves to lower temperature values for E6/IL-f/GN_0.25 and E6/IL-f/GN_1.00 was found in relation to the neat system E6/IL-f_9, (ii) rheometric curves for CNT modified epoxy compositions showed distinct differences in comparison to E6/IL-f_9 neat system. Significant viscosity increase at 100°C with increasing CNT content could be noted as followed: E6/IL-f_9: $2 \cdot 10^{-1} <$ (E6/CNT_0.25)/IL-f_9: $2 \cdot 10^{1} <$ (E6/CNT_0.50)/IL-f_9: $7 \cdot 10^{1} <$ (E6/CNT_1.00)/IL-f_9: $1.5 \cdot 10^{2}$ Pa·s. The gelation process performed in slightly wider temperature range (i.e. 120–140°C) when compared to the systems modified with GN. The lowest amount of CNT applied resulted in rheometric curve shift to lower temperatures (range from 124–132°C, in relation to the three other investigated compositions, Figure 3).

3.3. Properties of epoxy nanocomposites

For the E6/IL-f/carbon nanofillers cured system thermomechanical, thermal, electrical resistance and flammability tests were performed.

3.3.1. Thermomechanical and thermal properties

The crosslinking of the epoxy composition containing 3 phr IL-f was not efficient enough, as it could be seen from DMTA results in Table 4 (low values of glass transition temperature, T_g, and storage modulus, as well as high tan δ value). Higher contents of catalytic curing agent (6 and 9 phr) in epoxy compositions allowed to obtain epoxy materials with acceptable thermomechanical parameters, i.e. T_g (145–146°C), storage modulus (2097–2446 MPa) and tan δ (0.30–0.34). Crosslinking density parameter was estimated on a basis of Equation (1) [22, 23]:

$$\nu_e = \frac{E_r}{3RT_r} \quad (1)$$

where E_r is storage modulus at 'rubbery' state, i.e. at $T_r = T_g + 30$, R is universal gas constant. The values of ν_e for epoxy materials cured with 6 and 9 phr IL-f were rather high (12 758 and 11 094 mol/m^3, respectively) – significantly higher than for epoxy systems cured with BMIM thiocyanate (2113 and 7181 mol/m^3; using 9 and 3 phr of IL, respectively). That ν_e value difference was caused mainly by relatively high storage moduli values at 'rubbery' state (i.e. above 175°C) when IL-f was applied as crosslinking agent (Table 4).

The epoxy composition containing 9 phr IL-f was selected for preparing nanocomposite with carbon nanofillers. The presence of CNTs as well as GNs affected thermomechanical properties of epoxy nanocomposites in rather low extent. T_g slightly increased from 146 to 149°C; no regular tendency in dependence to filler type and content has been observed. The tan δ values decreased from 0.30 to 0.27 with CNTs or GNs content increase (Table 4). The storage modulus changed depending on carbon nanofiller kind: (i) clear and significant decrease (2087 → 1070 MPa) for neat epoxy materials and that filled with the highest (1.0 wt%) amount of CNTs, respectively, (ii) irregular changes when the other nanofiller was used: E6/IL-f_9/GN_0.50 (2172 MPa) and E6/IL-f_9/GN_1.00 (1995 MPa). Similarly, crosslink densities regularly decreased for materials containing CNTs:
neat epoxy (11 094 mol/m^3) > (E6/CNT_0.25)/IL-f_9 (9965 mol/m^3) > (E6/CNT_0.50)/IL-f_9 (7810 mol/m^3) > (E6/CNT_1.00)/IL-f_9 (7020 mol/m^3). Nanocomposites with GN exhibited maximum ν_e values in a range of nanofiller contents 0.25–0.50 wt% (12 841–12 852 mol/m^3) whereas for neat epoxy materials and that filled with the highest GN content crosslink densities were lower and rather similar (11 094 and 12 025 mol/m^3, respectively).

Putz *et al*. [24] considered three possible mechanisms for T_g variation referred to CNT nanoparticles presence in epoxy resin: (i) changed thermal conductivity could affect curing kinetics resulting in impeded attainment of consistent crosslink density (T_g ↓), (ii) network disruption leading to effective ν_e decrease (T_g ↓), (iii) interphase creation of thin films (T_g ↑ or ↓). Some data considering decreased [24, 25] or increased [24–26] T_g values for epoxy materials caused by CNT presence, have been reported. The possible explanation of observed T_g and tan δ variation related to introduction of carbon nanofillers could be enhancing interaction between carbon nanoparticles (perfectly wetted with IL) and epoxy network. Epoxy polymerization caus-

Table 4. Characteristic parameters for epoxy materials cured with IL-f and modified with carbon nanofillers from DMTA and TGA measurements

Composition acronym	DMTA					TGA		
	T_g [°C]	tan δ	Storage modulus* (glassy state) [MPa]	Storage modulus** ('rubber' state) [MPa]	Crosslink density [mol/m^3]	$T_{5\%}$ [°C]	$T_{10\%}$ [°C]	$T_{max.DTG}$ [°C]
E6/IL-f_3	44	1.27	800	0.0	n.d.	275	300	431
E6/IL-f_6	145	0.34	2446	139.7	12 758	360	394	438
E6/IL-f_9	146	0.30	2087	124.6	11 094	340	372	439
E6/(IL-f_9/GN_0.25)	148	0.29	2043	144.7	12 852	349	384	439
E6/(IL-f_9/GN_0.50)	149	0.27	2172	144.7	12 841	345	384	439
E6/(IL-f_9/GN_1.00)	146	0.28	1995	134.6	12 025	336	371	438
(E6/CNT_0.25)/IL-f_9	147	0.28	1930	108.8	9 965	354	393	438
(E6/CNT_0.50)/IL-f_9	147	0.27	1633	82.6	7 810	347	376	434
(E6/CNT_1.00)/IL-f_9	149	0.27	1070	79.1	7 020	358	398	435

n.d. – not determined, *determined at 40°C, **determined at T_g + 30

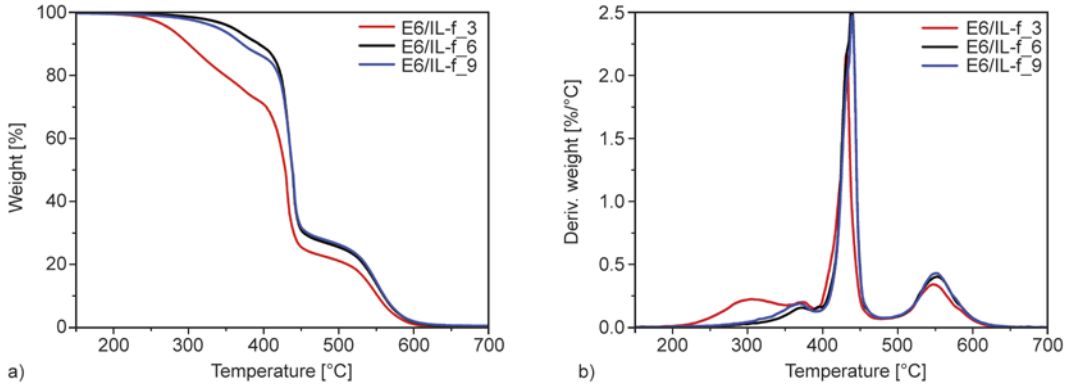

Figure 4. TGA (a) and DTG (b) curves for neat E6/IL-f epoxy materials

ing network formation began directly on carbon surface. In result thin interphase between epoxy network and carbon surface could be formed, resulting in T_g increase (tan δ decrease) because of some retarding dynamics in the system. Network disruption mechanism could be responsible for storage modulus as well as crosslink density decrease, especially for CNT modified nanocomposites.

Inefficiently crosslinked epoxy material based on E6/IL-f_3 exhibited clearly lower temperatures of 5 or 10% mass losses in comparison to those cured with higher IL-f content. Generally, the materials containing medium amount of curing agent (6 phr) exhibited the highest temperatures of 5 and 10% mass losses (360 and 394°C, respectively). Some influence of carbon nanofiller addition on the nanocomposites thermal stability has been observed as well (Figure 4, Table 4). The temperatures values of 5 and 10 wt% losses were about 8–12°C higher for the materials modified with 0.25 and 0.50 wt% of GN than for the reference one. Even higher increase of the mass loss temperatures for the epoxy nanocomposites modified with CNT (up to 18 and 26°C, for 5 and 10% mass losses, respectively) has been noted. The temperature values at maximum mass losses were placed in rather narrow range from 431 up to 439°C.

3.3.2. Electrical volume resistivity

Electrical volume resistivity of the investigated epoxy materials was evaluated. The changes of that parameter as a function of filler contents were presented in Figure 5. The electrical resistivity of neat epoxy material was found to be $1.9 \cdot 10^{11}$ Ω·m. The both carbon nanofillers improved the electrical conductivity of epoxy matrix several orders of magnitude, however, the results for nanocomposites with

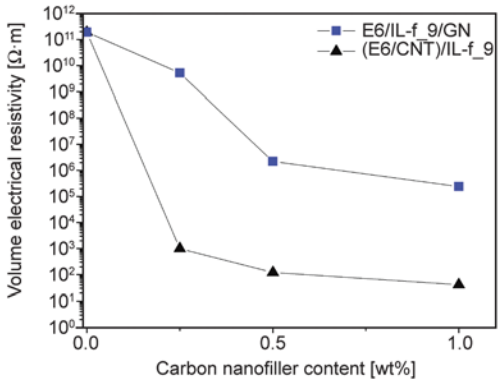

Figure 5. Volume resistivity of epoxy (nano)composites with GN and CNT as a function of nanofiller content

CNTs were substantially more pronounced. For the nanocomposites with GNs increasing filler content from 0.25 to 1 wt% caused reduction of electrical resistivity about 4 orders (from $5.2 \cdot 10^9$ to $2.4 \cdot 10^5$ Ω·m). An introduction of CNT into epoxy materials resulted in deep decrease of this parameter, i.e. altogether 8–10 orders of magnitude as compared to the reference neat epoxy material. In the range of CNT content 0.25–1.0 wt% electrical resistivity decreased to a lower extent from $1.1 \cdot 10^3$ to $4.1 \cdot 10^1$ Ω·m. It could be seen from Figure 5 that nanocomposites with CNT cured with phosphonium phosphinate ionic liquid exhibited percolation threshold below 0.25 wt% whereas these containing GN showed steadier decreasing electrical resistivity with growing nanoparticles content. These results were in qualitative agreement with recent literature data. Throckmorton *et al*. [14] have found that percolation threshold for epoxy nanomaterials modified with SWCNTs was ca. 2.5 order below that for GNP ($8.6 \cdot 10^{-5}$ and $1.7 \cdot 10^{-2}$ volume fraction, respectively). Both these values were close to the theoretical percolation thresholds predicted by power law

percolation theory model (for CNTs) or plate-like particle percolation theoretical models (for GNP) [14].

The obtained results showed that introduction of IL-f into preliminary sonicated epoxy resin/CNT system with afterwards simple mixing (without necessity of using more efficient dispersing technique) allowed to obtain epoxy nanocomposites with important improvement of electrical properties.

3.3.3. Limiting oxygen index

Phosphorus compounds represent important group of flame retardants including organic and inorganic phosphates [$(PO)_3PO$], phosphites [$(PO)_3P$], phosphonates [$(RO)_2PR'$], phosphinates [$(ROR'_2PO$], phosphines [R_3P], phosphine oxides [R_3PO], and phosphonium salts [R_4PX] [27]. As applied trihexyl(tetradecyl)phosphonium bis(2,2,4-trimethylpentyl)phosphinate contained phosphonium atom in cationic as well as in anionic part of IL, flame retardancy features of epoxy nanoycomposites cured with it were tested.

The limiting oxygen index test results were shown in Figure 6. Materials with LOI lower than 22% are flammable, with LOI between 22 and 25 are considered as self-extinguishing; when value of this parameter is above 26, the material reaches flame retardancy level [28]. All investigated epoxy materials exhibited LOI values above 22. Typical level of LOI for epoxy crosslinked with polyamines, e.g. triethylenetetramine is ca. 20 [29]. The LOI values of nanocomposites modified with CNTs were placed in a range from about 23 to 24.5, indicating that small amount (0.25–1.0 wt%) of CNTs in epoxy systems slightly improved flame retardancy. Epoxy nanocomposites modified with GN exhibited distinctly improved flame retardancy; for composites with 0.5 or 1.0 wt% GN LOI was above 27 (flame retardant). Even lower amount of GN applied (0.25 wt%) increased oxygen index parameter about 4 units from 22.5 up to 26.5%. Presented results indicated that GN was an effective flame retardant for epoxy nanocomposites cured with phosphonium phosphinate ionic liquid.

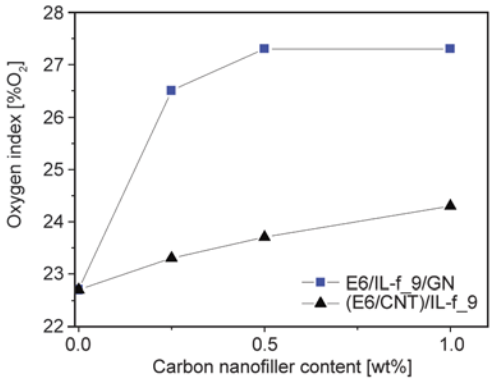

Figure 6. Oxygen index of epoxy (nano)composites with GN and CNT as a function of nanofiller content

Our results on flame retardant properties of epoxy nanocomposites cured with phosphorus containing IL and modified with GN could be compared with relevant data recently published by Chiang *et al*. [30]. That research group used graphene oxide (GO) and reduced GO (rGO) functionalized with DOPO (9,10-dihydro-9-oxa-10-phosphaphenanthrene-10-oxide) known flame retardant for epoxy materials. The grafting efficiency for DOPO/rGO ratio was 19.9 wt%. GO as well as rGO functionalized with DOPO (DOPO-rGO) were used in amounts 1, 5 and 10 wt% relative to epoxy resin (i.e. for DOPO-rGO containing 0.2, 1.0 and 2.0 wt% P as well as 0.8, 4.0 and 8.0 wt% rGO, respectively). Introduction of 1–10 wt% GO resulted in some LOI value increase (from 20 up to 23% as compared to neat epoxy cured with diaminodiphenylmethane). DOPO-rGO used with mentioned above ratios allowed to reach LOI values to: 21, 25 and 26%, respectively. Similar flame retardancy effect was reached in our work using: (i) rather simple GN dispersion methodology as comparing with DOPO grafting on rGO [30], (ii) substantially lower concentrations of modifying components, i.e. IL-f (serving simultaneously as curing catalysts, GN dispersion medium and antiflamming compound) and GN, i.e. 0.5 wt% GN and ca. 0.7 wt% P, as compared to those from ref. [30] (8.0 wt% GO and 2.0 wt% P) to obtain LOI value 26–27%.

4. Conclusions

Epoxy compositions with CNT or GN in presence of phosphonium ionic liquid have been prepared. IL played triple function: carbon nanofiller dispersing medium, catalytic curing agent and antiflamming additive. The pot life values of neat epoxy systems were 4 up to 8 days for IL-f/epoxy weight ratio between 9 and 3 phr at ambient temperature. The viscosities of epoxy compositions containing GN were negligibly higher. On the other hand the same contents of CNT (0.25–1.0 wt%) in epoxy systems caused dramatic viscosity jump from ca. 13 up to

207 Pa·s as measured directly after components mixing. With increasing IL-f content (3 → 9 phr) in epoxy resin the curing reaction started at lower temperatures as determined by rheometry (145 → 125°C) or DSC (133 → 118°C). Only slight influence of CNT or GN on curing characteristics of epoxy systems has been observed. Acceptable thermomechanical properties of IL-f cured epoxy neat materials were reported when at least 6 phr IL was applied (i.e. T_g 145–146°C, storage modulus 2097–2446 MPa, and tan δ 0.30–0.34). The both carbon nanofiller types slightly affected T_g and tan δ values (from 146 → 149°C and 0.30 → 0.27, respectively). However, storage modulus changed depending on nanoparticle type, i.e. significant decrease (2087 → 1070 MPa) for nanocomposites with CNT and irregular changes in narrow values range (2172 → 1995 MPa) with GN was observed. For crosslink density similar trend was observed, i.e. changes in rather wide range (11 094 → 7020 mol/m^3) for CNT modified materials and little difference for GN filled composite materials. Thermal resistance of epoxy material was improved when CNTs were added (18–26°C for 5 and 10% mass losses) and to a lower extent for GN modified materials (8–12°C). Electrical bulk resistivity decreased about 8 order of magnitude after inclusion of 0.25 wt% CNT to epoxy materials. The highest electrical conductivity, i.e. $4 \cdot 10^1$ Ω·m was registered for nanocomposite containing 1 wt% CNT. Higher resistivity exhibited epoxy materials modified with GN (up to $2.4 \cdot 10^6$ Ω·m). The presence of phosphonium phosphinate IL resulted in some improvement of LOI index for neat epoxy material (22.7 when compared to 20% for conventional epoxy materials cured with polyamine). However, few-layer GN caused high improvement of that parameter (up to 26.5 for 0.25 wt% load) in the nanocomposite. Such an epoxy nanocomposite material could be considered as electroconductive (below 10^5 Ω·m [31]) and flame retardant.

References

[1] Kowalczyk K., Spychaj T.: Ionic liquids as convenient latent hardeners of epoxy resin. Polimery, **48**, 833–835 (2003).

[2] Rahmathullah A. M., Jeyarajasingam A., Merritt B., VanLandingham M., McKnight S. H., Palmese G. R.: Room temperature ionic liquids as thermally latent initiators for polymerization of epoxy resins. Macromolecules, **42**, 3219–3221 (2009).
DOI: 10.1021/ma802669k

[3] Soares B. G., Livi S., Duchert-Rumeau J., Gerard J-F.: Synthesis and characterization of epoxy/MCDEA networks modified with imidazolium-based ionic liquids. Macromolecular Materials and Engineering **296**, 826–834 (2011).
DOI: 10.1002/mame.201000388

[4] Mąka H., Spychaj T., Pilawka R.: Epoxy resin/ionic liquid systems: The influence of imidazolium cation size and anion type on reactivity and thermomechanical properties. Industrial Engineering Chemistry Research, **51**, 5197–5206 (2012).
DOI: 10.1021/ie202321j

[5] Mąka H., Spychaj T., Kowalczyk K.: Imidazolium and deep eutectic ionic liquids as epoxy resin crosslinkers and graphite nanoplatelets dispersants. Journal of Applied Polymer Science, **131**, in press (2014).
DOI: 10.1002/APP.40401

[6] Soares B. G., Livi S., Duchert-Rumeau J., Gerard J. F.: Preparation of epoxy/MCDEA networks modified with ionic liquids. Polymer, **53**, 60–66 (2012).
DOI: 10.1016/j.polymer.2011.11.043

[7] Sanes J., Carrión-Vilches F. J., Bermúdez M. D.: New epoxy-ionic liquid dispersions. Room temperature ionic liquid as lubricant of epoxy resin-stainless steel contacts. e-Polymer, no.005 (2007).
DOI: 10.1515/epoly.2007.7.1.48

[8] Sanes J., Carrión F. J., Bermúdez M. D.: Effect of the addition of room temperature ionic liquid and ZnO nanoparticles on the wear and scratch resistance of epoxy resin. Wear, **268**, 1295–1302 (2010).
DOI: 10.1016/j.wear.2010.01.024

[9] Guo B., Wan J., Lei Y., Jia D.: Curing behaviour of epoxy resin/graphite composites containing ionic liquid. Journal of Physics D: Applied Physics, **42**, 145307/1–145307/8 (2009).
DOI: 10.1088/0022-3727/42/14/145307

[10] Zhang X., Sun H., Yang C., Zhang K., Yuen M. M. F., Yang S.: Highly conductive polymer composites from room-temperature ionic liquid cured epoxy resin: Effect of interphase layer on percolation conductance. Royal Society of Chemistry Advances, **3**, 1916–1921 (2013).
DOI: 10.1039/C2RA23027E

[11] Hameed N., Salim N. V., Hanley T. L., Sona M., Fox B. L., Guo Q.: Individual dispersion of carbon nanotubes in epoxy via a novel dispersion–curing approach using ionic liquids. Physical Chemistry Chemical Physics, **15**, 11696–11703 (2013).
DOI: 10.1039/c3cp00064h

[12] Mąka H., Spychaj T.: Epoxy resin crosslinked with conventional and deep eutectic ionic liquids. Polimery, **57**, 456–462 (2012).
DOI: 10.14314/polimery.2012.456

[13] Silva A. A., Livi S., Netto D. B., Soares B. G., Duchet J., Gérard J. F.: New epoxy systems based on ionic liquid. Polymer, **54**, 2123–2129 (2013).
DOI: 10.1016/j.polymer.2013.02.021

[14] Throckmorton J. A., Watters A. L., Geng X., Palmese G. R.: Room temperature ionic liquids for epoxy nanocomposite synthesis: Direct dispersion and cure. Composites Science and Technology, **86**, 38–44 (2013).
DOI: 10.1016/j.compscitech.2013.06.016

[15] Rogers R. D., Seddon K. R.: Ionic liquids – Solvents od the future? Science, **302**, 792–793 (2003).
DOI: 10.1126/science.1090313

[16] Fukushima T., Kosaka A., Ishimura Y., Yamamoto T., Takigawa T., Ishii N., Aida T.: Molecular ordering of organic molten salts triggered by single-walled carbon nanotubes. Science, **300**, 2072–2074 (2003).
DOI: 10.1126/science.1082289

[17] Nuvoli D., Valentini L., Alzari V., Scognamillo S., Bittolo Bon S., Piccinini M., Illescas J., Mariani A.: High concentration few-layer graphene sheets obtained by liquid phase exfoliation of graphite in ionic liquid. Journal of Materials Chemistry, **21**, 3428–3431 (2011).
DOI: 10.1039/C0JM02461A

[18] Abbott A. P., Capper G., Davies D., Rasheed R. K., Tambyrajah V.: Novel solvent properties of choline chloride/urea mixtures. Chemical Communications, **1**, 70–71 (2003).
DOI: 10.1039/B210714G

[19] Carriazo D., Serrano M. C., Gutierrez M. C., Ferrer M. L., del Monte F.: Deep-eutectic solvents playing multiple roles in the synthesis of polymers and related materials. Chemical Society Reviews, **41**, 4996–5014 (2012).
DOI: 10.1039/c2cs15353j

[20] Wang Z., Yang X., Wang Q., Hahn H. T., Lee S-G., Lee K-H., Guo Z.: Epoxy resin nanocomposites reinforced with ionized liquid stabilized carbon nanotubes. International Journal of Smart and Nano Materials, **2**, 176–193 (2011).
DOI: 10.1080/19475411.2011.594104

[21] Wang Z., Colorado H. A., Guo Z-H., Kim H., Park C-L., Hahn H. T., Lee S-G., Lee K-H., Shang Y-Q.: Effective functionalization of carbon nanotubes for bisphenol F epoxy matrix composites. Materials Research, **15**, 510–516 (2012).
DOI: 10.1590/S1516-14392012005000092

[22] LeMay J. D., Kelley R. N.: Structure and ultimate properties of epoxy resins. Advances in Polymer Science, **78**, 115–148 (1986).

[23] Wan J., Li C., Bu Z-Y., Xu C-J., Li B-G., Fan H.: A comparative study of epoxy resin cured with a linear diamine and a branched polyamine. Chemical Engineering Journal, **188**, 160–172 (2012).
DOI: 10.1016/j.cej.2012.01.134

[24] Putz K. W., Palmeri M. J., Cohn R. B., Andrews R., Brinson C.: Effect of cross-link density on interphase creation in polymer nanocomposites. Macromolecules, **41**, 6752–6756 (2008).
DOI: 10.1021/ma800830p

[25] Zhamu A., Hou Y. P., Zhong W-H., Srone J. J., Li J., Luckhart C. M.: Properties of a reactive-graphitic-carbon-nanofibers-reinforced epoxy. Polymer Composites, **28**, 605–611 (2007).
DOI: 10.1002/pc.20278

[26] Wang J., Fang Z., Gu A., Xu L., Liu F.: Effect of amino-functionalization of multi-walled carbon nanotubes on the dispersion with epoxy resin matrix. Journal of Applied Polymer Science, **100**, 97–104 (2006).
DOI: 10.1002/app.22647

[27] Chanda M., Roy S. K.: Plastics fundamentals, properties and testing. CRC Press, Boca Raton (2009).

[28] Shen M-Y., Kuan C-F., Kuan H-C., Chen C-H., Wang J-H., Yip M-C., Chiang C-L.: Preparation, characterization, thermal, and flame-retardant properties of green silicon-containing epoxy/functionalized graphene nanosheets composites. Journal of Nanomaterials, **2013**, 747963/1–747963/10 (2013).
DOI: 10.1155/2013/747963

[29] Heneczkowski M., Oleksy M., Oliwa R., Dutkiewicz M., Maciejewski H., Galina H.: Application of silsesquioxanes for modification of epoxy resins. Polimery, **58**, 759–765 (2013).
DOI: 10.14314/polimery.2013.759

[30] Liao S-H., Liu P-L., Hsiao M-C., Teng C-C., Wang C-A., Ger M-D., Chiang C-L.: One-step reduction and functionalization of graphene oxide with phosphorus-based compound to produce flame-retardant epoxy nanocomposite. Industrial and Engineering Chemistry Research, **51**, 4573–4581 (2012).
DOI: 10.1021/ie2026647

[31] Berkei M.: Conductive coatings using carbon nanotubes. CHEManager Europe, **7–8**, 10 (2011).

eXPRESS Polymer Letters Vol.8, No.10 (2014) 733–744
Available online at www.expresspolymlett.com
DOI: 10.3144/expresspolymlett.2014.76

The detection of the early stages of ageing in an LDPE + graphite composite by comparison of dielectric responses induced by sinusoidal and triangular signals

I. Petronijević[1], K. Simonović[2], F. Marinković[1], J. Dojčilović[1], A. S. Luyt[3], D. Dudić[3,4]*

[1]University of Belgrade - Faculty of Physics, Studentski trg 12–16, 11001 Belgrade, Serbia
[2]Faculty of Mechanical Engineering, Bogišičeva 8, 1000 Ljubljana, Slovenija
[3]Department of Chemistry, University of the Free State (Qwaqwa Campus), Private Bag X13, 9866 Phuthaditjhaba, South Africa
[4]University of Belgrade – Vinča Institute of Nuclear Sciences, P.O. Box 522, 11001 Belgrade, Serbia

Received 11 March 2014; accepted in revised form 25 May 2014

Abstract. This study describes the possibility of dielectric characterization of the initial stages of ageing in an low-density polyethylene (LDPE) + graphite composite, which is not possible using the standard method of dielectric spectroscopy. It is shown that the differences between the delay angles, $\Delta\varphi = \varphi_{TRI} - \varphi_{SIN}$, obtained using triangular and sinusoidal excitations on the composite samples, shows a maximum, and at the same time the position of this maximum shows more sensitivity to changes in the electrical properties of the material caused by ageing than other dielectric parameters. In order to clarify the applied methodology, a comparative analysis of the dielectric properties of other polymers poly(vinyl chloride) (PVC) and poly(vinyl alcohol) (PVA) and a conductive polymer composite (LDPE + carbon black) with respect to the application of sinusoidal and triangular electrical signals was carried out. Based on the presented results, we believe that the position of the peak in the frequency spectra of the difference between the delay angles obtained by using triangular and sinusoidal signals may be a suitable parameter for the dielectric characterization of polymeric materials.

Keywords: *polymer composites, triangular wave signal, dielectric, delay angle, ageing*

1. Introduction

Various forms of degradation of polymeric materials and their composites represent an important factor that reduces their usability. The most common causes of changes in the properties of polymeric materials are: application of mechanical stress [1]; elevated temperature [2, 3]; exposure to electromagnetic radiation of high energy [4, 5]; presence of slowly varying electric fields [6]; contact with aggressive chemicals [7]. The changes in polymeric materials resulting from aforementioned factors can be classified into two groups. The first group consists of chemical changes such as oxidation processes, changes in molecular weight or other chemical reactions, and the second group involves the physical changes in the structure of the polymer or polymer composite, including phase transitions, changes in crystallinity, rearrangement of the amorphous phase and redistribution of fillers [8]. In most cases the physical and chemical processes occur together and affect each other.

A number of standards were developed that prescribe the methodology of investigation of degradation effects on the physico-chemical properties of these materials. Regardless of their application, polymeric materials are expected to have good

*Corresponding author, e-mail: ddudic@vinca.rs

mechanical properties, even after ageing. Among other properties such as chemical resistance, toxicity, optical properties and thermal stability, changes in electrical properties are important for polymer materials that are used in electronics or as electrical insulating materials. It has been shown that in cases where changes of electrical properties due to ageing are not of primary importance, their changes can still be correlated with, for example, changes in mechanical properties [9]. Most of the methods that examine the properties of the material show a relative measurement error of about 1%, but in some cases this error can be much higher as is the case with stress-strain measurements or lower in density measurements. This measurement error is not a problem when examining the effect of ageing, which significantly changes the properties of the material. There is however a need to detect the initial stages of changes in material properties, which are important in, for example, electrical insulation materials, where the measuring sensitivity of the applied method becomes extremely important.

Electrical measurements have an important place in the field of materials characterization, and the measurement of the frequency spectra of AC conductivity provides more information than the DC conductivity measurement. DC measurement gives only one value, resistivity or conductivity, while dielectric measurements provide two parameters, such as amplitude of conductivity and delay angle, and also their frequency dependence. The dielectric measurement can also be improved by changing the shape of the excitation signal, which is what is presented in this article. The application of the sine wave electrical test signal in the investigation of the dielectric properties of polymers is a standard procedure in polymer science [10–12]. The other waveforms of a test signal are rarely used in the analysis of the electrical properties of polymers [13, 14], but they are used for the testing of energy transformers as well as for various electronic and mechanical tests [15–18]. It is well known that the dielectric relaxations in polymers occur over broad intervals of frequencies and/or temperatures, which sometimes makes difficult to precisely establish the dielectric parameters and the exact position of the processes (they are simply too broad to be noticed). The application of sinusoidal excitation allows the presentation of AC conductivity (admittance) and AC resistance (impedance) in a complex mathematical form. The real and imaginary parts of admittance and impedance, and the complex permittivity ($\varepsilon^* = \varepsilon' - i\varepsilon''$) and angle δ (usually $\tan\delta$) are the dielectric parameters that are commonly used to describe the dielectric relaxation in polymers. In some cases the dielectric relaxation of polymers is clearly observed in the temperature and frequency dependencies of electrical modulus ($M^* = 1/\varepsilon^*$), as well as appropriate derivations of the AC conductivity [19] or permittivity [11].

In the present study we used, besides the sine wave signal, a triangular test signal to investigate the early stages of ageing in an LDPE + graphite composite which was subjected to high oxygen pressure at room temperature. It was shown that the difference between the delay angles obtained by applying different excitations waveforms, triangular and sinusoidal, shows a maximum whose position on the frequency scale was very sensitive to changes in the electrical properties of the composites. In order to describe the applicability of the method to other polymer systems, we also analyzed some typical polymers (PVC and PVA) and a conductive polymer composite (LDPE + carbon black (CB)).

2. Experimental

2.1. Materials

PVC – The poly(vinyl chloride) sample was a commercial PVC cling film obtained from Shanghai StarLight Plastics Limited.

PVA – Merck-Alkaloid, art.821038.

LDPE – PE552, HIP Pančevo, Serbia, M_w = 110 000 and ρ = 0.922 g/cm^3.

The carbon black (ellipsoidal shape, diameter 3–5 μm) and graphite flakes (about 10 μm) were obtained from the Laboratory for Thermal Engineering and Energy, Vinča Institute of Nuclear Sciences, Serbia.

2.2. Samples preparation

PVC samples of 210×150 mm and thickness d = 0.01 mm were cut from the middle of the sheets.

The poly(vinyl alcohol) sample was obtained from an aqueous PVA solution (1.5 mass%). The polymer was dissolved in boiling distilled water and mixed at 6000 rpm for 120 minutes. In order to get solid films, the solution was placed into a Petri dish and dried in a vacuum oven at 40°C for 24 h. The sample was in the form of disk with diameter D = 53 mm and thickness d = 0.11 mm.

LDPE + 20 wt% carbon black and LDPE + 30 wt% graphite composites were obtained in a Haake rheometer at 433 K for 10 min. The isotropic sheets were prepared by compression molding at 460 K and a pressure of 1.75 MPa for 5 min, followed by quenching in water at room temperature. The LDPE + graphite composites were gamma irradiated in a ^{60}Co radiation facility, in air at room temperature, at a dose rate of 6 kGy/h (100 and 200 kGy). The accelerated ageing was performed at 22°C in an Emmerson single vessel oxygen apparatus at 0.5 MPa. Samples of 50×50 mm and thickness d = 1 mm were cut from the middle of the sheets.

Electrical measurements were made more than 30 days after the mentioned treatments of the composites. Electrical contacts on the samples were made by fine copper powder.

2.3. Methods

The dielectric measurements were performed on a Tektronix TDS 2022B oscilloscope. An Agilent 33220A 20 MHz function/arbitrary wave form generator was used as the voltage source. An amplitude of 7.8 V was applied and the frequency range was 0.005 Hz–160 kHz. The sample cell was housed in a Faraday cage and measurements were done at room temperature (normal pressure and 50% relative humidity). The experimental set-up is shown in Figure 1.

In the measurement procedure, the electrical current through the sample was monitored via the resistor R in Figure 1 (capacity less than 10^{-11} F). The presence of this resistor might have induced distortion of the triangular signal applied to the sample. For this reason, the values of R were changed in such a way to ensure that the voltage drop across the resistor did not exceed 1% of the input voltage of the function generator. The electrical current through the sample cell was calculated as $I(t) = U_{CH_2}(t)/R$, while the voltage on the sample was determined as $U_S(t) = U_{CH_1}(t) - U_{CH_2}(t)$. The reported results were obtained after the correction $I_S(t) = I_M(t) - I_B(t)$ was applied, where $I_S(t)$ is the current through the sample, $I_M(t)$ the current measured with a sample in the cell, and $I_B(t)$ the current in the empty cell without the upper cell electrode. The value of the current at each particular frequency (f) was determined as the average value over the time interval that lasted at least $10/f$. Relative values of the standard deviation of the obtained parameters were up to 2%, and they did not change significantly with respect to the change in input signals. Electrical DC conductivity measurements were performed using an Agilent 4339B high resistance meter at room temperature, and applying an electric field of 100 V/mm for 20 min.

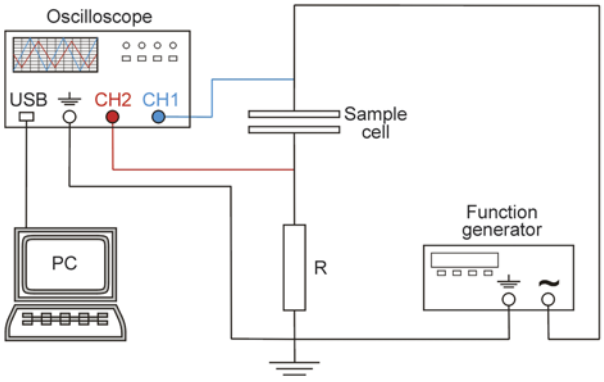

Figure 1. Block diagram of the experimental set-up

The results of measurements with sinusoidal excitation were related to the well-known current phase diagram in Figure 2a (I_0 is the amplitude of the current). In contrast to the current amplitude obtained by application of the sinusoidal voltage, the amplitudes of the current obtained by application of a triangular waveform are always in phase with the voltage amplitude. Because of that, the delay angle was determined under the condition $I(t_2) = V(t_1) = 0$ as shown in Figure 2b. The amplitude of the conductivity was defined as $Y_0 = I_0/U_0$ for both waveforms, where U_0 and I_0 are the maximum values of the measured voltage and current, respectively. Data processing was performed in a script program originally designed for this purpose.

3. Results and discussion

3.1. Dielectric response of PVC, PVA and LDPE + CB

A comparison of the dielectric properties of polymers with the appropriate RC circuit models has already been presented in the literature [10–12]. We presented in the appendix of this paper an analysis of the electrical responses of serial and parallel RC circuits due to sinusoidal and triangular voltage excitations. Comparison of the dielectric response of RC circuits to sine and triangular excitation indicates that the angle of the triangular signal delay is always greater than or equal to the appropriate angle obtained by applying sinusoidal signals ($\Delta\varphi(f) = \varphi_{TRI} - \varphi_{SIN} \geq 0$). One reason for this is that the response (current) of RC circuits to sine (voltage)

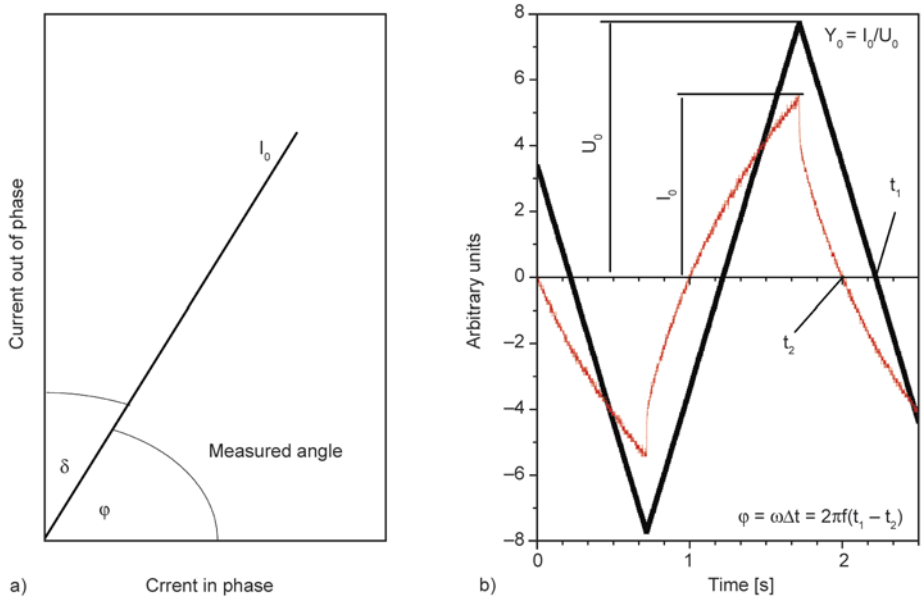

Figure 2. a) Current phase diagram for sinusoidal excitation; b) the response of PVA to triangular excitation at 0.5 Hz

excitation also has a sinusoidal shape with a unique, time-independent delay angle, while the response of the RC circuits to triangular excitation has a complex frequency-dependent form, the amplitude of which is always in phase with the excitation. The phase deviation of the measured current of triangular excitation, due to the existence of a capacity, is the largest in the intersection of the measured current with the time axis (Figure 2b). This is used to determine delay angle for this form of excitation. In addition, numerical analysis shows that in the cases of ideal serial and parallel RC circuits there is a well defined peak of the function $\Delta\varphi(f)$ (Figures 9a and 10a). The position of the maximum in the difference between the delay angles in the frequency spectrum, $\Delta\varphi(f) = \varphi_{TRI} - \varphi_{SIN}$, obtained using triangular and sinusoidal excitation for ideal electrical circuits, can be related to the RC constant of the circuits (fo in Table 1). This gave us the idea to use the frequency, that corresponds to the maximum of $\Delta\varphi(f)$, to describe the electrical properties of polymers. In this section, the behaviour of the real polymer systems was tested on two polymers, PVC as a representative electrically non-conductive polymer, PVA that can then be considered as a semiconductor, and an LDPE + 20 wt% CB composite with relatively high electrical conductivity.

Figure 3 shows the results obtained after the application of sinusoidal and triangular signals to the PVC sample. The loss tangent of PVC (Figure 3a)

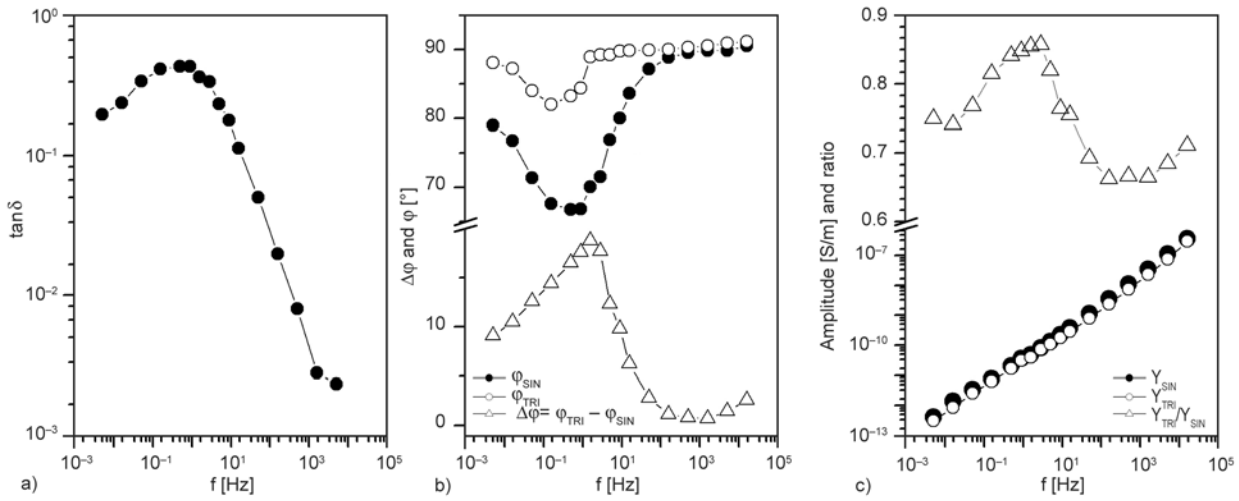

Figure 3. a) Loss tangent ($\tan\delta_{SIN}$), and the curves of b) differences in delay angles and c) amplitude ratios for polyvinyl chloride (PVC). The results were obtained experimentally by application of sinusoidal and triangular signals to the sample.

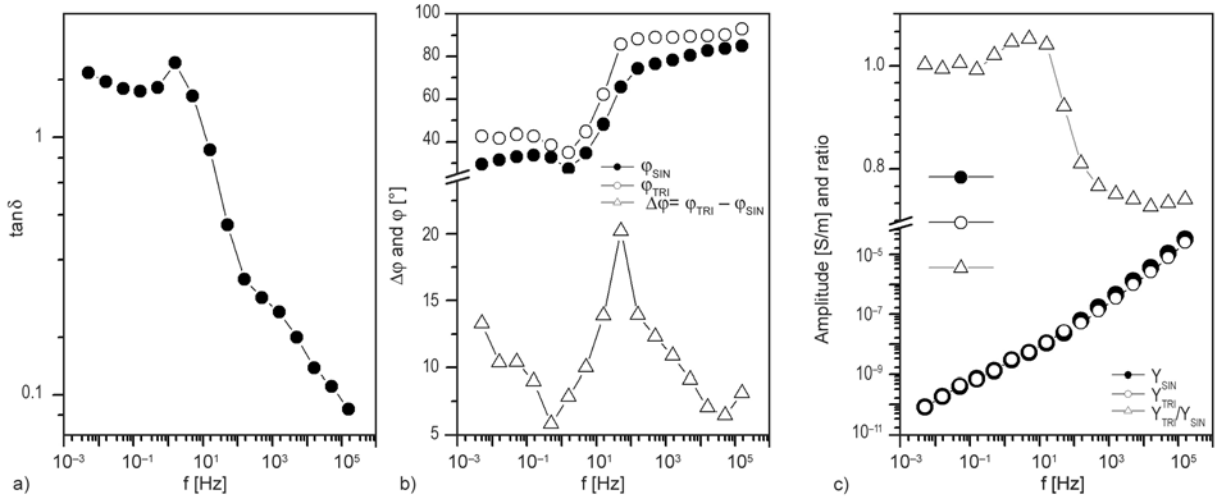

Figure 4. a) Loss tangent ($\tan\delta_{SIN}$), and the curves of b) differences in delay angles and c) amplitude ratios for polyvinyl alcohol (PVA). The results were obtained experimentally by application of sinusoidal and triangular signals to the sample.

shows a peak around 1 Hz attributable to the β relaxation [20]. In addition to the β relaxation, the curve of the differences in delay angles ($\Delta\varphi = \varphi_{TRI} - \varphi_{SIN}$) also exhibits a peak at frequency $f_0 \sim 1.5$ Hz (Figure 3b) in the observed frequency range in PVC sample, as was suggested by the mathematical considerations on RC circuits (Figures 9a and 10a). The ratio between the amplitudes of conductivity at low frequencies is lower than 1 ($Y_{TRI}/Y_{SIN} < 1$) and has a peak at about 0.9 Hz (Figure 3c).

The loss tangent of PVA (Figure 4a) shows a small maximum at 1.5 Hz. A peak is clearly observable in the curve of angle differences ($\Delta\varphi = \varphi_{TRI} - \varphi_{SIN}$) with the maximum positioned at $f_0 \sim 50$ Hz (Figure 4b). The ratios of the amplitudes at low frequencies are close to 1 and the peak is at ~ 5 Hz (Figure 4c). The best agreement with the parallel RC circuit model was noticed in the composite of LDPE filled with 20% of carbon black. The loss tangent of the LDPE + CB composite shows a nearly linear dependence on frequency in the log-log scale (Figure 5a). The curve of the differences between the delay angles obtained by using sinusoidal and triangular excitation (Figure 5b) is similar to the results obtained mathematically on the parallel RC circuit (Figure 9a). Figure 5c also shows that the ratio of the amplitudes of conductivity corresponds well with the results in Figure 9b. The characteristic frequencies obtained for the composite were $f_0 \sim 5$ kHz and about 500 Hz for the maximum in amplitude ratio. The RC time constants of the samples estimated according to the model of a parallel RC circuit

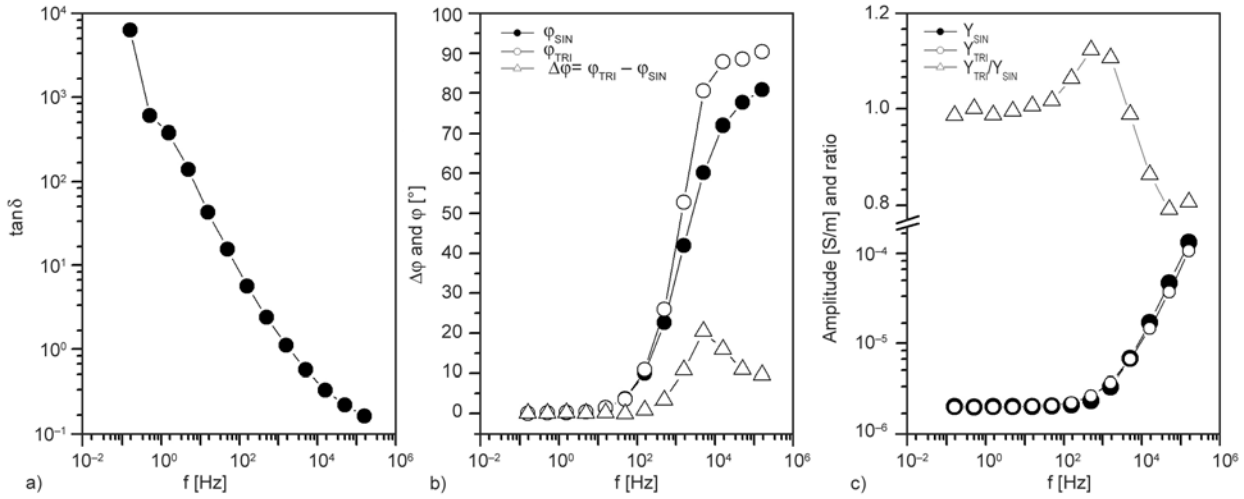

Figure 5. a) Loss tangent ($\tan\delta_{SIN}$), and the curves of b) differences in delay angles and c) amplitude ratios for the composite LDPE filled with 20% of carbon black. The results were obtained experimentally by application of sinusoidal and triangular signals to the sample.

(Table 2) and the corresponding DC conductivities are shown in Table 1. As can be seen, as the DC conductivity of the polymers or composites increases, the value f_0 also increases, which is in accordance with the established dependence of this quantity in terms of the idealized models of polymers according to the parallel and serial RC circuits ($f_0 \sim 1/R$). The mentioned models also point to a more complex dependence, e.g. $f_0 \sim 1/(RC)$ (Table 2). It is obvious that this parameter shows the biggest sensitivity to changes in polymer properties that are subject both to an increase in conductance (resistance decrease) and a decrease in capacity, or vice versa. A good example of this is the process of grouping the conductive particles in conductive paths in polymer composites, during which part of the capacitive contact switches to direct contact, giving rise to a decrease in capacity and an increase in conductance. Since the true $\varphi_{SIN} = f(RC,\omega)$, the same is true for the sensitivity of the delay angle (or $\tan(\pi/2 - \varphi_{SIN})$). However, f_0 is an integral parameter that does not depend on the frequency and describes the dielectric properties of the material in a wider range of frequencies. This is probably one of the reasons why it is more sensitive to changes in the dielectric properties of the material then the delay angle. It should be noted that for the detection of processes with opposite changes in resistance and capacitance in polymer materials ($RC \approx$ const), the admittance (or impedance) amplitude may be more suitable than the delay angle.

The results in Figures 3, 4 and 5 clearly show that application of sinusoidal and triangular signals enables one to draw additional information about the dielectric properties of real polymers samples. The curve of differences in delay angles ($\Delta\varphi = \varphi_{TRI} - \varphi_{SIN}$) shows a well defined peak, even when the loss tangent implies more complex dielectric properties for a particular polymer. It should be noted that the methodology presented here may be used to also study other physical properties of polymers. For example, it has been shown that electroluminescence of polymers induced by AC electrical signals exhibits a time shift, depending on the waveform signal applied [13].

Table 1. Experimentally determined f_0 and RC time constants calculated by the model of a parallel RC circuit (Table 3), and DC conductivities of the polymers and composite

Sample	f_0 [Hz]	$RC = 1/4f_0$ [s]	σ_{DC} [S/m]
PVC	1.58	0.156	$1.2\cdot10^{-15}$
PVA	50	0.005	$3.3\cdot10^{-12}$
LDPE+CB	5000	0.00005	$2.1\cdot10^{-6}$

3.2. Changes in the dielectric properties of the LDPE + graphite composite induced by ageing

As was noted previously, the frequency (f_0) which corresponds to the maximum of the $\Delta\varphi(f) = \varphi_{TRI} - \varphi_{SIN}$ curve could be a suitable parameter to describe the changes in the electrical properties of polymers. As an example of this, Figure 6 shows the effect of gamma irradiation on the dielectric properties of an LDPE + graphite composite. Radiation-induced processes of oxidation, networking and grafting in the composite increases its electrical conductivity [21], and these changes in the composite also affect the maximum of the $\Delta\varphi(f)$ (Figure 6a) and tangent loss (Figure 6b) curves. The dominant effect of a gamma radiation dose of about 100 kGy is the networking of chains in the polyethylene matrix. The application of higher doses (200 kGy) leads to significant degradation of the crystal domains, in addition to networking, which is reflected by the electrical [21] and the mechanical properties [22]. The results shown in Figure 6 are in line with this influence of gamma radiation on the LDPE + carbon based composites. Unlike the composite samples exposed to gamma radiation in air, the physical and chemical changes in the composite samples that were aged at room temperature in high pressure oxygen for several days were significantly less.

The use of elevated temperature and oxygen pressure (thermo-oxidative ageing) is a frequently applied method of accelerated ageing of the polymeric materials to predict their lifetime. The degradation mechanism of thermo-oxidative ageing can be described through physical changes, densification and shrinkage, that are directly related to the thermo-mechanical history of the material, as well as surface chemical degradation with the formation of microcracks, and chemical changes in the sample [23]. Thermo-oxidative ageing usually causes degradation of mechanical properties but in some cases, such as reticulated resins, can lead to an improvement in these properties due to the subsequent process of networking [24]. The changes in electrical characteristics caused by these processes are very complex and diverse [6–9]. In the existing literature

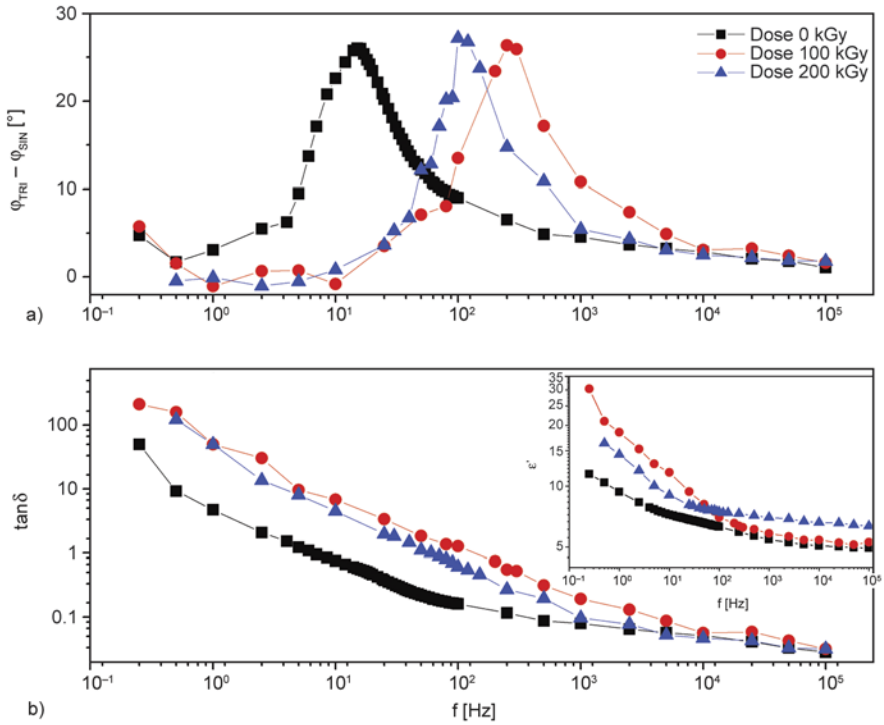

Figure 6. The effect of gamma irradiation on the dielectric properties of the LDPE+graphite composite: a) the curves of differences in delay angles and b) loss tangent ($\tan\delta_{SIN}$) and permittivity (inset)

there is no evidence that the accelerated ageing that we applied to the LDPE + graphite composite (up to 4 days at room temperature ageing at high oxygen pressure) caused noticeable chemical or physical changes. We also could not detect such changes in the permittivity and loss tangent curves of these samples outside the experimental error (±1%). However, in the curves of the difference between the delay angles the initial ageing stage of the composites is clearly visible.

Figure 7a shows the frequency dependence of loss tangent and Δφ of the LDPE + graphite composite which was subjected for different periods up to 4 days to oxygen at a high pressure at room temperature. While the loss tangent shows no significant differences due to the effect of ageing, there is a clear shift in the position of the maximum in the Δφ(*f*) curves. The magnified part of Figure 7a is presented in Figure 7b. We emphasize that both the delay angles (φ_{TRI} and φ_{SIN}) were measured in the same experimental setup and with the same relative error of about 1%. The results suggest that the position of the maximum in the $\Delta\varphi(f) = \varphi_{TRI} - \varphi_{SIN}$ curves (φ_{TRI} and φ_{SIN} are measured by applying tri-

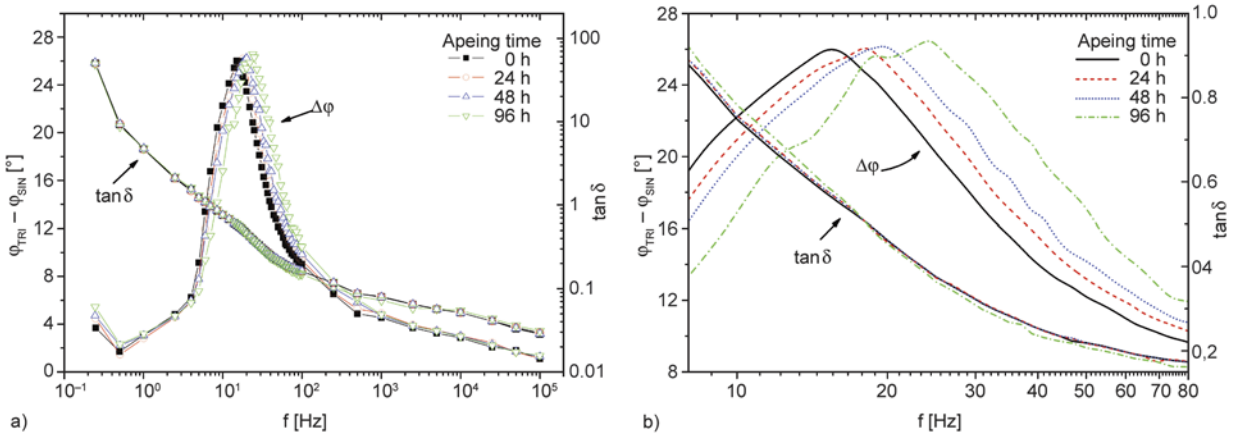

Figure 7. The effect of accelerated ageing on the dielectric properties of the LDPE+graphite composite: a) loss tangent ($\tan\delta_{SIN}$) and Δφ; b) the magnified part of the picture in a)

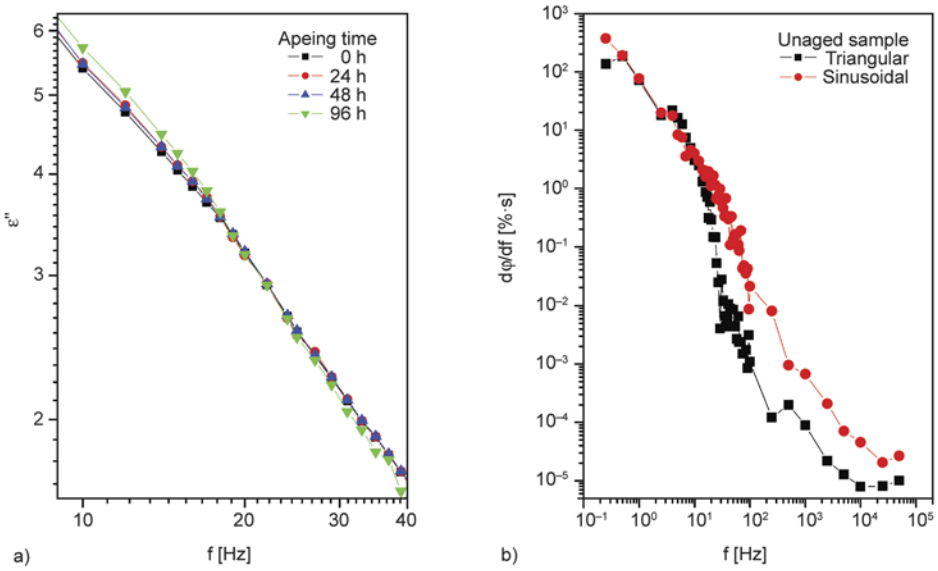

Figure 8. a) Imaginary part of permittivity of aged composite samples; b) normalised derivation of delay angles per frequency for unaged sample

angular and sinusoidal voltage respectively) shows more sensitivity to changes in the electrical properties of LDPE + graphite, due to ageing, than other dielectric parameters. These changes could also not be observed in the values of permeability (Figure 8a), and there is also no evidence of these changes in the dependence of the derivation of the delay angles versus frequency (Figure 8b), because of big errors in these results.

As previously stated, there is no indication that the ageing treatment that we applied causes significant physical and chemical changes in the LDPE + graphite composite. In addition to the possible oxidation process, we believe that the observed shift in the value of f_0 is a consequence of compressive pressure and thereby induced structural relaxation in the samples during treatment rather than chemical changes. Bearing in mind the modeled dependence $f_0 \sim 1/(RC)$ (Table 2), the analysis of only this parameter cannot give conclusive evidence on whether the increase in f_0 with ageing time resulted from an increased number and/or quality of the direct contacts between the graphite particles in LDPE. However, based on existing experience such an increase is expected [8]. Since the change in amplitude of the conductivity caused by the oxygen ageing is also within experimental error, only one conclusion can be drawn, and that is that the observed increase in f_0 with increasing ageing time indicates a decrease in the delay angle φ_{SIN} (parallel RC circuit), i.e. an increase in δ (and also $\tan\delta$) in the frequency spectrum. This can be concluded on the basis of the dependence $f_0 \sim 1/(RC)$ and the expression for φ_{SIN} under the condition ω = const in the model of a parallel RC circuit (Table 2). The same result is obtained by considering f_0 and the delay angle in the model serial RC circuit.

4. Conclusions

We investigated the dielectric properties of different polymer systems with respect to the application of sinusoidal and triangular input signals. Our study also describes the possibility of dielectric characterization of the initial stages of ageing in a low-density polyethylene + graphite composite using comparison of the delay angles obtained by triangular and sinusoidal voltage excitations. The differences in the results obtained with these two signal excitations were first studied by simulation on parallel and serial RC circuits (see Appendix). The curve of the differences in delay angles ($\Delta\varphi = \varphi_{TRI} - \varphi_{SIN}$) obtained by the differently shaped input signals shows a peak with a well defined position of the maximum. The frequency that corresponds to this maximum can be related to the RC time constant (RC) of the circuits by the simple formulas $f \approx 1/(4RC)$ for a parallel and $f \approx 1/(7.2RC)$ for a serial RC circuit. All the tested polymers (PVC and PVA) and polymer composites (LDPE + CB and LDPE + graphite) show a well-defined peak in the $\Delta\varphi(f)$ spectra. Through the use of this method we discovered early ageing processes in an LDPE + graphite composite that could not be detected by conventional dielectric spectroscopy methods. Our results

suggest that the position of the maximum in the $\Delta\varphi(f) = \varphi_{TRI} - \varphi_{SIN}$ curves (φ_{TRI} and φ_{SIN} are measured by applying triangular and sinusoidal voltage respectively) is more sensitive to changes in the electrical properties of polymer materials then angle δ (or $\tan\delta$). We think that the proposed methodology could find industrial application, for example, in early stage detections of ageing in electrical insulation and transformer oils or for the purpose of monitoring other physical or chemical changes in materials.

Appendix

The basic equations that characterise the parallel and serial RC circuit in terms of the application of the sinusoidal and triangular signals are given in Table 2. AC currents $i(t)$, that are shown in Table 2, are obtained by applying the differential equations for the RC circuits on the expression for the triangular wave voltage which are also presented in the same table.

The analysis of the responses of serial and parallel RC circuits was done by using software that was specifically designed for this purpose, and some of these results were checked by measurements on different RC circuits, which confirms the validity of the applied equations and software operation.

Two basic parameters were studied: the amplitude of AC conductivity (Y) or AC resistivity (Z) and delay angle (φ) (see Figure 2). The amplitudes (Y and Z) and delay angles (for both applied waveforms) were presented for four different values of R and C, but keeping their product constant in Figure 9 for parallel and in Figure 10 for serial RC circuits ($RC(1)$, $RC(2)$, $RC(3)$ and $RC(4)$ are presented in Table 3). As for a sinusoidal signal (Table 2), the delayed angle upon triangular excitation on serial and parallel RC circuits depended on the time constant but not on the individual values of R and C. For this reason we presented only the results for $RC(1)$ in Figures9a and 10a. It is clear that the delayed angles for these two signals differ in the narrow range of intermediate frequencies (around 1 kHz), while their difference, $\Delta\varphi = \varphi_{TRI} - \varphi_{SIN}$, exhibits a peak of about 33° for parallel and 9° for serial circuits at the corresponding frequencies f_0. It was found that this frequency can be related to the circuit time constant (RC) by the empirical formulas shown in Table 2. The results shown in Figures 9, 10 and 11 were also verified by experimental measurements.

The amplitudes of admittance (AC conductivity) of both signals for the parallel RC circuit (Figure 9b) are almost inseparable at low frequencies ($f <<$

Table 3. RC circuits and corresponding parameters for dielectric analyses presented in Figures 9, 10 and 11

N°	R [Ω]	C [μF]	RC [10^{-4} s]
1	1737.5	0.1036	1.80005
2	1491.5	0.1207	1.80069
3	1191.5	0.1509	1.79881
4	978.5	0.1839	1.79946
5	2990.1	0.0386	1.15414
6	703.5	0.3271	2.30044

Table 2. The corresponding equations for parallel and serial RC circuit

	Parallel RC circuit	Serial RC circuit
Differential equations	$i(t) = \frac{u(t)}{R} + C\frac{\mathrm{d}u(t)}{\mathrm{d}t}$	$i(t) = C\frac{\mathrm{d}u_C(t)}{\mathrm{d}t} = \frac{u_R(t)}{R}$
Delay angle upon sinusoidal coercion	$\varphi_{SIN} = \frac{\pi}{2} - \arctan\frac{1}{RC\omega}$	$\varphi_{SIN} = \frac{\pi}{2} - \arctan RC\omega$
Amplitude of admittance or impedance	$Y_{SIN} = \sqrt{\frac{1}{R^2} + (C\omega)^2}$	$Z_{SIN} = \sqrt{R^2 + \left(\frac{1}{C\omega}\right)^2}$
Triangular signal	$u(t) = \frac{8u_0}{\pi^2}\sum_{k=0}^{\infty}\frac{\cos[(2k+1)\omega t]}{(2k+1)^2}$	
$i(t)$ – Current in circuit upon triangular coercion	$\frac{8u_0}{R\pi^2}\sum_{k=0}^{\infty}\frac{\cos[(2k+1)\omega t] - RC\omega(2k+1)\sin[(2k+1)\omega t]}{(2k+1)^2}$	$\frac{8u_0}{R\pi^2}\sum_{k=0}^{\infty}\frac{\cos[(2k+1)\omega t] - \frac{1}{RC\omega(2k+1)}\sin[(2k+1)\omega t]}{(2k+1)^2 + \left(\frac{1}{RC\omega}\right)^2}$
f_0 – Frequency that corresponds to a maximum difference between delay angles, $\varphi_{TRI} - \varphi_{SIN}$ in range $f_0 \in$(0.01 Hz, 100 kHz)	$\frac{1}{f_0RC} = 4.06\pm0.03 \Rightarrow f_0 \approx \frac{1}{4RC}$	$\frac{1}{f_0RC} = 7.2\pm0.08 \Rightarrow f_0 \approx \frac{1}{7.2RC}$

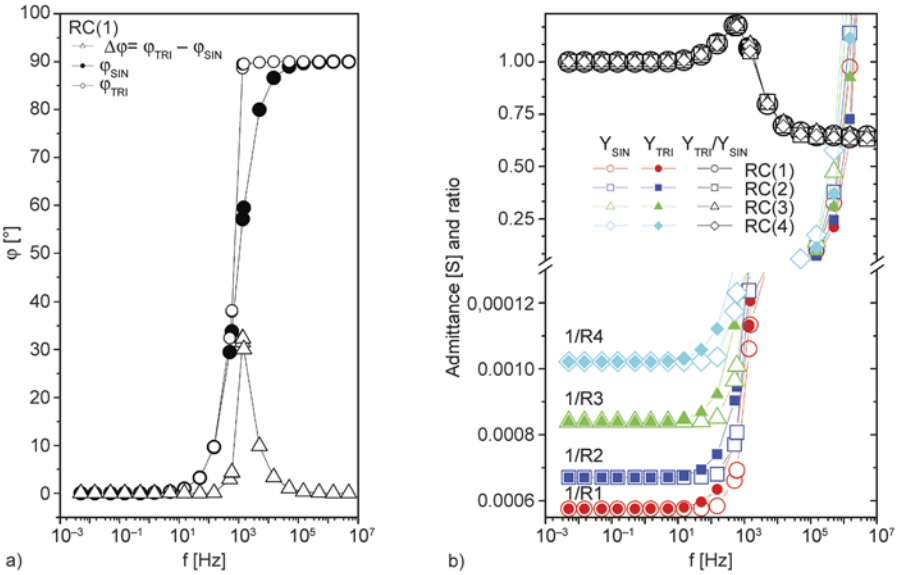

Figure 9. a) Delay angles and b) the amplitudes of admittance obtained by software simulation on parallel RC circuits with the four equal time constants *RC* (*R* and *C* values were altered and stated in Table 3). In the case of delay angles, the results for *RC*(1) were presented, since the calculations with other time constants gave identical values.

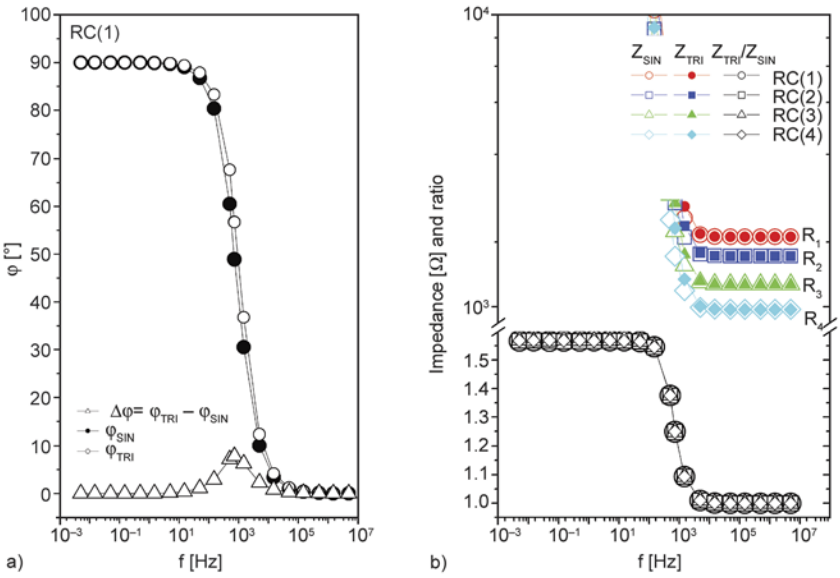

Figure 10. a) Delay angles and b) the amplitudes of impedance obtained by software simulation on serial RC circuits with the four equal time constants *RC* (*R* and *C* values were altered and stated in Table 1). In the case of delay angles, the results for *RC*(1) were presented, since the calculations with other time constants gave identical values.

$1/RC$) and $Y_{TRI} = Y_{SIN} = 1/R$ for each particular resistivity. However, they do differ at higher frequencies ($f >> 1/(RC)$), with the Y_{TRI}/Y_{SIN} ratio approaching ~0.64. In the case of the impedance amplitude in serial RC circuits the relation $Z_{TRI} = Z_{SIN} = R$ at $f >> 1/(RC)$ is also true (Figure 10b).

Figure 11 shows the values of the differences in the delay angles and amplitude ratios for both the input signals calculated (for the parallel RC model) by using the different time constants *RC*(3), *RC*(5) and *RC*(6) from Table 3, as well as the loss tangent for the sinusoidal signal calculated for the same constants. Figure 11a shows that the dependence of tan δ ($\delta = \pi/2 - \varphi_{SIN}$) on frequency is a straight line in the log-log scale with a slope equal to –1. At the same time, the curves of Y_{TRI}/Y_{SIN} and Δφ exhibit maxima that shift towards lower frequencies with increasing time constant. Similar results were obtained for the case of differences in delay angles for a serial RC circuit.

Acknowledgements

This work was supported by the Ministry of Education and Science, Republic of Serbia (Project No. 171029).

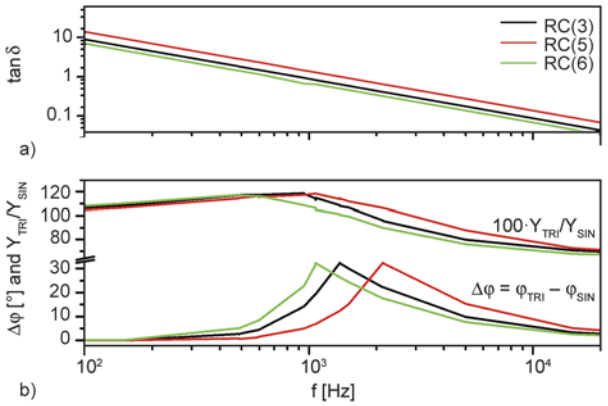

Figure 11. The results obtained by using different time constants: *RC*(4), *RC*(5) and *RC*(6) in Table 3 on parallel RC circuit. a) Loss tangent (tan δ) and b) the curves of differences in delay angles and amplitude ratios (as indicated in figure).

References

[1] Struik L. C. E.: The mechanical and physical ageing of semicrystalline polymers: 1. Polymer, **28**, 1521–1533 (1987).
DOI: 10.1016/0032-3861(87)90353-3

[2] Wiles M. D., Scott G.: Polyolefins with controlled environmental degradability. Polymer Degradation and Stability, **91**, 1581–1592 (2006).
DOI: 10.1016/j.polymdegradstab.2005.09.010

[3] Dudić D., Djoković V., Kostoski D.: The high temperature secondary crystallisation of aged isotactic polypropylene. Polymer Testing, **23**, 621-627 (2004).
DOI: 10.1016/j.polymertesting.2004.01.015

[4] Wu Q., Qu B., Xu Y., Wu Q.: Surface photo-oxidation and photostabilization of photocross-linked polyethylene. Polymer Degradation and Stability, **68**, 97–102 (2000).
DOI: 10.1016/S0141-3910(99)00171-8

[5] Djoković V., Kostoski D., Dramićanin M., Dudić D.: Effects of gamma irradiation on the stress relaxation of drawn ultrahigh molecular weight polyethylene. Radiation Physics and Chemistry, **55**, 605–607 (1999).
DOI: 10.1016/S0969-806X(99)00255-8

[6] Sakamoto W. K., Perez D. J., Das-Gupta D. K.: On the characterisation of electrically stressed polyethylene before and after chemical treatment. Journal of Materials Science, **37**, 1295–1300 (2002).
DOI: 10.1023/A:1014547907534

[7] Simonović K., Petronijević I., Kostoski D., Dojčilović J., Luyt S. A., Dudić D.: Effects of acid treatment at different temperatures on the surface dielectric properties of low-density polyethylene. Polymer International, in press (2014).
DOI: 10.1002/pi.4731

[8] Vu Q. D., Gigliotti M., Lafarie-Frenot C. M.: Experimental characterization of thermo-oxidation-induced shrinkage and damage in polymer–matrix composites. Composites Part A: Applied Science and Manufacturing, **43**, 577–586 (2012).
DOI: 10.1016/j.compositesa.2011.12.018

[9] Sun Y., Luo S., Watkins K., Wong P. C.: Electrical approach to monitor the thermal oxidation aging of carbon black filled ethylene propylene rubber. Polymer Degradation and Stability, **86**, 209–215 (2004).
DOI: 10.1016/j.polymdegradstab.2004.04.013

[10] Hedvig P.: Dielectric spectroscopy of polymers. Akadémiai Kiadó, Budapest (1977).

[11] Asami K.: Characterization of heterogeneous systems by dielectric spectroscopy. Progress in Polymer Science, **27**, 1617–1659 (2002).
DOI: 10.1016/S0079-6700(02)00015-1

[12] Boyd H. R.: Relaxation processes in crystalline polymers: Experimental behaviour – A review. Polymer, **26**, 323–347 (1985).
DOI: 10.1016/0032-3861(85)90192-2

[13] Baudoin F., Mills D. H., Lewin P. L., Le Roy S., Teyssedre G., Laurent C.: Modeling electroluminescence in insulating polymers under AC stress: Effect of excitation waveform. Journal of Physics D: Applied Physics, **44**, 165402/1–165402/11 (2011).
DOI: 10.1088/0022-3727/44/16/165402

[14] Suwarno: Role of applied voltage waveforms on partial discharge patterns of electrical treeing in low density polyethylene. International Journal of Electrical and Power Engineering, **3**, 184–190 (2009).

[15] Janssen R. P. M., Govaert L. E., Meijer H. E. H.: An analytical method to predict fatigue life of thermoplastics in uniaxial loading: Sensitivity to wave type, frequency, and stress amplitude. Macromolecules, **41**, 2531–2540 (2008).
DOI: 10.1021/ma071274a

[16] Gasulla-Forner M., Jordana-Barnils J., Pallas-Areny R., Torrents J. M.: Subsurface resistivity measurements using square waveforms. IEEE Transactions on Instrumentation and Measurement, **47**, 74–77 (1998).
DOI: 10.1109/19.728793

[17] Bailey J. J.: The triangular wave test for electrocardiographic devices: A historical perspective. Journal of Electrocardiology, **37**, 71–73 (2004).

[18] Creason S. C., Hayes J. W., Smith D. E.: Fourier transform faradaic admittance measurements III. Comparison of measurement efficiency for various test signal waveforms. Journal of Electroanalytical Chemistry and Interfacial Electrochemistry, **47**, 9–46 (1973).
DOI: 10.1016/S0022-0728(73)80343-2

[19] Dudić D., Škipina B., Dojčilović J., Novaković L., Kostoski D.: Effects of charge trapping on the electrical conductivity of low-density polyethylene–carbon black composites. Journal of Applied Polymer Science, **121**, 138–143 (2011).
DOI: 10.1002/app.33421

[20] Elícegui A., Del Val J. J., Millán L. J., Mijangos C.: α and β relaxation processes in internally plasticized poly (vinylchloride). Journal of Non-Crystalline Solids, **235–237**, 623–627 (1998).
DOI: 10.1016/S0022-3093(98)00664-4

[21] Balabanov S., Krezhov K.: Electrical conductivity and electrostatic properties of radiationally modified polymer composites with carbon black. Journal of Physics D: Applied Physics, **32**, 2573–2577 (1999).
DOI: 10.1088/0022-3727/32/19/315

[22] Suarez J. C. M., Monteiro E. E. C., Mano E. B.: Study of the effect of gamma irradiation on polyolefins – Low-density polyethylene. Polymer Degradation and Stability, **75**, 143–151 (2002).
DOI: 10.1016/S0141-3910(01)00213-0

[23] Tsotsis K. T., Keller S., Bardis J., Bish J.: Preliminary evaluation of the use of elevated pressure to accelerate thermo-oxidative aging in composites. Polymer Degradation and Stability, **64**, 207–212 (1999).
DOI: 10.1016/S0141-3910(98)00190-6

[24] Middleton J., Burks B., Wells T., Setters M. A., Jasiuk I., Kumosa M.: The effect of ozone and high temperature on polymer degradation in polymer core composite conductors. Polymer Degradation and Stability, **98**, 2282–2290 (2013).
DOI: 10.1016/j.polymdegradstab.2013.08.013

eXPRESS Polymer Letters Vol.8, No.10 (2014) 745–755
Available online at www.expresspolymlett.com
DOI: 10.3144/expresspolymlett.2014.77

Self-assembly of nanostructures obtained in a microwave-assisted oxidative polymerization of aniline

M. R. Gizdavic-Nikolaidis[1,2], *M. M. Jevremovic*[3], *M. C. Allison*[1], *D. R. Stanisavljev*[2], *G. A. Bowmaker*[1], *Z. D. Zujovic*[1,4,5*]

[1]School of Chemical Sciences, The University of Auckland, Private Bag 92019, 1142 Auckland, New Zealand
[2]Faculty of Physical Chemistry, Studentski Trg 12-16, 11001 Belgrade, Serbia
[3]Nuclear Facilities of Serbia, 12–14 Mike Petrovica Alasa, Vinca, 11351 Belgrade, Serbia
[4]Institute of General and Physical Chemistry, Studentski Trg 12–16, 11001 Belgrade, Serbia
[5]MacDiarmid Institute for Advanced Materials and Nanotechnology, Victoria University of Wellington, 6140 Wellington, New Zealand

Received 9 April 2014; accepted in revised form 26 May 2014

Abstract. For the first time, microwave assisted aniline oxidative polymerization is performed in the presence of acetic acid (CH_3COOH) and ammonium hydroxide (NH_4OH) at different microwave power levels. The reaction system is kept at constant temperature of 24±1°C. The products are investigated by Fourier Transform Infrared Spectroscopy (FTIR), Raman, solid-state Nuclear Magnetic Resonance (NMR) and Electron Paramagnetic Resonance (EPR) spectroscopies. EPR signals in polyaniline (PANI) originate from the polarons formed upon protonation and doping by acid. The microwave radiation causes an increase in the spin concentration which is slightly more evident for 8 W than for 93 W. The morphology is investigated by using scanning electron microscopy (SEM). SEM micrographs revealed the formation of nanorods (in the presence of CH_3COOH) and nanospheres (in the presence of NH_4OH). FTIR, Raman and solid-state NMR spectroscopies indicate the presence of PANI and aniline oligomers. X-ray Diffraction (XRD) measurements showed the presence of well-ordered structures.

Keywords: *polymer synthesis, molecular engineering, microwave-enhanced, self-assembly, polyaniline, nanomaterials*

1. Introduction

Polyaniline (PANI) has been one of the most studied electrically conducting polymers. This is mainly because of its simple doping-dedoping REDOX chemistry, ease of synthesis, relatively inexpensive production and ability to yield nanostructured materials of different morphologies. There are different means for obtaining PANI including a chemical, an electrochemical and recently introduced a microwave (MW) assisted methodology [1–3].

Over the last decade the chemical approach i.e. the oxidative polymerization of aniline has been used for the synthesis of wide variety of products with different morphologies and physical and chemical properties [4–14]. The specific characteristics make PANIs applicable in various fields such as gas sensors, biosensors, actuators, anticorrosive coatings, electronic devices etc. [1, 2]. Some of syntheses have been performed at medium or high pH (pH > 4) compared to standard, relatively low pH conditions (pH < 2.5) [15, 16]. The standard low pH synthesis in an acidic medium using 1 M HCl for instance yields morphologically featureless and highly conductive PANIs. On the other hand it has been shown that higher pH values very often favour self-assembly of well-defined, but less conductive supramolecular

*Corresponding author, e-mail: z.zujovic@auckland.ac.nz

structures: nanotubes, nanospheres, nanorods, nanodisks etc. [17–21]. These can be used directly as formed or indirectly as templates for other PANI based materials which exhibit better conductivity and an improved environmental stability [17]. Therefore, the ever growing need for various applications demands further developments in the field of self-assembly of nanomaterials obtained in the oxidative polymerization of aniline.

A novel method of synthesis of PANI using a microwave assisted approach under controlled temperature (Enhanced Microwave Synthesis – EMS) [22–26] has been recently introduced [3, 27]. The reaction vessel is externally cooled while simultaneously irradiated with microwaves. Temperature in the system was measured by a fiber optic temperature sensor preventing interaction with MWs and influence on the temperature reading. This is significantly different from the conventional microwave synthesis (CMS) [28, 29] which mainly relies on thermal heating and where the system due to the efficient heating quickly reaches a high temperature. When the reaction system attains the predetermined bulk temperature, the microwave irradiation is turned off ensuring that reagents and products are not degraded by excessive heating. This approach cannot preserve constant temperature of the samples during extended time intervals. In the EMS synthesis a source of microwave heating is finely balanced with external cooling system so that samples may be permanently irradiated keeping the reaction solution at certain bulk temperature. This enables a continuous flow of MW energy into the system which maintains a desired temperature [22, 30–32].

However, the development of materials with specific physicochemical and morphological characteristics tailored to certain applications is constrained by the absence of a theoretical framework relating product characteristics to MW operation. The question whether all effects can be attributed to thermal or to specific thermal and non-thermal effects related to microwave radiation should be answered and taken into account during EMS synthesis. This has sparked a sharp debate that divides the scientific community [33, 34]. The non-thermal effects are a result of the direct interactions of molecules with electromagnetic irradiation which could change kinetic parameters of the reactions. The specific thermal effects include superheating phenomena, different distribution of heat compared with classical heating and different heating of phases present in the same system producing 'hot spots'. In order to explain the formation mechanism of nanostructured PANIs in MW, we hypothesized that two reaction stages existed, both affected by microwave irradiation: (a) nucleation and (b) chain growth (polymerization) [35]. The first stage is based on instantaneous local heating that develops conditions for homogeneous nucleation. Other effects such as diffusion or molecular agitation could drive the second stage that is also fast. However, the lack of a full understanding as to what mechanisms drive MW effects and the formation of specific PANIs make further studies based on our preliminary data necessary.

Using the EMS approach is important as PANI exhibits better physicochemical characteristics when synthesized at lower temperatures [36, 37]. Besides this, PANI materials have been synthesised on a large scale using the EMS scheme [3, 27]. Also, it has been shown that the EMS yields specific nanostructured materials which open possibilities for upscaled production of polymeric conducting nanostructures [3, 35]. At the same time, various parameters such as a MW power, reaction time, concentrations of reagents, pH etc. can be used to tune various chemical and physical properties of PANI such as molecular weight, morphology, conductivity etc. [35].

We have previously reported studies of the self-assembly of various nanostructures synthesized at relatively low temperatures and at initial medium pH based on a conventional aniline oxidative polymerization approach [18–21, 38–41]. However, using microwave synthesis at low pH PANI was produced in 5 minutes with 80% yield (synthesized sixty times faster compared to the classical chemical synthesis). Typically, self-assembly favours low temperatures, low concentrations of reactants and long reaction times. The question is whether we can use the EMS for self-assembly knowing that MW accelerates reactions.

Therefore, the idea here is to use the advantages of constant microwave irradiation during the self-assembly process while keeping the reaction temperature low. Is it possible to get nanostructures at initially high and medium pH using the microwave method, which usually promotes fast syntheses? Will microwaves affect the final products? To gain insight into these matters, a microwave-enhanced

aniline oxidative polymerization at initial medium and high pH was carried out.

2. Experimental methods

2.1. Synthesis

PANI was prepared by aniline oxidation with ammonium persulfate (APS). APS (1.3704 g) was added to an aqueous solution of 0.4 M acetic acid (CH_3COOH) or 0.2 M ammonium hydroxide, NH_4OH (12 mL), followed by addition of 0.4369 mL of aniline. The initial pH values were around 5 and 10 for the CH_3COOH and NH_4OH mediums, respectively. Information on chemicals: 1) Aniline, ACS reagent, ≥99.5%, Sigma Aldrich, CAS Number 62-53-3;2) Ammonium persulphate, reagent grade 98%, Sigma Aldrich, CAS Number 7727-54-0;3) Ammonium hydroxide, ACS reagent, 28.0–30.0% NH_3 basis, Sigma Aldrich, CAS Number 1336-21-6; 4) Acetic acid, Acetic acid – Glacial acetic acid, 99.7+%, ACS reagent, Acros Organic, CAS Number 64-19-7. The MW PANI synthesis using CH_3COOH and NH_4OH was performed at three power levels, 0, 8 and 93 W for 10 and 20 min. The synthesis performed at 0 W is equivalent to a classical chemical synthesis (CS). The reaction mixture was filtered and washed thoroughly with distilled water. The retentates were dried in a vacuum oven at 40°C overnight.

2.2. Microwave apparatus

MW irradiation was performed in a single mode focused CEM reactor (Model Discover, CEM Co., Matthew, NC) operating at 2.45 GHz with ability to control the output power. The experimental parameters were set up as previously described [38, 40]. An external cooling circuit maintained constant temperature of the reaction mixture and constant irradiation power. In order to maintain uniform temperature the sample was mixed by magnetic stirring at 400 rpm. The PANI MW synthesis using APS was performed at microwave power 0, 8 and 93 W. All experiments were done under the same conditions by keeping constant irradiation power, temperature and initial reaction mixture volume. The temperature was maintained at 24±1°C in all experiments.

2.3. FTIR spectroscopy

Fourier transform infrared (FTIR) spectra were recorded with resolution 2 cm^{-1} using a Nicolet 8700 FT-IR spectrometer with KBr pellets. 100 scans were averaged for each sample.

2.4. Raman spectroscopy

Raman spectra were recorded at 1 cm^{-1} resolution using a Renishaw Raman System-Model 1000 spectrometer with 785 nm (red) laser excitation.

2.5. SEM

SEM was carried out using a Philips XL30S Field Emission Gun with a SiLi (Lithium drifted) EDS detector with Super Ultra Thin Window. The PANI samples were 10 mm in diameter, mounted on aluminium studs using adhesive graphite tape and sputter coated using a Polaron SC7640 Sputter Coater at 5–10 mA and 1.1 kV for 5 min.

2.6. Solid-state NMR spectroscopy

Solid-state NMR experiments were carried out on dry powder samples using a Bruker AVANCE 300 standard bore magnet system operating at 300.13 MHz proton frequency (7.05 T). Spectra were obtained by using CP MAS (Cross-Polarization Magic Angle Spinning) technique. The experiments were carried out using a Bruker double resonance broadband probe with zirconium oxide (ZrO_2) 7 mm rotors and Kel-F caps. The magic angle was adjusted by maximizing the sidebands of the ^{79}Br signal of a KBr sample. The typical parameters for ^{13}C NMR spectroscopy were: a 90° pulse width of 4.2 μs, a spin-lock field of 62.5 kHz, contact time of 1.5 ms, a recycle delay of 1 s and a spectral-width of 40 kHz. Experiments were carried out with 5000 scans at ambient temperature using samples enclosed in the rotors. The ^{13}C chemical shift scale was referenced to tetramethylsilane (TMS). Samples were rotated at 7000±1 Hz.

2.7. Electron paramagnetic resonance (EPR) spectroscopy

EPR spectra of 7.9 mg for the standard sample and 10.5 mg for MW PANI samples in quartz EPR tubes, were recorded at ambient temperature using a JEOL JES-FA 200 EPR spectrometer with modulation amplitude 16 mT. The spin concentration was determined using hydrated copper sulphate ($CuSO_4$) as a standard. The EPR spectra of the samples and $CuSO_4 \cdot 5H_2O$ were recorded under the same conditions. The spin concentration, N_{sample} (spins g^{-1}) was calculated using the area calculated from the second integral of the first-derivative signals using Matlab according to Equation (1):

$$N_{sample} = \frac{Area_{sample}}{Area_{reference}} \cdot \frac{mass_{reference}}{mass_{sample}} N_{reference} \quad (1)$$

where the reference substance used was $CuSO_4 \cdot 5H_2O$, for which $N_{reference} = 2.412 \cdot 10^{21}$ spins g^{-1}.

2.8. X-ray diffraction (XRD) measurements

To determine the changes in crystallinity and structure of the samples X-ray Diffraction (XRD) measurements were recorded at room temperature on a Panalytical Empyreon powder diffractometer with Cu Kα radiation (40 kV, 40 mA) in transmission mode. Diffraction intensities were measured with a PixCel solid state detector by scanning from 6 to 50° (2θ) with a step size of 0.02° (2θ) at 0.25 sec/step.

3. Results and discussion

3.1. SEM measurements

SEM micrographs of the samples obtained using the EMS at different power levels using CH_3COOH and NH_4OH are shown in Figure 1. The micrographs obtained from the samples synthesized with CH_3COOH at 8 W mainly show elongated, tape-like structures. The product obtained after 20 min looks morphologically more homogeneous compared to the 10 min product, showing the presence of nanorods. The morphology of the samples synthesized with CH_3COOH depends on the microwave power level, as can be seen from the micrographs of the samples synthesized at 8 and 93 W (10 min). The product obtained at 93 W is more morphologically heterogeneous, although it does consist of elongated nanostructures. At the same time the sample synthesized 0 W is mainly featureless and microporous.

Samples synthesized with NH_4OH show different dependence on the microwave power and the reaction time. First, the main products are nanospheres. The samples synthesized at 93 W are morphologically more uniform compared to the sample obtained at 8 W. Also, it seems that in this case the shorter reaction times favor better defined nanostructures.

Overall, the samples synthesized under medium to high pH conditions exhibit compact and defined nanostructural morphologies. They show differences when obtained on different MW powers and reaction times. The morphologies obtained here are similar to those obtained using a standard approach [15]. However, microwave actuation allows for faster reactions and possibilities for fine tuning of aniline oxidative polymerization [3, 27]. Due to their distinctive morphological characteristics, samples synthesized after a reaction time of 10 min for CH_3COOH and 20 min for NH_4OH were chosen for structural analysis.

3.2. FTIR and aman spectroscopy

3.2.1. FTIR spectroscopy

FTIR spectra of the PANI samples obtained with CH_3COOH and NH_4OH are shown in Figure 2. The values in the brackets represent the peak positions in the FTIR spectrum from the sample obtained in the presence of NH_4OH. There is a shoulder at 1641 (1640) cm^{-1} which can be assigned to a to a hydrogen-bonded C=O stretch, i.e., –C=O••••H–N– [5]. The intense bands and shoulders at 1591 (1598) cm^{-1} and the bands at 1504 (1511) cm^{-1} are present in all

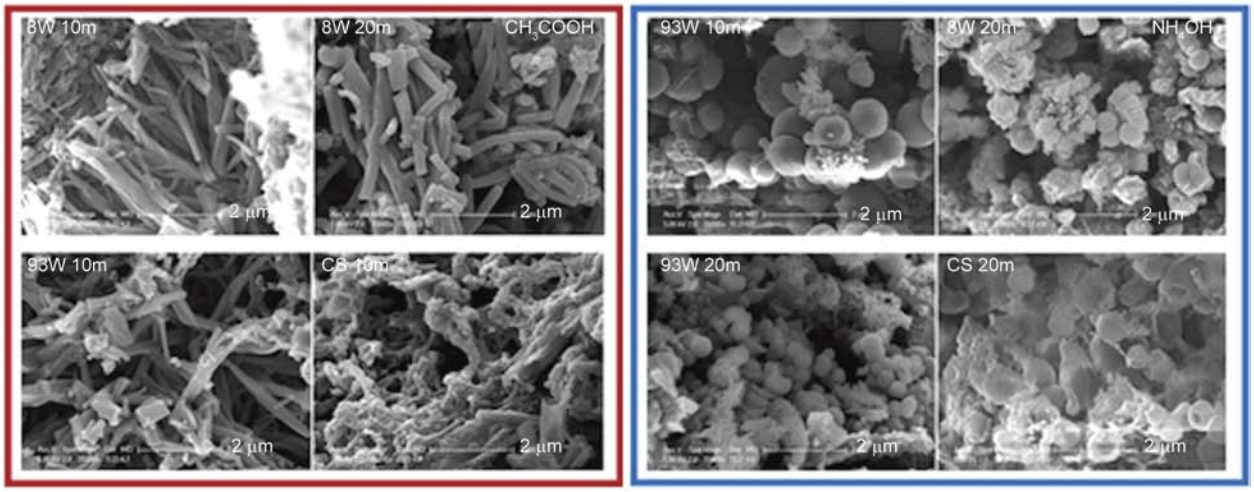

Figure 1. SEM micrographs of the products obtained with CH_3COOH (red) and NH_4OH (blue) at different reaction times and power levels (CS = 0 W).

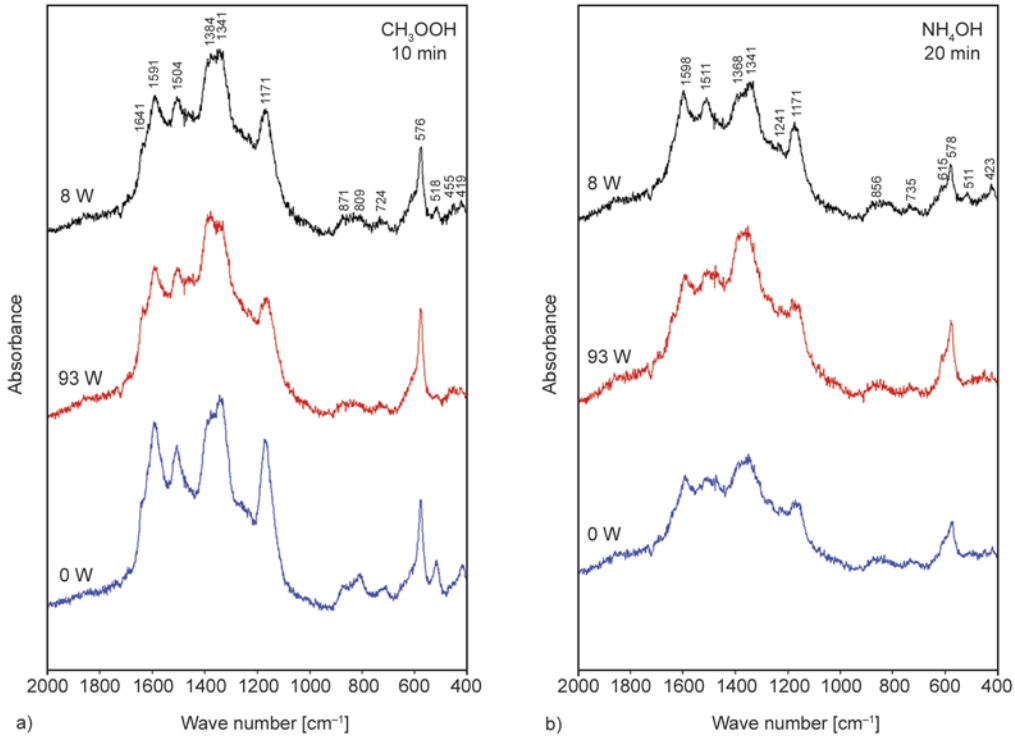

Figure 2. FTIR spectra of the products obtained with CH_3COOH (10 min) (a) and NH_4OH (20 min) (b) at different microwave powers

spectra (Figure 1) and can be attributed to C=C stretching in the quinoid and benzenoid rings, respectively [42]. The band at about 1364 (1368) cm^{-1} is attributed to C–N stretching [43] or C–C stretch in quinoid segments [42]. The peak at 1341 (1341) cm^{-1} can be assigned to C–N stretching (plus C–C stretching) [43] or C–H bending in benzenoid units [42]. The band at 1170 (1171) cm^{-1} can be due to C–H bending in benzenoid structures or it has been often referred as an electronic band [43, 44]. This peak is significantly more intense compared to the corresponding peaks from the samples obtained in the EMS syntheses implying the higher degree of delocalization of electrons [44] in these samples. The band at 871 (856) cm^{-1} is due to C–H out-of-plane bending on three substituted benzene ring [43]. The band at 809 cm^{-1} can be assigned to out-of-plan C–H bending in the benzenoid units [45]. The band at 724 (735) cm^{-1} can be assigned to C–N=C bending [42], or C–H out-of-plane bending on disubtituted benzene ring [43]. The bands from ca. 500 to 600 cm^{-1} are due to aromatic ring deformations in the benzenoid and quinoid units [42, 43]. The band at 419 (423) cm^{-1} is due ring deformation out-of-plane of the benzenoid ring.

3.2.2. Raman spectroscopy

Raman spectra of the samples obtained by MW after 10 and 20 minutes at 93 and 8 W with CH_3COOH and NH_4OH and for the conventional synthesis are shown in Figure 3 (left and right). The bands at 1589 (1589) cm^{-1} can be assigned to C=C stretch in quinoid units [42]. The bands 1511 (1489) cm^{-1} are characteristic for C=N stretching and C–H bending in benzenoid units [42]. The bands 1368 (1367) cm^{-1} can be assigned to C–C stretching in quinoid units. The band at 1341 cm^{-1} is assigned to C–H bending in benzenoid units [42] while the band at 1231 cm^{-1} (NH_4OH spectra) belongs to $C–N^+$ + C–C stretching [43]. The bands at 1171 (1168) cm^{-1}, 856 (856) cm^{-1} and 735 (730) cm^{-1} are attributed to C–H bending of the quinoid rings, ring deformations in benzenoid and ring deformations in quinoid units, respectively [42]. The band at 578 (578) cm^{-1} is due to a quinoid ring deformation [42].

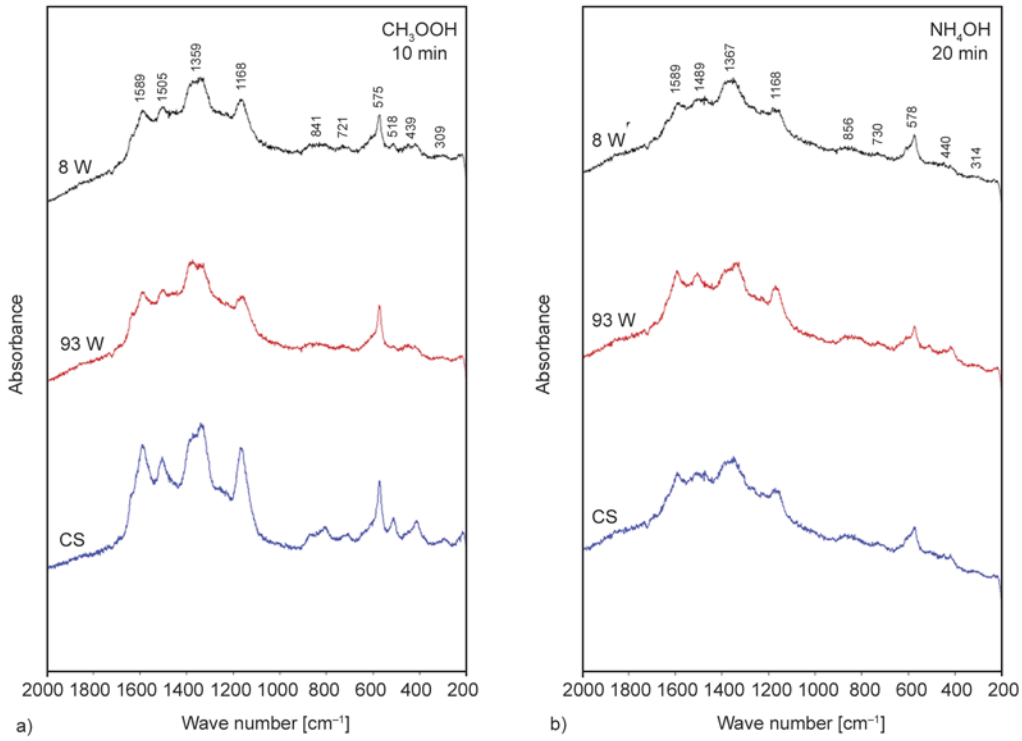

Figure 3. Raman spectra of the products obtained with CH_3COOH (10 min) (a) and NH_4OH (20 min) (b) at different microwave powers

The FTIR and Raman spectra reveal the presence of quinoid/benzenoid segments in all samples either synthesized conventionally or in the microwave.

3.3. Solid-state NMR spectroscopy

The solid-state ^{13}C CPMAS NMR spectra of aniline oxidation products obtained with CH_3COOH and NH_4OH after 10 and 20 min reaction time at different MW power levels are shown in Figure 4.

The assignment of peaks in the ^{13}C CPMAS spectra shown in Figure 4 is based on data obtained from chemically synthesized PANI [46, 47] (Figure 5α) and from the products synthesized using the 'pH falling' approach (Figure 5β) [20, 40]. The peak at ca. 180 ppm (see Figure 4) is usually not seen in the NMR spectra of chemically synthesized PANI.

The 181.5 ppm signal could be due to the presence of carbonyl groups on the six-membered rings (C-9,

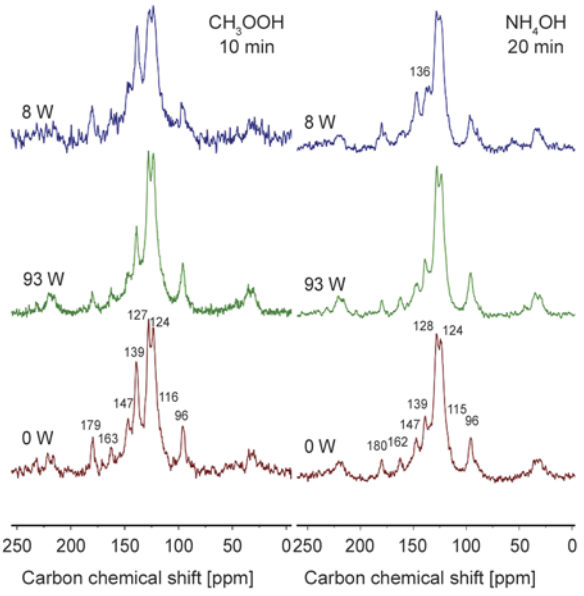

Figure 4. Solid-state NMR spectra of the products obtained with CH_3COOH (10 min) and NH_4OH (20 min) at different microwave powers

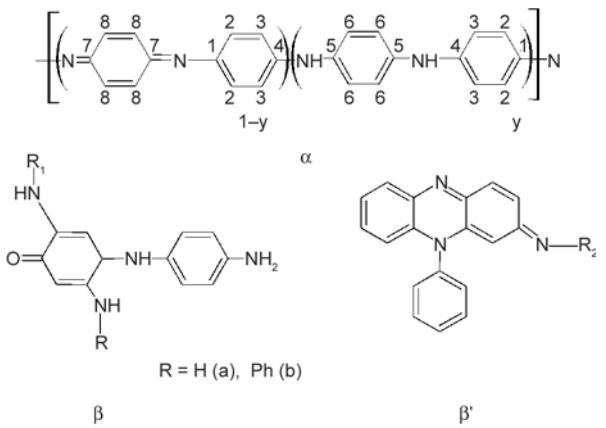

Figure 5. Proposed structural units present in the nanostructured aniline oxidation products obtained at different power levels

Figure 5β), as proposed previously in studies of the products obtained in the oxidative polymerization of aniline [5, 40]. The peaks at ca. 163 ppm are assigned to non-protonated imine quinoid carbon (C-7, see Figure 5α) [48]. The peaks at ca. 147 ppm are assigned to nonprotonated carbon attached to the imine nitrogen C-1 [40]. This confirms the presence of quinoid rings. The peak at ≈140 ppm due to nonprotonated carbons (C-4 and C-5) [40] could be partly overlapped with the peak for protonated quinoid carbon (≈139 ppm for 'standard' chemically synthesized PANI [46]). The peaks at ca. 124 ppm are assigned to protonated benzenoid carbon (C-2,3). The resonance at 128 ppm could be attributed to protonated quinoid carbons C-8 [49]. This peak was also partly attributed to the presence of bipolarons i.e. positively charged domains [50]. The peak at 96 ppm found in all spectra (Figure 4) is usually not characteristic for chemically synthesized PANI and it can be due to the presence of branching in the polymer structure (C-10, Figure 5β) [20]. The spectral features i.e. the differences in the relative peak intensities in the NMR spectra imply the presence of a mixture of aniline oligomeric structures with the presence of quinoid and benzenoid, i.e. PANI segments. These polymerize at a late stage of synthesis.

3.4. EPR spectroscopy

The EPR spectra of the products obtained at different microwave power levels in the presence of CH_3COOH and NH_4OH are shown in Figures 6 and 7 respectively. The spin concentrations calculated from the second integrals using Equation (1) are given in Table 1. For both reaction media the use of microwave radiation results in an increase in the spin concentration, which is slightly greater for 8 W than for 93 W irradiation power level. Microwave irradiation also causes a slight increase in the EPR linewidth; in the case of the reaction in CH_3COOH, this results in the EPR signals for the MW synthesized products obtained at 8 and 93 W having lower peak intensities than that for the 0 W product (Figure 6), despite the fact that the latter has the lowest spin concentration (Table 1). In the case of reaction in NH_4OH, the spin concentration for the 0 W product is much lower, so that the order of the EPR peak intensities (Figure 7) is the same as that of the spin concentrations (Table 1), although here again the line-broadening effect of MW irradiation in the synthesis is evident in the considerably lower peak intensity of the signal for the 93 W relative to the 8 W sample (Figure 7). EPR signals in PANI are due to the formation of polarons upon protonation and doping of the PANI by acid [51] and this is presumably the cause of the signals observed in the present study, the dopant acid being H_2SO_4 produced by reduction of APS in the oxidation of aniline.

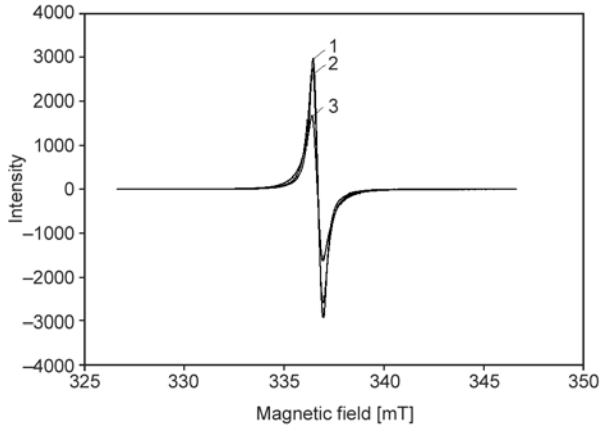

Figure 6. EPR spectra of the samples prepared with CH_3COOH and taken after 10 min 1) 0 W; 2) 93 W and 3) 8 W

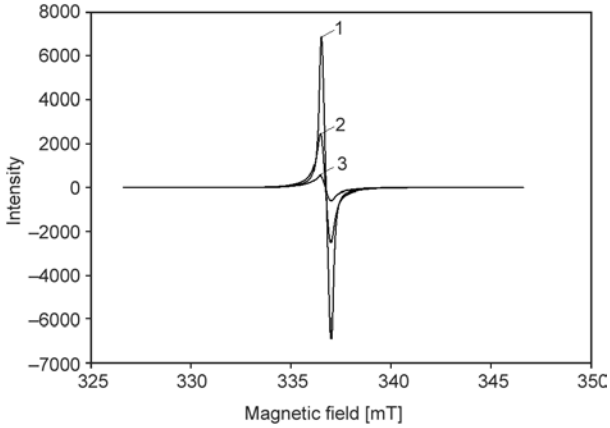

Figure 7. EPR spectra of the samples prepared with NH_4OH and taken after 20 min: 1) 8 W; 2) 93 W and 3) 0 W

Table 1. Spin concentration N_{sample} for the synthesized PANIs

Sample	Spin concentration N_{sample} (spin g^{-1})·10^{19}
CH_3COOH 8 W 10 min	2.333
CH_3COOH 93 W 10 min	2.216
CH_3COOH 0 W 10 min	1.840
NH_4OH 8 W 20 min	2.278
NH_4OH 93 W 20 min	2.105
NH_4OH 0 W 20 min	0.758

3.5. XRD measurements

To investigate structural characteristics of the samples obtained powder XRD measurements were carried out. XRD patterns of the samples obtained with CH_3COOH exhibit sharp lines in the region of $5° < 2\theta < 50°$ (Figure 8a). This implies long-range ordering in this sample. The main diffraction peaks are at 2θ values of 6.5, 16.2, 17.9, 19.1, 23.3, 23.6, 26.2, 26.5, 27.0, 30.3 and less intensive peaks at 32.8, 33.4, 36.6, 36.2, 38.5, 40.4, and 40.7. The peaks at $2\theta = 6.5$ implies very long range order, which can be assigned to the periodicity caused by the aniline/dopant acid salt [52]. The peaks at 17.9 and 26.2° can be attributed to the periodicity parallel and perpendicular to the polymer chains, respectively [52–54]. The peaks at ca. 23 and also at 26° could be due to a periodicity caused by π-π stacking of rigid phenazine-like structures [53]. At the same time the sample obtained at 0 W shows broad reflection due to the presence of amorphous phases. This is very interesting as it implies that samples obtained in the presence of MWs have significantly more ordered structure.

XRD patterns of the samples obtained with NH_4OH in the presence of MWs also show sharp lines (Figure 8b), except for the 10 min sample obtained at 93 W. The position of sharp peaks is close to those shown in Figure 8a and the same assignment can apply. XRD patterns of the samples obtained at 0 W show mixed crystallinity. That is, 10 min sample shows broad peaks, while the 20 min sample exhibit very sharp peaks. This could imply that in the first 10 min regardless of microwave power an amorphous phase is formed, and then with time progressing more crystalline structures are obtained. These findings can be very interesting as MW can be used for the formation of very well ordered structures.

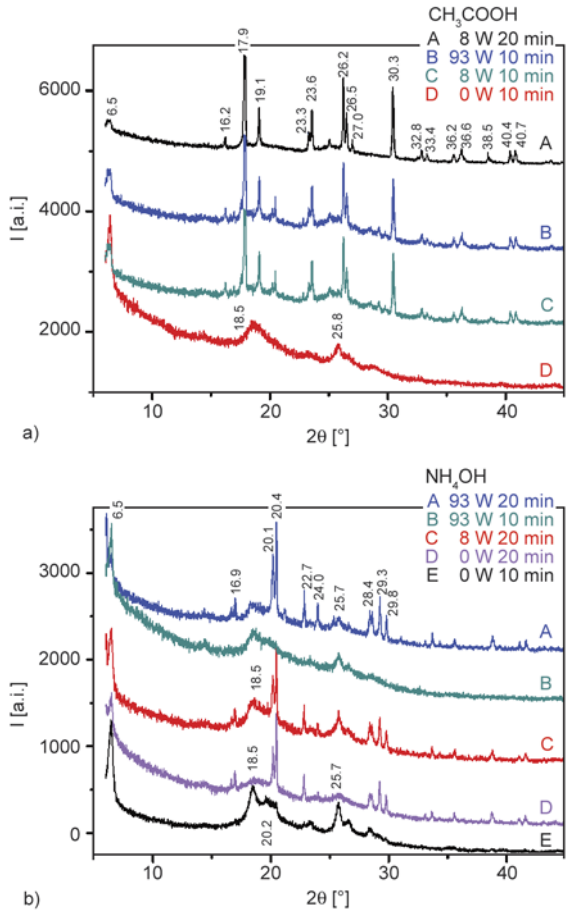

Figure 8. XRD patterns of the samples prepared with CH_3COOH (a) and NH_4OH (b) collected at different power levels and reaction times

4. Conclusions

MW assisted aniline oxidative polymerization syntheses under medium and high pH are performed for the first time. SEM micrographs showed that products obtained after 10 and 20 min consist of either nanorods (in the presence of CH_3COOH) or nanospheres (in the presence of NH_4OH). Based on solid-state NMR, FTIR and Raman data it was shown that branched structures with the existence of the benzenoid/quinoid segments prevail in the final products. This is not surprising considering that the syntheses started at medium and high pH. An increase in the spin concentration is slightly more evident for 8 W than for 93 W power level, according to EPR spectroscopy. XRD data suggest the presence of well-ordered (crystal-like) structures.

Here, it is worth highlighting the fact that the MW approach can be used for the formation of self-assembled nanorods and nanospheres. This is interesting as it is well known that self-assembly favors longer reaction times for complex, supramolecular structures to be formed. Self-assembly of aniline based products (polyanilines or oligoanilines) is quite complicated subject especially in the presence of microwaves. Additional work is needed to understand the complex formation mechanisms in the microwave-assisted polymerization.

Acknowledgements

The authors acknowledge financial support Ministry of Science and Environmental Protection of Serbia (Contract No. 172015) and PBRF Fund School of Chemical Sciences, the University of Auckland. The authors would like to thank Dr Michel Nieuwoudt for her asistence with FTIR, Raman and EPR spectroscopies.

References

[1] Wallace G. G., Spinks G. M., Kane-Maguire L. A. P.: Conductive electroactive polymers: Intelligent materials systems. CRC Press, Boca Raton (2002).

[2] Skotheim T. A., Reynolds J. R.: Handbook of conducting polymers, conjugated polymers processing and applications. CRC Press, Boca Raton (2007).

[3] Gizdavic-Nikolaidis M. R., Stanisavljev D. R., Easteal A. J., Zujovic Z. D.: A rapid and facile synthesis of nanofibrillar polyaniline using microwave radiation. Macromolecular Rapid Communications, **31**, 657–661 (2010).
DOI: 10.1002/marc.200900800

[4] Huang J., Kaner R. B.: A general chemical route to polyaniline nanofibers. Journal of the American Chemical Society, **126**, 851–855 (2004).
DOI: 10.1021/ja0371754

[5] Venancio E. C., Wang P-C., MacDiarmid A. G.: The azanes: A class of material incorporating nano/micro self-assembled hollow spheres obtained by aqueous oxidative polymerization of aniline. Synthetic Metals, **156**, 357–369 (2006).
DOI: 10.1016/j.synthmet.2005.08.035

[6] Wei Z., Zhang Z., Wan M.: Formation mechanism of self-assembled polyaniline micro/nanotubes. Langmuir, **18**, 917–921 (2002).
DOI: 10.1021/la0155799

[7] Zhang L., Wan M.: Self-assembly of polyaniline – From nanotubes to hollow microspheres. Advanced Functional Materials, **13**, 815–820 (2003).
DOI: 10.1002/adfm.200304458

[8] Zhang Z., Wan M., Wei Y.: Highly crystalline polyaniline nanostructures doped with dicarboxylic acids. Advanced Functional Materials, **16**, 1100–1104 (2006).
DOI: 10.1002/adfm.200500636

[9] Ćirić-Marjanović G.: Polyaniline nanostructures. in 'Nanostructured conductive polymers' (ed.: Eftekhari A.) Wiley, London, 19–98 (2010).

[10] Ćirić-Marjanović G., Dondur V., Milojević M., Mojović M., Mentus S., Radulović A., Vuković Z., Stejskal J.: Synthesis and characterization of conducting self-assembled polyaniline nanotubes/zeolite nanocomposite. Langmuir, **25**, 3122–3131 (2009).
DOI: 10.1021/la8030396

[11] Ćirić-Marjanović G., Trchová M., Stejskal J.: The chemical oxidative polymerization of aniline in water: Raman spectroscopy. Journal of Raman Spectroscopy, **39**, 1375–1387 (2008).
DOI: 10.1002/jrs.2007

[12] Konyushenko E. N., Stejskal J., Šeděnková I., Trchová M., Sapurina I., Cieslar M., Prokeš J.: Polyaniline nanotubes: Conditions of formation. Polymer International, **55**, 31–39 (2006).
DOI: 10.1002/pi.1899

[13] Stejskal J., Sapurina I., Trchová M., Konyushenko E. N., Holler P.: The genesis of polyaniline nanotubes. Polymer, **47**, 8253–8262 (2006).
DOI: 10.1016/j.polymer.2006.10.007

[14] Stejskal J., Spirkova M., Riede A., Helmstedt M., Mokreva P., Prokes J.: Polyaniline dispersions 8. The control of particle morphology. Polymer, **40**, 2487–2492 (1999).
DOI: 10.1016/S0032-3861(98)00478-9

[15] Konyushenko E. N., Trchová M., Stejskal J., Sapurina I.: The role of acidity profile in the nanotubular growth of polyaniline. Chemical Papers, **64**, 56–64 (2010).
DOI: 10.2478/s11696-009-0101-z

[16] Ćirić-Marjanović G., Konyushenko E. N., Trchová M., Stejskal J.: Chemical oxidative polymerization of anilinium sulfate versus aniline: Theory and experiment. Synthetic Metals, **158**, 200–211 (2008).
DOI: 10.1016/j.synthmet.2008.01.005

[17] Tran H. D., D'Arcy J. M., Wang Y., Beltramo P. J., Strong V. A., Kaner R. B.: The oxidation of aniline to produce 'polyaniline': a process yielding many different nanoscale structures. Journal of Materials Chemistry, **21**, 3534–3550 (2011).
DOI: 10.1039/c0jm02699a

[18] Laslau C., Zujovic Z., Travas-Sejdic J.: Theories of polyaniline nanostructure self-assembly: Towards an expanded, comprehensive multi-layer theory (MLT). Progress in Polymer Science, **35**, 1403–1419 (2010).
DOI: 10.1016/j.progpolymsci.2010.08.002

[19] Laslau C., Zujovic Z. D., Zhang L., Bowmaker G. A., Travas-Sejdic J.: Morphological evolution of self-assembled polyaniline nanostuctures obtained by pH-stat chemical oxidation. Chemistry of Materials, **21**, 954–962 (2009).
DOI: 10.1021/cm803447a

[20] Zujovic Z. D., Laslau C., Bowmaker G. A., Kilmartin P. A., Webber A. L., Brown S. P., Travas-Sejdic J.: Role of aniline oligomeric nanosheets in the formation of polyaniline nanotubes. Macromolecules, **43**, 662–670 (2010).
DOI: 10.1021/ma902109r

[21] Zujovic Z. D., Laslau C., Travas-Sejdic J.: Lamellar-structured nanoflakes comprised of stacked oligoaniline nanosheets. Chemistry – An Asian Journal, **6**, 791–796 (2011).
DOI: 10.1002/asia.201000703

[22] Gerbec J. A., Magana D., Washington A., Strouse G. F.: Microwave-enhanced reaction rates for nanoparticle synthesis. Journal of the American Chemical Society, **127**, 15791–15800 (2005).
DOI: 10.1021/ja052463g

[23] Seijas J. A., Vázquez-Tato M. P., Martínez M. M., Rodríguez-Parga J.: Microwave enhanced synthesis of acridines. A new aspect in the Bernthsen reaction. Green Chemistry, **4**, 390–391 (2002).
DOI: 10.1039/B204243F

[24] Ayele D. W., Chen H-M., Su W-N., Pan C-J., Chen L-Y., Chou H-L., Cheng J-H., Hwang B-J., Lee J-F.: Controlled synthesis of CdSe quantum dots by a microwave-enhanced process: A green approach for mass production. Chemistry – A European Journal, **17**, 5737–5744 (2011).
DOI: 10.1002/chem.201003686

[25] Wu C-C., Shiau C-Y., Ayele D. W., Su W-N., Cheng M-Y., Chiu C-Y., Hwang B-J.: Rapid microwave-enhanced solvothermal process for synthesis of $CuInSe_2$ particles and its morphologic manipulation. Chemistry of Materials, **22**, 4185–4190 (2010).
DOI: 10.1021/cm1006263

[26] Lange J. H. M., Verveer P. C., Osnabrug S. J. M., Visser G. M.: Rapid microwave-enhanced synthesis of 4-hydroxyquinolinones under solvent-free conditions. Tetrahedron Letters, **42**, 1367–1369 (2001).
DOI: 10.1016/s0040-4039(00)02244-9

[27] Gizdavic-Nikolaidis M. R., Stanisavljev D. R., Easteal A. J., Zujovic Z. D.: Microwave-assisted synthesis of functionalized polyaniline nanostructures with advanced antioxidant properties. The Journal of Physical Chemistry C, **114**, 18790–18796 (2010).
DOI: 10.1021/jp106213m

[28] Kappe C. O., Dallinger D., Murphree S. S.: Practical microwave synthesis for organic chemists: Strategies, instruments, and protocols. Wiley-VHC, Weinheim (2009).

[29] Kappe C. O., Stadler A.: Microwaves in organic and medicinal chemistry. Wiley-VHC, Weinheim (2005).

[30] Antonio C., Deam R. T.: Can 'microwave effects' be explained by enhanced diffusion? Physical Chemistry Chemical Physics, **9**, 2976–2982 (2007).
DOI: 10.1039/B617358F

[31] de la Hoz A., Dyaz-Ortiz A., Moreno A.: Microwaves in organic synthesis. Thermal and non-thermal microwave effects. Chemical Society Reviews, **34**, 164–178 (2005).
DOI: 10.1039/B411438H

[32] Perreux L., Loupy A.: A tentative rationalization of microwave effects in organic synthesis according to the reaction medium, and mechanistic considerations. Tetrahedron, **57**, 9199–9223 (2001).
DOI: 10.1016/S0040-4020(01)00905-X

[33] Kappe C. O., Pieber B., Dallinger D.: Microwave effects in organic synthesis: Myth or reality? Angewandte Chemie International Edition, **52**, 1088–1094 (2013).
DOI: 10.1002/anie.201204103

[34] Dudley G. B., Stiegman A. E., Rosana M. R.: Correspondence on microwave effects in organic synthesis. Angewandte Chemie International Edition, **52**, 7918–7923 (2013).
DOI: 10.1002/anie.201301539

[35] Gizdavic-Nikolaidis M. R., Jevremovic M., Stanisavljev D. R., Zujovic Z. D.: Enhanced microwave synthesis: Fine-tuning of polyaniline polymerization. The Journal of Physical Chemistry C, **116**, 3235–3241 (2012).
DOI: 10.1021/jp2086939

[36] Adams P. N., Laughlin P. J., Monkman A. P., Kenwright A. M.: Low temperature synthesis of high molecular weight polyaniline. Polymer, **37**, 3411–3417 (1996).
DOI: 10.1016/0032-3861(96)88489-8

[37] Stejskal J., Riede A., Hlavatá D., Prokeš J., Helmstedt M., Holler P.: The effect of polymerization temperature on molecular weight, crystallinity, and electrical conductivity of polyaniline. Synthetic Metals, **96**, 55–61 (1998).
DOI: 10.1016/s0379-6779(98)00064-2

[38] Zhang L., Peng H., Zujovic Z. D., Kilmartin P. A., Travas-Sejdic J.: Characterization of polyaniline nanotubes formed in the presence of amino acids. Macromolecular Chemistry and Physics, **208**, 1210–1217 (2007).
DOI: 10.1002/macp.200700013

[39] Zhang L., Zujovic Z. D., Peng H., Bowmaker G. A., Kilmartin P. A., Travas-Sejdic J.: Structural characteristics of polyaniline nanotubes synthesized from different buffer solutions. Macromolecules, **41**, 8877–8884 (2008).
DOI: 10.1021/ma801728j

[40] Zujovic Z. D., Zhang L., Bowmaker G. A., Kilmartin P. A., Travas-Sejdic J.: Self-assembled, nanostructured aniline oxidation products: A structural investigation. Macromolecules, **41**, 3125–3135 (2008).
DOI: 10.1021/ma071650r

[41] Laslau C., Zujovic Z. D., Travas-Sejdic J.: Polyaniline 'nanotube' self-assembly: The stage of granular agglomeration on nanorod templates. Macromolecular Rapid Communications, **30**, 1663–1668 (2009).
DOI: 10.1002/marc.200900244

[42] Boyer M-I., Quillard S., Rebourt E., Louarn G., Buisson J. P., Monkman A., Lefrant S.: Vibrational analysis of polyaniline: A model compound approach. The Journal of Physical Chemistry B, **102**, 7382–7392 (1998).
DOI: 10.1021/jp972652o

[43] Tang J., Jing X., Wang B., Wang F.: Infrared spectra of soluble polyaniline. Synthetic Metals, **24**, 231–238 (1988).
DOI: 10.1016/0379-6779(88)90261-5

[44] MacDiarmid A. G., Epstein A. J.: The concept of secondary doping as applied to polyaniline. Synthetic Metals, **65**, 103–116 (1994).
DOI: 10.1016/0379-6779(94)90171-6

[45] Harada I., Furukawa Y., Ueda F.: Vibrational spectra and structure of polyaniline and related compounds. Synthetic Metals, **29**, 303–312 (1989).
DOI: 10.1016/0379-6779(89)90311-1

[46] Kaplan S., Conwell E. M., Richter A. F., MacDiarmid A. G.: Solid-state carbon-13 NMR characterization of polyanilines. Journal of American Chemical Society, **110**, 7647–7651 (1988).
DOI: 10.1021/ja00231a011

[47] Kaplan S., Conwell E. M., Richter A. F., MacDiarmid A. G.: A solid-state NMR investigation of the structure and dynamics of polyanilines. Synthetic Metals, **29**, 235–242 (1989).
DOI: 10.1016/0379-6779(89)90301-9

[48] Zujovic Z. D., Nieuwoudt M., Bowmaker G. A., Kilmartin P. A.: Nanostructures obtained in the oxidative polymerization of aniline: Effects of polarons. Polymer, **54**, 6363–6372 (2013).
DOI: 10.1016/j.polymer.2013.09.020

[49] Thiyagarajan M., Kumar J., Samuelson L. A., Cholli A. L.: Enzymatically synthesized conducting polyaniline nanocomposites: A solid-state NMR study. Journal of Macromolecular Science Part A: Pure and Applied Chemistry, **40**, 1347–1355 (2003).
DOI: 10.1081/MA-120025314

[50] Kababya S., Appel M., Haba Y., Titelman G. I., Schmidt A.: Polyaniline–dodecylbenzene sulfonic acid polymerized from aqueous medium: A solid state NMR characterization. Macromolecules, **32**, 5357–5364 (1999).
DOI: 10.1021/ma982010e

[51] Kang Y., Lee H., Namgoong J., Jung B., Lee H.: Decrease in electrical conductivity upon oxygen exposure in polyanilines doped with HCl. Polymer, **40**, 2209–2213 (1999).
DOI: 10.1016/S0032-3861(98)00441-8

[52] Wang Z., Liao F., Yang S., Guo T.: A novel route synthesis of poly(ortho-phenylenediamine) fluffy microspheres self-assembled from nanospheres. Fibers and Polymers, **12**, 997–1001 (2011)
DOI: 10.1007/s12221-011-0997-0

[53] Jiang H., Sun X., Huang M., Wang Y., Li D., Dong S.: Rapid self-assembly of oligo(*o*-phenylenediamine) into one-dimensional structures through a facile reprecipitation route. Langmuir, **22**, 3358–3361 (2006).
DOI: 10.1021/la053091s

[54] Jin E., Liu N., Lu X., Zhang W.: Novel micro/nanostructures of polyaniline in the presence of different amino acids via a self-assembly process. Chemistry Letters, **36**, 1288–1289 (2007).
DOI: 10.1246/cl.2007.1288

eXPRESS Polymer Letters Vol.8, No.10 (2014) 756–766
Available online at www.expresspolymlett.com
DOI: 10.3144/expresspolymlett.2014.78

Decreased oxygen permeability of EVOH through molecular interactions

Zs. Péter[1,2], *Cs. Kenyó*[1,2], *K. Renner*[1,2*], *Ch. Kröhnke*[3], *B. Pukánszky*[1,2]

[1]Laboratory of Plastics and Rubber Technology, Department of Physical Chemistry and Material Science, Budapest University of Technology and Economics, P.O. Box 91, H-1521 Budapest, Hungary
[2]Institute of Materials and Environmental Chemistry, Research Centre for Natural Sciences, Hungarian Academy of Sciences, P.O. Box 286, H-1519 Budapest, Hungary
[3]Clariant Produkte (Deutschland) GmbH, D-81477 Munich, Germany

Received 16 March 2014; accepted in revised form 29 May 2014

Abstract. Poly(ethylene-co-vinyl alcohol) of 48 mol% ethylene content was modified with N,N′-bis(2,2,6,6-tetramethyl-4-piperidyl)-isophthalamide (Nylostab SEED) to decrease the oxygen permeability of the polymer. The additive was added in a wide concentration range from 0 to 10 wt%. The structure and properties of the polymer were characterized with various methods including differential scanning calorimetry, X-ray diffraction, mechanical testing, optical measurements and oxygen permeation. Interactions were estimated by molecular modeling and infrared spectroscopy. The results showed that oxygen permeation decreased considerably when the additive was added at less than 2.0 wt% concentration. The decrease resulted from the interaction of the hydroxyl groups of the polymer and the amide groups of the additive. The dissolution of the additive in the polymer led to decreased crystallinity, but also to decreased mobility of amorphous molecules. Stiffness and strength, but also deformability increased as a result. Above 2 wt% the additive forms a separate phase leading to the deterioration of properties. The success of the approach represents a novel way to control oxygen permeation in EVOH and in other polymers with similar functional groups capable of strong interactions.

Keywords: *material testing, oxygen permeability, crystalline structure, solubility, hydrogen bonds*

1. Introduction

The number of functional and smart packaging materials increases continuously and they are used already in everyday practice in increasing quantities [1–4]. The main functions targeted for various products are small oxygen permeability or oxygen scavenging [5–7], humidity control [8–12], regulated ethylene content [13], antimicrobial effect [14–17], adsorption of odorous materials, or the opposite, the release of desirable aromas [18, 19]. Intensive research and development work is carried out on these materials all over the world, but mostly in industry.

Controlling oxygen permeability is especially important in the pharmaceutical industry and in food packaging. The oxygen permeability of polymers varies in a wide range covering several orders of magnitudes from a few hundred to a few hundredths or even thousands of $cm^3 \cdot mm/m^2/24$ h/bar [20]. Ethylene-vinyl alcohol copolymers (EVOH) offer extremely good protection against oxygen [20–25]. The barrier properties of these materials depend on ethylene content [23, 26, 27], crystallinity, temperature [22, 28] and humidity [24, 26–34]. The last factor represents also the major drawback of EVOH, since permeability may increase by orders of magnitudes with increasing water content [28]. Various

*Corresponding author, e-mail: krenner@mail.bme.hu

solutions exist to overcome this drawback. One of them is the production of multilayer films consisting of an EVOH barrier layer between polyolefin outer layers combined by the use of adhesive functional polymers [27, 35–37]. Development led to the production of packaging films with 9 or 10 layers combining EVOH, polyamide (PA) and polyolefins [38]; microfilms with 30–1000 layers of 0.02–5 μm thickness also appeared on the market recently [39].

Another approach to decrease the oxygen permeability and water sensitivity of EVOH is modification by blending [29, 35, 40–49] or by the production of layered silicate nanocomposites [50–57]. EVOH is combined with polyamides the most frequently, but blending results in decreased crystallinity and the desired improvement in permeability is seldom achieved. Better results are claimed with layered silicates which are supposed to exfoliate completely in EVOH, increase tortuosity and decrease permeability considerably. Unfortunately the control of structure is difficult in polymer/layered silicate nanocomposites [58], complete exfoliation is rarely achieved [59], organophilic silicates are quite expensive and they often discolor the product [60]. All the above presented examples prove the need for solutions, which result in a further decrease in the oxygen permeability of EVOH.

During the literature study of the topic, we have not found any indication of using a small molecular weight additive for the improvement of the barrier properties of poly(ethylene-co-vinyl alcohol) against oxygen. The general idea and goal of our project was to explore this possibility and use N,N′-bis(2,2,6,6-tetramethyl-4-piperidyl)-isophthalamide (Nylostab SEED), which was originally developed for the protection of pigmented polyamides against light induced decomposition. The additive proved to be also an efficient nucleating agent in polyamides. Nucleation of EVOH might increase crystallinity thus decreasing oxygen permeability and water sensitivity as well. The compound contains several functional groups, which may interact with the –OH group of EVOH thus changing free volume and offering a further route to modify oxygen permeability. EVOH containing the additive in a relatively wide composition range was produced and various properties were determined in the study. A detailed analysis of structure and interactions is presented in the paper to shed light onto the reason of the observed effects and correlations.

2. Experimental

The poly(ethylene-co-vinyl alcohol) polymer (EVOH) used in the experiments was the Eval G156 grade acquired from Eval Europe, Belgium. Its ethylene content is 48 mol%, density 1.12 g/cm^3 and its melt flow index is 6.4 g/10 min at 190°C and 2.16 kg. The additive, N,N′-bis(2,2,6,6-tetramethyl-4-piperidyl)-isophthalamide (Nylostab SEED, in further discussion Seed) is the product of Clariant, Germany. The chemical structure of the additive is shown in Figure 1. It is a sterically hindered amine (HALS) product, a crystalline material with melting temperature of 272°C and density of 1.12 g/cm^3. Experiments were carried out at 0, 0.1, 0.2, 0.3, 0.4, 0.5, 0.8, 1.0, 2.5, 5.0, 7.5 and 10.0 wt% additive contents.

Components were homogenized in a Brabender single screw extruder at 30 rpm and 260–270–280–260°C zone temperatures. The extruder was equipped with a die of single orifice of 3 mm diameter. The extruded strand was cooled in air and then pelletized. The pellets were compression molded to plates of 1 mm and films of about 100 μm thickness at 190°C using a Fontijne SRA 100 machine. Before processing all materials were dried at 100°C for 4 hours in an oven and then kept in a desiccator until further use.

Melting and crystallization characteristics and the possible nucleation effect of the additive were determined by differential scanning calorimetry (DSC) using a Perkin Elmer DSC 7 apparatus. The measurements were done on 3–5 mg samples cut from the 1 mm thick plates. Two heating and a cooling run were carried out at 10°C/min heating and cooling rate in the temperature range of 30–300°C. Crystallinity was calculated from the enthalpy of fusion (157.8 J/g) of the EVOH single crystal of 100% crystallinity [61]. Crystalline structure was also studied

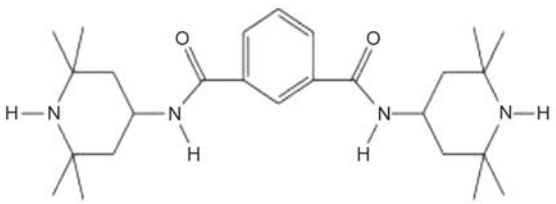

Figure 1. Chemical structure of the additive used in the experiments (Seed)

by X-ray diffraction. XRD patterns were recorded using a Phillips PW 1830/PW 1050 equipment with CuK_α radiation at 40 kV and 35 mA in the reflection mode. The traces were recorded in 0.04° steps with a sampling interval of 1 s and a rate of 0.04°/min in the 2θ range of 3–43°. Crystallinity was calculated from the XRD traces with the method proposed by Brückner [62].

Molecular interactions were studied by Fourier transform infrared spectroscopy (FTIR). The measurement were carried out in the attenuated total reflection (ATR) mode and the spectra were recorded in the wavelength range of 4000–400 cm^{-1} with 16 scans in 4 cm^{-1} steps using a Perkin Elmer Spectrum 100 apparatus. Molecular modeling was used to check possible interactions between the additive and the polymer and to estimate their strength. To reduce the necessary time and computer capacity to a reasonable level, we selected a small molecular weight model compound (1,4-buthanediol) representing the repeating unit of the polymer. We focused only on specific interactions, i.e. hydrogen bonds, and neglected dispersion interactions in the analysis. All the geometry optimizations for the model system were performed at the density functional theory (DFT) level using the MPW1B95 (modified Perdew and Wang exchange and Becke's 1995 correlation) functional [63] as well as the 6-31++G** basis set [64].

The density of the polymer was measured at room temperature in n-hexane using a pycnometer. A Systec Instruments Model 8000 apparatus (Thame, Oxfordshire, England) was applied for the permeation measurements, which were carried out according to the ASTM D 3985 standard in three parallel measurements. The test area and thickness of the sample were 50 cm^2 and about 100 μm, respectively, for all specimens. Oxygen transmission rate (OTR) was detected at 23°C and 50% relative humidity. Mechanical properties were characterized by tensile testing using an Instron 5566 machine at 115 mm gauge length and 5 mm/min cross-head speed on five parallel specimens with 1×10 mm dimensions according to the ISO 527 standard. The haze of the samples was determined with the help of a ColorQuest (HunterLab, Reston, US) apparatus.

3. Results and discussion

The results are presented in several sections. First, the effect of the additive on the properties of the polymer is shown and then the structure of the latter is analyzed in detail. Solubility and interactions are considered in the next two sections, and then correlations are discussed and a brief reference is made to consequences for practice in the last section.

3.1. Properties

The main hypothesis of the project was that similarly to PA, Seed will nucleate also EVOH, increase crystallinity and oxygen permeability decreases as an effect. The OTR of films is plotted against additive content in Figure 2.

Permeability decreases at small Seed concentrations as expected, but increases considerably at larger additive contents. The initial decrease seems to be small, but it is approximately 30%, which is more than any effect achieved by blending and only slightly smaller than the claimed decrease resulting from the use of layered silicates (~50%) [55, 56], but without the disadvantageous effect of the latter. We may conclude as a result that the additive influences oxygen permeability indeed, but the reason for the effect must be identified by further study and analysis. Changes in other properties and the analysis of structure should offer more information about the mechanism and origin of the effect. The increase in permeability at large additive content merits further considerations as well. If nucleation and changes in crystalline structure result in the improvement observed, one would expect a saturation effect, OTR remaining constant at large SEED contents. Obviously, some other, probably structural changes lead to the minimum in the OTR vs. additive content correlation

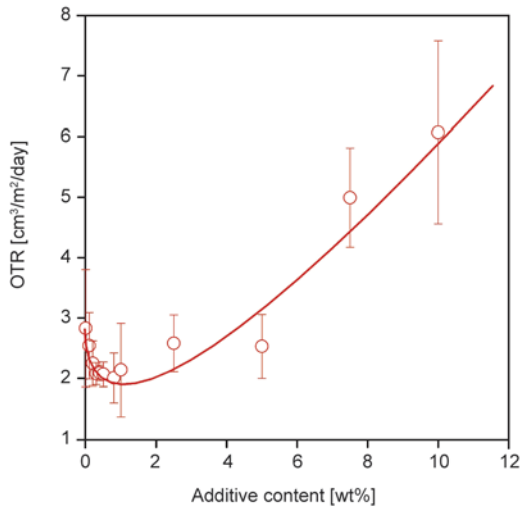

Figure 2. Effect of Seed content on the oxygen permeation of EVOH films

resulting from the superposition of two different effects.

The influence of the additive on the Young's modulus of the polymer is presented in Figure 3. The results strongly corroborate our preliminary assumption, stiffness increases with increasing additive content presumably because of increasing crystallinity and probably larger lamella thickness [65]. Similarly to OTR, two stages can be observed in the composition dependence of Young's modulus as well. Stiffness increases quite steeply at small and somewhat more moderately at larger additive contents, above 1.5–2.0 wt%. Ultimate tensile properties are presented as a function of additive content in Figure 4. The changes in tensile strength agree more or less with the results presented in Figures 2 and 3, i.e. strength increases considerably at small additive contents. On the other hand, the composition dependence of deformability seems to contradict our initial assumption. Changing crystallinity leading to larger stiffness usually results in decreased deformability and not to increased elongation-at-break. Simultaneous increase of strength and deformability often indicates changing structure, like physical or chemical cross-linking or decreased crystallinity. Moreover, the maximum in both quantities hints also to further structural changes, to the probability of phase separation caused by the limited solubility of the additive in the polymer. A heterogeneous, two-phase structure with weak interfacial interaction of the phases could result in the decrease of strength and deformability at large additive contents.

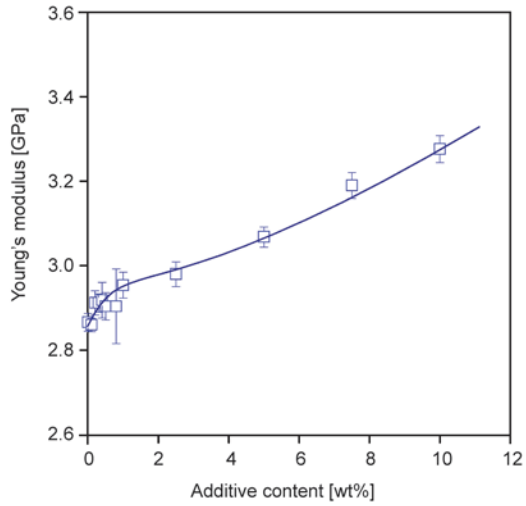

Figure 3. Dependence of the stiffness of EVOH plates on additive content

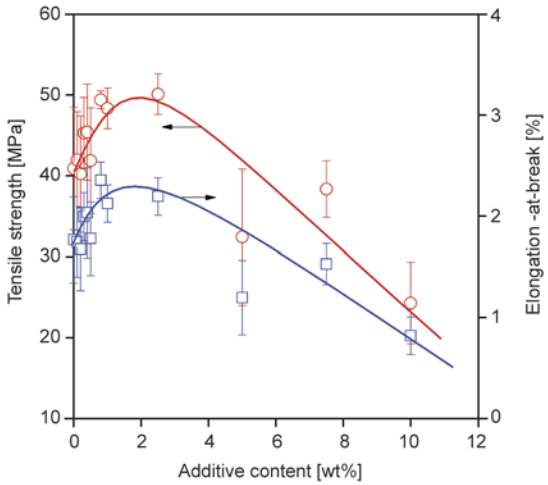

Figure 4. Ultimate tensile properties of EVOH plotted against Seed content. Symbols: (○) tensile strength, (□) elongation-at-break.

3.2. Structure

The modulus of crystalline polymers is determined mainly by crystallinity and the thickness of the lamella grown during crystallization [65]; lamella thickness increases with increasing crystallization temperature, thus also with nucleation [66, 67]. The heat of fusion proportional to crystallinity is plotted against additive content in Figure 5. Rather surprisingly crystallinity does not increase, but decreases with increasing additive content. The detailed analysis of the DSC traces recorded in the two heating and the cooling runs indicated that Seed does not nucleate EVOH. All quantities related to crystallinity (heat of fusion, heat of crystallization) decreased with increasing additive content, the melting temperature was constant in both heating runs and the temperature of crystallization also decreased as

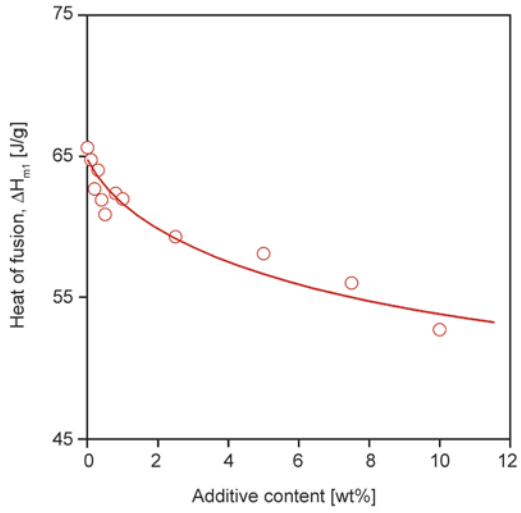

Figure 5. Effect of additive content on the crystallinity (ΔH_{m1}) of EVOH

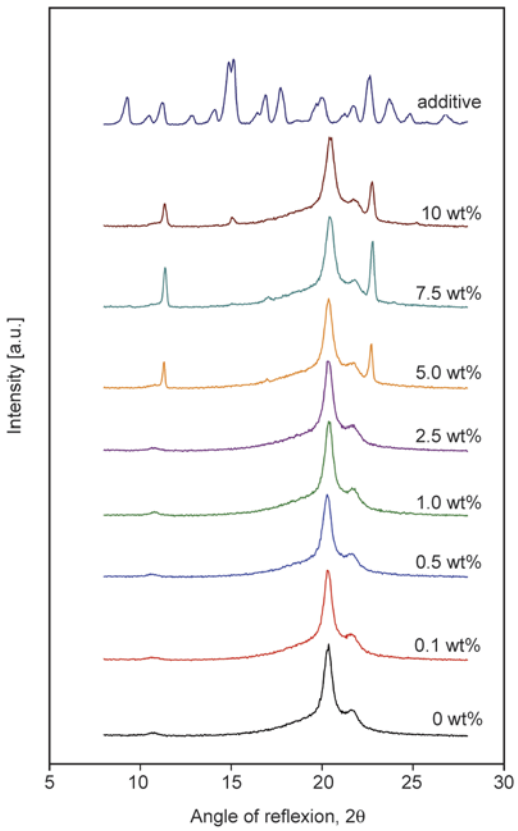

Figure 6. XRD traces of EVOH containing various amounts of Seed additive

Seed content increased. These results clearly indicate that the decrease in OTR as an effect of the additive is not caused by changing crystalline structure, but by some other factor or factors.

XRD spectra were also recorded and analyzed in order to confirm the modification of crystalline structure. The traces are presented in Figure 6 for selected compositions. Crystal form does not change at small additive content, but new peaks appear on the traces above 2.5 wt% Seed content. Possible changes in crystallinity cannot be deduced from the traces in this form, but their quantitative analysis by the approach of Brückner [62] allowed the determination of crystallinity, which is plotted against additive content in Figure 7. The correlation is practically identical to the one presented in Figure 5, and plotting the two quantities, i.e. the heat of fusion and crystallinity determined by XRD, against each other yielded a straight line with negligible scatter (not shown). These results further confirm that crystallinity does not increase, but decreases as an effect of the additive, this latter does not nucleate EVOH and the changes observed in properties are caused by another factor, probably by interactions.

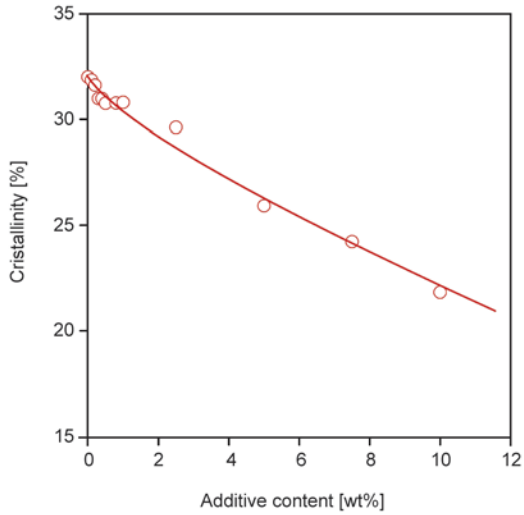

Figure 7. Decreasing crystallinity with increasing additive content as determined by XRD analysis

3.3. Solubility

The extremes in Figures 2 and 4 indicated the modification of structure, which cannot result from changing crystallinity, since it decreases monotonously with increasing additive content. A possible reason might be phase separation, the limited solubility of the additive in the polymer. A further indication for the existence of separate phases was supplied by the XRD traces presented in Figure 6. Above 2.5 wt% Seed content new peaks appear in the traces, which correspond to certain reflections of the additive. Obviously, the additive is present as a separate phase in crystalline form at these concentrations.

Changes in the optical properties of polymers may also reveal phase changes. Crystalline units as well as dispersed particles are often large enough to interfere with visible light and this interference results in considerable haze that is often used for the characterization of the optical properties of plastic products. Haze is the total flux of light scattered within the angular range between 2.5 and 90° and normalized to the total transmitted flux [68]. Haze indicates changes in optical properties more sensitively than transparency, which is the fraction of incident light that passes through an object. The haze value of the plates containing different amounts of Seed is plotted as a function of composition in Figure 8. The correlation is very interesting and clearly reveals all structural changes in the polymer as an effect of increasing additive content. Haze decreases at small additive concentrations due to decreasing crystallinity. At around 2 wt% Seed con-

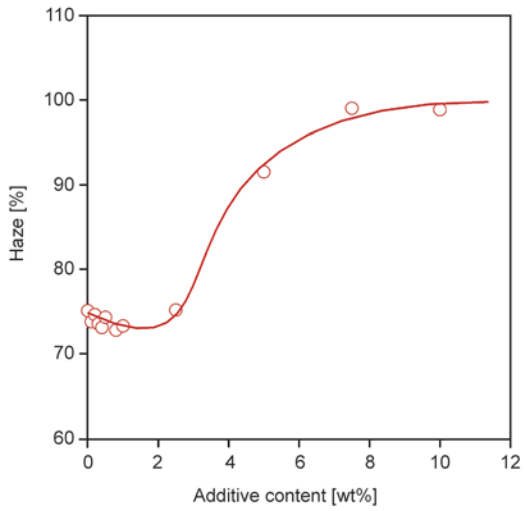

Figure 8. Effect of additive content on the haze of 1 mm thick EVOH plates

tent haze starts to increase and reaches practically 100% at the largest additive content because of phase separation and the presence of large dispersed particles. These changes agree well both with the XRD results (Figure 6), but also with the changes in mechanical properties (Figures 3 and 4).

3.4. Interactions

The functional groups of the additive and the hydroxyl groups of the polymer may develop relatively strong interactions. Molecular modeling by using the DFT approach showed that hydrogen bonds can form between the two substances indeed (see Figure 9). The two compounds are in the lowest energy state when the hydroxyl group of the polymer and the carbonyl of the additive are at about 2 Å distance from each other which corresponds to the distance of hydrogen bonds. The energy of the interaction is 28 kJ/mol, which is relatively strong. The interaction should result in a shift of the corresponding absorptions bands in the infrared spectrum of the material.

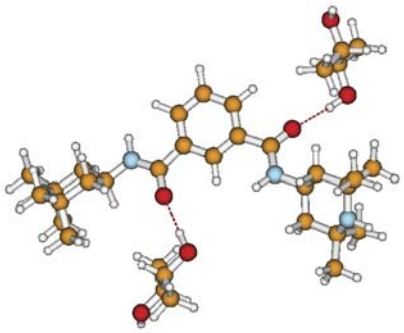

Figure 9. Formation of hydrogen bonds between EVOH and Seed; DFT modeling

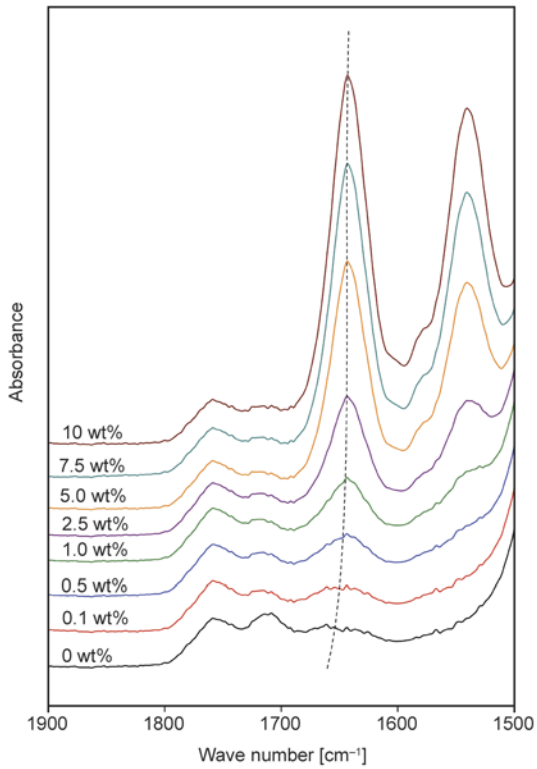

Figure 10. Shift in the position of the carbonyl absorption of amide groups with increasing additive content

The spectra are presented in Figure 10 for selected additive contents in the range of the carbonyl vibration of the amide group (around 1650 cm^{-1}). A considerable shift can be observed at small additive contents, which seems to level out at larger amounts of Seed, but the spectra in Figure 10 do not allow a more precise determination of band shifts. The results

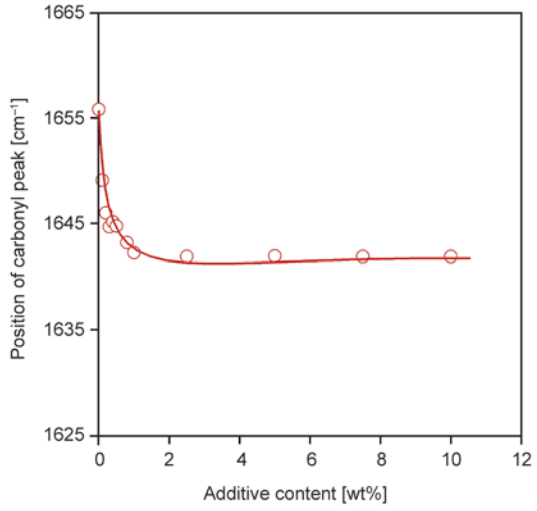

Figure 11. Effect of additive content on the position of the carbonyl absorption of amide groups

of quantitative analysis are shown in Figure 11, in which the position of the carbonyl absorption is plotted against additive content. The absorption band shifts more than 10 cm^{-1} wavelength in the range of 0–2 wt% additive content and remains constant afterwards. The strong shift corroborates previous results and further justifies the changes in structure and properties presented in previous sections. The results clearly prove that not crystalline structure, but interactions determine properties in the EVOH/additive system studied.

3.5. Discussion

The control of oxygen permeation has strong practical relevance. EVOH is one of the polymers with the smallest oxygen permeation, but many attempts are made to improve barrier properties even further [38, 47, 50, 55]. Most of these approaches failed to result in sufficient improvement in this property. Instead of blending or using fillers, we added a small molecular weight additive to EVOH to decrease oxygen permeation with positive results. Although the change in the targeted property is relatively small, it is significant. Contrary to our original assumption the additive, i.e. Seed, does not act as a nucleating agent, but the effect observed can be assigned to molecular interactions.

Both molecular modeling and FTIR spectroscopy proved that the –OH groups of the polymer and the amide groups of the additive strongly interact with each other and this interaction results in all the observed changes in properties. Because of interactions, crystallinity decreases somewhat, but the decrease does not result in smaller stiffness and strength. At small concentrations the additive dissolves in the amorphous phase of the polymer decreasing molecular mobility. Decreased mobility results in increased stiffness and strength, but also increased overall deformability due to the physical cross-link points created by hydrogen bonds. Smaller mobility and hydrogen bonds decrease also oxygen diffusion, the direct effect of which is clearly shown by Figure 12. Smaller molecular mobility is accompanied by decreased free volume resulting in smaller OTR [69].

Up to the solubility level a very close linear correlation exists between oxygen permeability and the shift in the position of the carbonyl absorption of the amide groups. Above the solubility limit, which is around 2.0 wt% the additive forms a separate phase. Phase separation leads to a maximum in ultimate tensile properties (Figure 4), the appearance of new reflections in the XRD spectra (Figure 6) and the deviation from the straight line in Figure 12. The results strongly corroborate the effect of the additive on the structure and properties of EVOH and show a novel way to control oxygen permeation in such polymers.

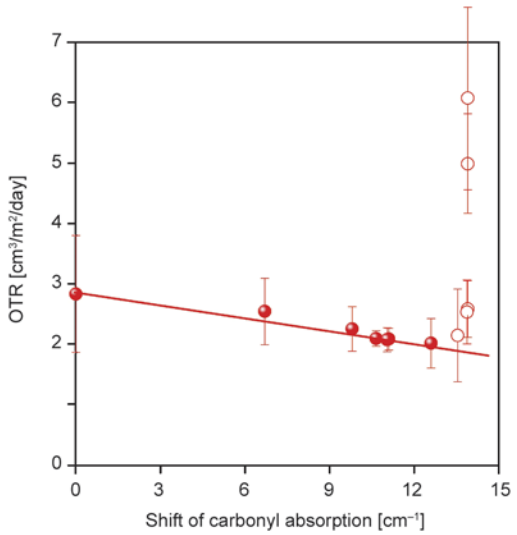

Figure 12. Direct correlation between oxygen permeation and molecular interactions (carbonyl shift); full symbols: below solubility level, empty symbols: separate additive phase

4. Conclusions

Poly(ethylene-co-vinyl alcohol) of 48 mol% ethylene content was modified with N,N′-bis(2,2,6,6-tetramethyl-4-piperidyl)-isophthalamide to decrease the oxygen permeability of the polymer even further. The results showed that oxygen permeation decreased considerably when the additive was added at less than 2.0 wt% concentration. The decrease resulted from the interaction of the hydroxyl groups of the polymer and the amide groups of the additive. The dissolution of the additive in the amorphous phase of the polymer led to decreased crystallinity, but also in the decreased mobility of amorphous molecules. Stiffness and strength, but also deformability increased as a result. Above 2 wt%, the additive forms a separate phase leading to the deterioration of properties. The success of the approach represents a novel way to control oxygen permeation in EVOH and in other polymers with similar functional groups capable of strong interactions.

Acknowledgements

The authors are indebted to Erika Selmeci for the execution of the FTIR measurements, to István Sajó for the XRD experiments, and to Mihály Kállay for the DFT calculations. The research on heterogeneous polymer systems was financed by the National Scientific Research Fund of Hungary (OTKA Grant No. K 101124) and partly by the former Süd-Chemie AG, today Clariant, Business Unit Masterbatches, on functional packaging materials; we appreciate the support very much. One of the authors (KR) is grateful also to the János Bolyai Research Scholarship of the Hungarian Academy of Sciences.

References

[1] Summers L.: Intelligent packaging. Centre for Exploitation of Science and Technology. London (1992).

[2] Rooney M. L.: Active food packaging. Blackie Academic and Professional, London (1995).

[3] Brody A. L., Strupinsky E. R., Kline L. R.: Active packaging for food applications. CRC Press, London (2001).

[4] Ahvenainen R.: Novel food packaging techniques. Woodhead, Boca Raton (2003).

[5] Charles F., Sanchez J., Gontard N.: Absorption kinetics of oxygen and carbon dioxide scavengers as part of active modified atmosphere packaging. Journal of Food Engineering, **72**, 1–7 (2006).
DOI: 10.1016/j.jfoodeng.2004.11.006

[6] Byun Y., Darby D., Cooksey K., Dawson P., Whiteside S.: Development of oxygen scavenging system containing a natural free radical scavenger and a transition metal. Food Chemistry, **124**, 615–619 (2011).
DOI: 10.1016/j.foodchem.2010.06.084

[7] Busolo M. A., Lagaron J. M.: Oxygen scavenging polyolefin nanocomposite films containing an iron modified kaolinite of interest in active food packaging applications. Innovative Food Science and Emerging Technologies, **16**, 211–217 (2012).
DOI: 10.1016/j.ifset.2012.06.008

[8] Shirazi A., Cameron A. C.: Controlling relative humidity in modified atmosphere packages of tomato fruit. Hortscience, **27**, 336–339 (1992).

[9] Mahajan P. V., Rodrigues F. A. S., Motel A., Leonhard A.: Development of a moisture absorber for packaging of fresh mushrooms (*Agaricus bisporous*). Postharvest Biology and Technology, **48**, 408–414 (2008).
DOI: 10.1016/j.postharvbio.2007.11.007

[10] Sandhya: Modified atmosphere packaging of fresh produce: Current status and future needs. LWT – Food Science and Technology, **43**, 381–392 (2010).
DOI: 10.1016/j.lwt.2009.05.018

[11] Allinson J. G., Dansereau R. J., Sakr A.: The effects of packaging on the stability of a moisture sensitive compound. International Journal of Pharmaceutics, **221**, 49–56 (2001).
DOI: 10.1016/S0378-5173(01)00670-6

[12] Waterman K. C., MacDonald B. C.: Package selection for moisture protection for solid, oral drug products. Journal of Pharmaceutical Sciences, **99**, 4437–4452 (2010).
DOI: 10.1002/jps.22161

[13] García-García I., Taboada-Rodríguez A., López-Gomez A., Marín-Iniesta F.: Active packaging of cardboard to extend the shelf life of tomatoes. Food and Bioprocess Technology, **6**, 754–761 (2013).
DOI: 10.1007/s11947-011-0759-4

[14] Coma V.: Bioactive packaging technologies for extended shelf life of meat-based products. Meat Science, **78**, 90–103 (2008).
DOI: 10.1016/j.meatsci.2007.07.035

[15] Zema L., Sangalli M. E., Maroni A., Foppoli A., Bettero A., Gazzaniga A.: *Activepackaging* for topical cosmetic/drug products: A hot-melt extruded preservative delivery device. European Journal of Pharmaceutics and Biopharmaceutics, **75**, 291–296 (2010).
DOI: 10.1016/j.ejpb.2010.03.007

[16] Boschetto D. L., Lerin L., Cansian R., Pergher S. B. C., Di Luccio M.: Preparation and antimicrobial activity of polyethylene composite films with silver exchanged zeolite-Y. Chemical Engineering Journal, **204–206**, 210–216 (2012).
DOI: 10.1016/j.cej.2012.07.111

[17] Chen J., Brody A. L.: Use of active packaging structures to control the microbial quality of a ready-to-eat meat product. Food Control, **30**, 306–310 (2013).
DOI: 10.1016/j.foodcont.2012.07.002

[18] Jacobsen C., Let M. B., Nielsen N. S., Meyer A. S.: Antioxidant strategies for preventing oxidative flavour deterioration of foods enriched with n-3 polyunsaturated lipids: A comparative evaluation. Trends in Food Science and Technology, **19**, 76–93 (2008).
DOI: 10.1016/j.tifs.2007.08.001

[19] Mexis S. F., Badeka A. V., Riganakos K. A., Karakostas K. X., Kontominas M. G.: Effect of packaging and storage conditions on quality of shelled walnuts. Food Control, **20**, 743–751 (2009).
DOI: 10.1016/j.foodcont.2008.09.022

[20] Massey L. K.: Permeability properties of plastics and elastomers – A guide to packaging and barrier materials. William Andrew Publishing/Plastics Design Library, Norwich (2003).

[21] Armstrong R. B.: Effects of polymer structure on gas barrier of ethylene vinyl alcohol (EVOH) and considerations for package development. in 'TAPPI PLACE Conference, Boston, USA' 1–6 (2002).

[22] Yamamoto T., Nishihara Y.: Barrier properties of EVOH at low temperatures and various humidity. Paper Film and Foil Converter (2001).

[23] Advani S. G., Shonaike G. O.: Advanced polymeric materials. CRC Press, Boca Raton (2003).

[24] Lagaron J. M., Powell A. K., Bonner G.: Permeation of water, methanol, fuel and alcohol-containing fuels in high-barrier ethylene–vinyl alcohol copolymer. Polymer Testing, **20**, 569–577 (2001).
DOI: 10.1016/S0142-9418(00)00077-5

[25] Mokwena K. K., Tang J.: Ethylene vinyl alcohol: A review of barrier properties for packaging shelf stable foods. Critical Reviews in Food Science and Nutrition, **52**, 640–650 (2011).
DOI: 10.1080/10408398.2010.504903

[26] Cabedo L., Lagarón J. M., Cava D., Saura J. J., Giménez E.: The effect of ethylene content on the interaction between ethylene-vinyl alcohol copolymers and water – II: Influence of water sorption on the mechanical properties of EVOH copolymers. Polymer Testing, **25**, 860–867 (2006).
DOI: 10.1016/j.polymertesting.2006.04.012

[27] Cava D., Cabedo L., Gimenez E., Gavara R., Lagaron J. M.: The effect of ethylene content on the interaction between ethylene–vinyl alcohol copolymers and water: (I) Application of FT-IR spectroscopy to determine transport properties and interactions in food packaging films. Polymer Testing, **25**, 254–261 (2006).
DOI: 10.1016/j.polymertesting.2005.09.018

[28] Muramatsu M., Okura M., Kuboyama K., Ougizawa T., Yamamoto T., Nishihara Y., Saito Y., Ito K., Hirata K., Kobayashi Y.: Oxygen permeability and free volume hole size in ethylene–vinyl alcohol copolymer film: Temperature and humidity dependence. Radiation Physics and Chemistry, **68**, 561–564 (2003).
DOI: 10.1016/S0969-806X(03)00231-7

[29] Lagarón J. M., Giménez E., Gavara R., Saura J. J.: Study of the influence of water sorption in pure components and binary blends of high barrier ethylene–vinyl alcohol copolymer and amorphous polyamide and nylon-containing ionomer. Polymer, **42**, 9531–9540 (2001).
DOI: 10.1016/S0032-3861(01)00496-7

[30] Zhang Z., Britt I. J., Tung M. A.: Permeation of oxygen and water vapor through EVOH films as influenced by relative humidity. Journal of Applied Polymer Science, **82**, 1866–1872 (2001).
DOI: 10.1002/app.2030

[31] Mokwena K. K., Tang J., Laborie M-P.: Water absorption and oxygen barrier characteristics of ethylene vinyl alcohol films. Journal of Food Engineering, **105**, 436–443 (2011).
DOI: 10.1016/j.jfoodeng.2011.02.040

[32] López-Rubio A., Lagaron J. M., Giménez E., Cava D., Hernandez-Muñoz P., Yamamoto T., Gavara R.: Morphological alterations induced by temperature and humidity in ethylene–vinyl alcohol copolymers. Macromolecules, **36**, 9467–9476 (2003).
DOI: 10.1021/ma035346j

[33] Aucejo S., Marco C., Gavara R.: Water effect on the morphology of EVOH copolymers. Journal of Applied Polymer Science, **74**, 1201–1206 (1999).
DOI: 10.1002/(SICI)1097-4628(19991031)74:5<1201::AID-APP17>3.0.CO;2-8

[34] Yamamoto T., Kanda T., Nishihara Y., Ooshima T., Saito Y.: Correlation study among oxygen permeability, molecular mobility, and amorphous structure change of poly(ethylene-vinylalcohol copolymers) by moisture. Journal of Polymer Science Part B: Polymer Physics, **47**, 1181–1191 (2009).
DOI: 10.1002/polb.21723

[35] Yeh J-T., Huang S-S., Yao W-H., Wang I-J., Chen C-C.: Oxygen permeation resistance of polyethylene, polyethylene/ethylene vinyl alcohol copolymer, polyethylene/modified ethylene vinyl alcohol copolymer, and polyethylene/modified polyamide–ethylene vinyl alcohol copolymer bottles. Journal of Applied Polymer Science, **92**, 2528–2537 (2004).
DOI: 10.1002/app.20215

[36] López-Rubio A., Lagarón J. M., Hernández-Muñoz P., Almenar E., Catalá R., Gavara R., Pascall M. A.: Effect of high pressure treatments on the properties of EVOH-based food packaging materials. Innovative Food Science and Emerging Technologies, **6**, 51–58 (2005).
DOI: 10.1016/j.ifset.2004.09.002

[37] Dhawan S., Barbosa-Cànovas G. V., Tang J., Sablani S. S.: Oxygen barrier and enthalpy of melting of multilayer EVOH films after pressure-assisted thermal processing and during storage. Journal of Applied Polymer Science, **122**, 1538–1545 (2011).
DOI: 10.1002/app.34267

[38] Schut J. H.: Nine-layer. Plastics Technology, **51**, 54–59 (2005).

[39] Schut J. H.: Microlayer films. Plastics Technology, **52**, 54–60 (2006).

[40] Samios C. K., Kalfoglou N. K.: Acrylic-modified polyolefin ionomers as compatibilizers for poly(ethylene-*co*-vinyl alcohol)/aromatic copolyester blends. Polymer, **42**, 3687–3696 (2001).
DOI: 10.1016/S0032-3861(00)00432-8

[41] Lasagabáster A., Abad M. J., Barral L., Ares A., Bouza R.: Application of FTIR spectroscopy to determine transport properties and water–polymer interactions in polypropylene (PP)/poly(ethylene-*co*-vinyl alcohol) (EVOH) blend films: Effect of poly(ethylene-*co*-vinyl alcohol) content and water activity. Polymer, **50**, 2981–2989 (2009).
DOI: 10.1016/j.polymer.2009.04.005

[42] Yeh J-T., Yao W-H., Du Q., Chen C-C.: Blending and barrier properties of blends of modified polyamide and ethylene vinyl alcohol copolymer. Journal of Polymer Science Part B: Polymer Physics, **43**, 511–521 (2005).
DOI: 10.1002/polb.20344

[43] Yeh J-T., Chen H-Y.: Blending and oxygen permeation properties of the blown films of blends of modified polyamide and ethylene vinyl alcohol copolymer with varying vinyl alcohol contents. Journal of Materials Science, **42**, 5742–5751 (2007).
DOI: 10.1007/s10853-006-0555-0

[44] Papadopoulou C. P., Kalfoglou N. K.: Compatibility study of binary and ternary PVOH/polyolefin blends. Polymer, **38**, 4207–4213 (1997).
DOI: 10.1016/S0032-3861(96)01009-9

[45] Földes E., Pukánszky B.: Miscibility–structure–property correlation in blends of ethylene vinyl alcohol copolymer and polyamide 6/66. Journal of Colloid and Interface Science, **283**, 79–86 (2005).
DOI: 10.1016/j.jcis.2004.08.175

[46] Lagarón J. M., Giménez E., Saura J. J., Gavara R.: Phase morphology, crystallinity and mechanical properties of binary blends of high barrier ethylene–vinyl alcohol copolymer and amorphous polyamide and a polyamide-containing ionomer. Polymer, **42**, 7381–7394 (2001).
DOI: 10.1016/S0032-3861(01)00204-X

[47] de Lima J. A., Felisberti M. I.: Poly(ethylene-*co*-vinyl alcohol) and poly(methyl methacrylate) blends: Phase behavior and morphology. European Polymer Journal, **44**, 1140–1148 (2008).
DOI: 10.1016/j.eurpolymj.2008.02.001

[48] Kim S. W., Hwang G. S.: A study on the morphology and properties of PP/(Nylon-EVOH) blends. Applied Chemistry, **9**, 45–48 (2005).

[49] Russo P., Acierno D., Maio L. D., Demma G.: Thermal and mechanical characterisation of films from Nylon 6/EVOH blends. European Polymer Journal, **35**, 1261–1268 (1999).
DOI: 10.1016/S0014-3057(98)00197-9

[50] Cabedo L. S., Giménez E., Lagaron J. M., Gavara R., Saura J. J.: Development of EVOH-kaolinite nanocomposites. Polymer, **45**, 5233–5238 (2004).
DOI: 10.1016/j.polymer.2004.05.018

[51] Aktzi N., Nir Y., Wang D., Narkis M., Siegmann A.: EVOH/clay nanocomposites produced by melt processing. Polymer Composites, **22**, 710–720 (2001).
DOI: 10.1002/pc.10573

[52] Lucciarini J. M., Ratto J. A., Koene B. E., Powell B.: Nanocomposites study of ethylene *co*-vinyl alcohol and montmorillonite clay. in 'SPE ANTEC Proceeding, San Francisco, USA' 760–764 (2002).

[53] Artzi N., Narkis M., Siegmann A.: Review of melt-processed nanocomposites based on EVOH/organoclay. Journal of Polymer Science Part B: Polymer Physics, **43**, 1931–1943 (2005).
DOI: 10.1002/polb.20481

[54] Jeong H., Kim B., Kim E.: Structure and properties of EVOH/organoclay nanocomposites. Journal of Materials Science, **40**, 3783–3787 (2005).
DOI: 10.1007/s10853-005-3719-4

[55] Lagaron J. M., Cabedo L., Cava D., Feijoo J. L., Gavara R., Gimenez E.: Improving packaged food quality and safety. Part 2: Nanocomposites. Food Additives and Contaminants, **22**, 994–998 (2005).
DOI: 10.1080/02652030500239656

[56] Kim S. W., Cha S-H.: Thermal, mechanical, and gas barrier properties of ethylene–vinyl alcohol copolymer-based nanocomposites for food packaging films: Effects of nanoclay loading. Journal of Applied Polymer Science, **131**, in press (2013).
DOI: 10.1002/app.40289

[57] Lagaron J. M., Gimenez E., Sanchez-Garcia M. A., Ocio M. J., Fendler A.: Novel nanocomposites to enhance quality and safety of packaged foods. in 'Food Contact Polymers-Intenational Conference, Brussels, Belgium' p.6 (2007).

[58] Százdi L., Pozsgay A., Pukánszky B.: Factors and processes influencing the reinforcing effect of layered silicates in polymer nanocomposites. European Polymer Journal, **43**, 345–359 (2007).
DOI: 10.1016/j.eurpolymj.2006.11.005

[59] Ábrányi Á., Százdi L., Pukánszky B. Jr., Vancsó G. J., Pukánszky B.: Formation and detection of clay network structure in poly(propylene)/layered silicate nanocomposites. Macromolecular Rapid Communications, **27**, 132–135 (2006).
DOI: 10.1002/marc.200500687

[60] Dominkovics Z., Hári J., Fekete E., Pukánszky B.: Thermo-oxidative stability of polypropylene/layered silicate nanocomposites. Polymer Degradation and Stability, **96**, 581–587 (2011).
DOI: 10.1016/j.polymdegradstab.2010.12.012

[61] Franco-Urquiza E., Santana O. O., Gámez-Pérez J., Martínez A. B., Maspoch M. L.: Influence of processing on the ethylene-vinyl alcohol (EVOH) properties: Application of the successive self-nucleation and annealing (SSA) technique. Express Polymer Letters, **4**, 153–160 (2010).
DOI: 10.3144/expresspolymlett.2010.20

[62] Brückner S.: Estimation of the background in powder diffraction patterns through a robust smoothing procedure. Journal of Applied Crystallography, **33**, 977–979 (2000).
DOI: 10.1107/s0021889800003617

[63] Zhao Y., Truhlar D. G.: Hybrid meta density functional theory methods for thermochemistry, thermochemical kinetics, and noncovalent interactions: The MPW1B95 and MPWB1K models and comparative assessments for hydrogen bonding and van der Waals interactions. The Journal of Physical Chemistry A, **108**, 6908–6918 (2004).
DOI: 10.1021/jp048147q

[64] Krishnan R., Binkley J. S., Seeger R., Pople J. A.: Self-consistent molecular orbital methods. XX. A basis set for correlated wave functions. The Journal of Chemical Physics, **72**, 650–654 (1980).
DOI: 10.1063/1.438955

[65] Pukánszky B., Mudra I., Staniek P.: Relation of crystalline structure and mechanical properties of nucleated polypropylene. Journal of Vinyl and Additive Technology, **3**, 53–57 (1997).
DOI: 10.1002/vnl.10165

[66] Wunderlich B.: Thermal analysis of polymeric materials. Springer, Berlin (2005).

[67] Horváth Zs., Menyhárd A., Doshev P., Gahleitner M., Tranninger C., Kheirandish S., Varga J., Pukánszky B.: Effect of molecular architecture on the crystalline structure and stiffness of iPP homopolymers: Modeling based on annealing experiments. Journal of Applied Polymer Science, **130**, 3365–3373 (2013).
DOI: 10.1002/app.39585

[68] Meeten G. H.: Optical properties of polymers. Elsevier, London (1986).

[69] Dhawan S., Varney C., Barbosa-Cánovas G. V., Tang J. M., Selim F., Sablani S. S.: Pressure-assisted thermal sterilization effects on gas barrier, morphological, and free volume properties of multilayer EVOH films. Journal of Food Engineering, **128**, 40–45 (2014)
DOI: 10.1016/j.jfoodeng.2013.12.012

eXPRESS Polymer Letters Vol.8, No.10 (2014) 767–778
Available online at www.expresspolymlett.com
DOI: 10.3144/expresspolymlett.2014.79

The utilization of biochemically modified microfibers from grain by-products as reinforcement for polypropylene biocomposite

A. K. Bledzki[1], *P. Franciszczak*[1*], *A. Mamun*[2]

[1]West Pomeranian University of Technology Szczecin, Faculty of Mechanical Engineering and Mechatronics, Institute of Materials Science, Piastów 19 Avenue, 70-310 Szczecin, Poland
[2]Universität Kassel, Institut für Werkstofftechnik, Mönchebergstr. 3, 34125 Kassel, Germany

Received 1 April 2014; accepted in revised form 31 May 2014

Abstract. The presented research study aims to evaluate microfibers from grain by-products as a substitute for wood flour in wood-thermoplastic composites. Grain husks are an abundant and cheap source of annual, renewable raw material, which besides lignocellulose, may also contain substantial amounts of starch, proteins and fats. These grain residues may negatively affect the mechanical properties of their composites, and generate an odor when decomposition occurs at higher temperatures during plastics processing. Such odors may also be present in the end-product. In order to overcome this drawback, in this research study, a simple and effective enzymatic treatment is proposed. This environmental friendly process removed protein, starch and fats in selective manner. Treated microfibers have shown enhanced thermal stability for ca. 20°C at 1% of weight loss. This correlates with lower amount of odor emission during plastics processing as well as in the final, injection molded parts (25–65% decrease). The mechanical properties of composites were either preserved, or slightly improved. All results were compared to standard injection molded softwood WPC.

Keywords: *biocomposites, lignocellulosic microfibers, grain by-products, enzymatic modification, olfactometry*

1. Introduction

Wood plastic composites (WPC) are the most widespread natural fiber composites (NFC), and have established their place on the market, because of their mechanical properties. Moreover, they are also known for more specific properties, i.e., their lightweight, vibration damping, and blunt fracture. Due to the high freedom of design and the low number of processing steps, WPC have a number of benefits in comparison to components made of wood. They can be processed using extrusion or injection molding, which are both highly efficient methods, and, thus, cost-effective. Furthermore, they meet the sustainability requirements, because they use materials made from raw, renewable resources. This, in turn, contributes to a lower environmental footprint. Their end-products are suitable for recycling, pyrolysis, or can be burned to create energy. These features make them suitable for applications in the automotive, furniture and household industries [1–6].

In recent years, the demand for WPC has risen by about 80 000 t/per annum. New applications for these materials are still being discovered. Annually, approximately 720 000 tons of WPC are produced. Approximately 600 000 tons are produced in America, about 90 000 tons in Asia, and 30 000 tons in Europe [7]. However, the shortage of wood, and its rising prices make it necessary to search for substitutes for this raw material [4]. Grain husks or hull by-products from cereal processing are rich in lignocellulose.

*Corresponding author, e-mail: piotr.franciszczak@zut.edu.pl

Current research focuses on their utilization as a substitute for wood.

Wheat (*Triticum aestivum*) is the most common type of cereal used worldwide, and one of the most important raw materials for the food industry. According to the Food and Agricultural Organization of the United Nations (FAO), its global production reached 671 million tons in 2012, 196 million tons of which were harvested in Europe. Rye crops (*Secale cereale*) equaled 14.5 million tons worldwide, and approximately 12.7 million tons in Europe. Rice paddy (*Oryza sativa*) was estimated to 720 million tons, 4.3 million tons of which were harvested in Europe [8]. The brans (hard outer layers of cereal grain) and husks (scaly protective casings of the seeds) comprise varying parts of whole grains depending on a crop's species and variety. Spelt (*Triticum spelta*) husks used in this research study consist of up to 20–30% grain [9, 10]. Similar amounts of husks are in rice paddy, while rye bran is made up of 10–15% grain [11–13].

Owing to their low nutritional content, wheat and rye brans are usually used as additives in feed. Unfortunately, the outer layers of the grains are exposed to pesticides, or herbicides, and mycotoxins [14]. In the case of hard husks, like rice husks, it is possible to use them as fuel for burning. Although they have a relatively high caloric value, half of which is coal [15], they are rich in silica (ca. 20%) and other minerals. As a consequence, there are problems concerning the disposal of their volatile ashes [16].

Recently, pilot applications were proposed at paper mills [17]. Another approach focuses on the conversion of lignocellulosic waste materials into bioethanol using enzymes. This process is still being developed, and has encountered some obstacles since lignocellulose consists of many complex polysaccharides so enzymes of combined activities have to be used to break down all the matter into glucose [18–20].

Besides being used as a biomass, they appear to be an appropriate and abundant source for lignocellulose fibers, which can be processed directly after dehusking of the grains. The WPC processors and mills estimate that the price of microfibers prepared from grain by-products is about twice lower than that of microfibers from wood, and the acquisition is simplified. Moreover, they are obtained from annual plants, making them even more sustainable than wood fibers processed from trees [21–23]. The only obstacle which may arise is caused by the contamination of husks with starch, proteins and fats from grain rests. These chemical compounds are less temperature-stable, and lead to the deterioration of the fiber-to-matrix bond. In this case, enzymatic treatment with appropriate hydrolases can remove these unwanted compounds without damaging the cellulose structure. In the case of enzymatic treatment of grain by-products, complexity of multi polysaccharide structure of lignocellulose, thus its resistance to enzymatic breakdown can be favorable when desiring to preserve its chemical structure. Some research has already been done in the field of enzymatic treatment of natural fibers of bast or leaf origin. In those cases, mainly pectinase was used to improve the fibrillation, and remove waxes attached by pectins to the outer cell walls. Modest improvements have been achieved in comparison to traditional methods. The so-called bio-scouring process is currently still under development, also in large companies [24–26].

The presented research study focuses on the manufacture of natural fiber composites reinforced with microfibers from spelt and rice husks and rye brans, which are common cereals in Europe and Asia. The husk and brans were ground to smaller fibrous particles, and, subsequently, enzymatically treated prior to pellet manufacturing by compounding them with a polymer matrix and compatibilizer. These composites are oriented to processing by means of injection molding. Fine particle sizes were chosen, which enable an easy melt flow, and which help to avoid impact cracking typical for the composite reinforced with coarse particle sizes. The enzymatic treatment proposed in the course of this research is necessary for all applications of these biocomposites where odor emission can exclude them from usage – these are furniture, housing and automotive parts.

The results found for the properties of the natural fiber composites reinforced with microfibers were compared with standard, injection molded, softwood reinforced WPC that was modified and processed in the same way.

2. Materials and methods

2.1. Materials

Injection molding grade polypropylene HP400R of Bassel-Orlen, Poland, was used as a matrix. This homopolymer exhibits good stiffness and high fluidity of MFR = 25 and MVR = 34 (230°C/2.16 kg).

Microfibers used as reinforcement were prepared at the Institute für Lebensmittel und Umweltforschung, Potsdam, Germany, by conditioning and milling spelt (*Triticum spelta*) and rice husks (*Oryza sativa*) and rye brans (*Secale cereale*) into particles sizes smaller than 600 μm. For reference purposes, microfibers made of the industrial grade softwood flour Jeluxyl Weho500 by Jeluwerk, Germany were used. Jeluxyl Weho500 consists of a mix of European spruce (*Picea abies*) and silver fir (*Abies alba*). A matrix-to-fiber weight ratio of 60/40 was used for all composites.

Three types of enzyme hydrolases were used to remove starch, protein and fat residues from the microfibers, namely alpha-amylase, protease and lipase. The commercial grade enzymes provided by Novozymes, Denmark are listed in Table 1. The alpha-amylase, lipase and protease employed were designed to be used in washing processes, which is why they have broad pH and temperature spectrums. Moreover these products have improved thermal stability.

Maleic acid anhydride grafted PP wax (MAH-g-PP) TP Licocene PP MA 6452 from Clariant, Germany of 3.3 wt% in relation to the matrix was applied as a compatibilizer between a non-polar matrix and polar lignocellulosic fibers.

2.2. Methods

2.2.1. Enzymatic treatment of microfibers

The enzymatic treatment was performed in order to remove unwanted constituents from the microfibers. Fats, proteins and starch dust may remain on the grain during the dehulling and dehusking processes. Most of these low molecular weight compounds, especially lipids and proteins, decompose at lower temperatures than cellulose and hemicellulose (at approximately 200°C). Consequently, they undergo degradation during compounding and injection molding [27]. This tends to weaken the fiber/matrix interface, and causes the emission of volatile degradation products, which, in turn, increase the odor of the material significantly while darkening the color of the material. Enzymatic treatment ensures the selective hydrolysis of unwanted compounds to water soluble dextrins (from starch), amino acids (from proteins) and fatty acids and glycerol (from lipids) without damaging the structure. Moreover, the carbon footprint is extremely small [28].

The mixture of three different type of enzymes consisted of lipase, protease and alpha-amylase. Additionally, hemicellulase, namely Pulpzyme HC, was used in order to roughen the surface of the microfibers, and facilitate the removal of the starch, lipids and proteins from the surface of the input material. The citrate sodium hydroxide buffer was added to maintain the pH level. The use of sodium hydroxide is substantial for the hydrolysis of lipids to glycerol and fatty acids. They react with one another, and produce sodium soap which simultaneously wets the fats, and, therefore, facilitates the degradation of the lipids to a large extent.

The whole process profile of the enzymatic treatment is presented in Figure 1. The microfibers were added to distilled water in a 1:8 ratio, and stirred constantly throughout the entire treatment with enzymes. In the beginning, the pH level was set at 7 to work at the optimum level for Pulpzyme HC. In the first stage, Pulpzyme HC (xylanase) was added to the suspension together with Lipex 100L (lipase) and Termamyl 300L (alpha-amylase). Each added enzyme portion equaled 1 mL. This stage took

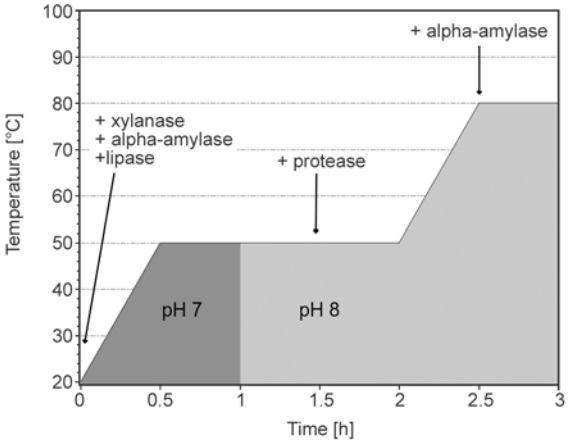

Figure 1. Process profile of enzymatic treatment

Table 1. Enzymes used in the processing of microfibers

Trade name	Chemical name	pH range	Temperature range [°C]	Type of reaction
Termamyl 300L	Alpha-amylase	6.5–9.5	20–90	Hydrolysis of α-1,4-bonds of amylose and amylopectin
Alcalase 2.5L	Protease	7–10	10–65	Broad spectrum of peptide bond hydrolysis
Lipex 100L	Lipase	7–11	20–60	Hydrolysis of carboxylic esters
Pulpzyme HC	Xylanase	6–8	50–60	β-1, 4 xylanase activity

approximately 30 min to complete, and was finished when suspension reached 50°C. It was kept at this temperature for the ensuing half hour.
In the second stage of the process, the pH level was set to 8, in order to be closer to the activity optimum of the rest of the enzymes. This level was maintained for half an hour before protease (Alcalase 2.5L) was added to hydrolyze the proteins. The same conditions as before were used for another half hour to let it react in optimal conditions. Protease induces degradation in other enzymes, so it was deactivated by increasing the temperature of the suspension to 80°C for the next 30 minutes.
In the third stage of the enzymatic treatment, the diluted crystalline starch was completely hydrolyzed to dextrose by adding a second dose of Termamyl 300L, which is a thermally stable alpha-amylase. Throughout the whole process, the concentration of the entire enzyme solutions equaled ca. 0.0625 wt%. After the enzymatic treatment, the fibers were rinsed with water to flush out the products of enzymatic hydrolysis.
In order to extend the previous research done by Mamun and Bledzki [29], the Weho500 (reference material) was also treated to evaluate the possibility of fiber damage during enzymatic treatment.

2.2.2. Characterization of microfibers

Chemical composition of microfibers

All chemical compositions of grain by-products were measured according to the official method of analysis of AOAC International (AOAC methods, 2007). The analytical results were measured twice, their standard deviation equaled 5%.

Cellulose, hemicellulose and lignin contents:
Neutral detergent dietary fiber (NDF), acid detergent dietary fiber (ADF) and acid detergent lignin (ADL) contents were measured using the Van Soest chemical method [1963; 1967] with modifications made by McQueen and Nicholson [1979]. Modification relied on the application of the alpha-amylase, in order to successfully degrade the starch. Dietary fiber was isolated by means of detergent solutions of acidic and neutral pH. Hot extractions of samples were carried out on a Fibertec apparatus produced by Foss Tecator (Sweden). The hemicellulose fraction was calculated on the basis of the NDF and ADF difference, while the cellulose fraction was calculated using the difference between ADF and ADL.

Starch contents:
The starch content was determined according to PN-R-64785:1994. This method relies on the dissolution of a sample material using hydrochloric acid, and measuring of specific rotation of light in clear extract using polarimeter.

Protein contents:
The protein content was determined using the Kjeldahl method, which involves the mineralization of samples using concentrated sulphuric acid. Subsequently, the amount of ammonia produced in the reaction is measured. In order to convert the nitrogen content to the protein content, the factor 6.25 was applied in accordance to PN-EN ISO 20483. This was carried out on a Kjeltec device setup by Foss Tecator (Sweden).

Fat content:
The fat content was determined according to PN-64/A74039 using a method of multiple extraction of samples with petroleum ether. After the ether evaporated, the remaining fat was weighed. A Soxtec HT6 setup by Foss Tecator (Sweden) was used was used to extract samples.

Thermal gravimetric analysis

The thermal gravimetric analysis (TGA) was carried out using the thermal gravimetric analyzer Q5000 by TA Instruments, USA. Samples were dried for 2 h at 103°C in the TGA chamber to evaporate all the moisture, and were then heated 5°C/min. Tests were performed in an air medium.

Particle geometry evaluation

The aspect ratio was measured using a static 2-D microscopy method which employs a Morphologi G3 device produced by Malvern, UK. The test samples were prepared in a dry powder dispersion to ensure that all particles were separated from each other. 50–100 thousand particles were measured for each batch of material. For each particle the aspect ratio and surface area (converted to spherical equivalent volume) was measured. These data were used to calculate the volumetric average aspect ratio.

2.3. Manufacturing of composites

2.3.1. Compounding

Microfibers were dried prior to compounding in an SLW115 of POL-EKO, Poland – oven with forced

convection (approx. 16h at 103°C, moisture content <0.3 wt%). PP was processed without drying. The pre-dried microfibers were compounded with PP and MAH-g-PP granulates using a Laborextruder LSM30 manufactured by Leistritz, Germany (counter-rotating, tightly intermeshing twin-screw extruder, $L/D = 23$, $D = 34$ mm). The extruded strand was cooled in a water bath, and pelletized. The materials were compounded at temperatures ranging from 170 to 190°C, and at 40 rpm. The processing method ensured a good fiber distribution and an even fiber-to-matrix ratio, as is visible in the results of the density measurements and the small deviations in the mechanical properties for each manufactured type of composite material.

2.3.2. Injection molding

The standard test specimens manufactured according to EN ISO 178 were injection molded using an ALLROUNDER 270 S 350-100 produced by ARBURG, Germany, (clamping force 350 kN, screw diameter 25 mm, $L/D = 20$) and was provided by PRACHT GROUP Company. The molds adhere to EN ISO 294-1, type B. The barrel temperatures were 165–200°C from the feed zone to the nozzle. The injection pressure was limited to 800 bar at a constant injection speed of 20 cm^3/s, resulting in actual injection pressures ranging from 450 to 550 bar.

2.4. Characterization of composites

2.4.1. Density measurement

The density of the manufactured composites was measured using the Archimedes method at room temperature on a high accuracy scale type AS made by Radwag, Poland, according to EN ISO 1183. Samples were measured in ethanol medium. Weighing was repeated three times and the average of the measured values was calculated.

2.4.2. Odor measurement

The odor concentration was measured in accordance with EN ISO 13725 using a human nose as a sensor. The samples were put in an environment tempered to 70°C for 6h in order to increase the emission from samples, and to simulate the extreme conditions which may occur during exploitation in closed, non-ventilated chambers. The dynamic, half-automatic, pneumatic olfactometer type TO7, ECOMA, Germany was used for the purpose of measurements.

2.4.3. Flexural test

The static mechanical properties of the manufactured test specimens were measured in a flexural test according to EN ISO 178. The test was carried out on an universal testing machine type 3366, Instron, UK. The testing parameters were as follows: 1 mm/min for the estimation of the flexural E-modulus, and 2 mm/min for the estimation of the tensile strength. The following values represent the averaged results of the measurements performed on 10 samples for each type of composite material.

2.4.4. Notch impact strength

The impact strength was tested using the Izod method according to EN ISO 180/A on a Typ B5102 apparatus by Zwick, Germany. The A-notch was prepared on specimens using a dedicated notching machine. All composites were tested at room temperature 23°C and while subject to 50±10% relative humidity. The values presented comprise the averaged results for 10 tests carried out for each type of composite.

2.4.5. Heat deflection temperature

The heat deflection temperature (HDT) analyses were conducted on a Vicat-HDT analyzer manufactured by Donserv, Poland, according to EN ISO 75-1. The specimens were analyzed using a bending force of 1.8 MPa, a heating rate of 2°C/min, and the HDT was measured at a fixed elongation of 2 mm.

2.4.6. Brightness measurement

The injection molded samples were scanned using a standard Officejet Pro 8600, HP, USA. The allowance for coloration change was taken by subtraction of scanned white background. Coloration was averaged for 1 square centimeter using GIMP software. The results were presented after calculating the average of the RGB color model values.

3. Results and discussion

3.1. pH of microfibers

The pH of microfibers (Figure 2) after enzymatic treatment rose to neutral due to the buffering process. This can be advantageous for the long-term behavior of composites. It may also be favorable to reinforce polyester matrices that are prone to faster depolymerization in an acidic environment.

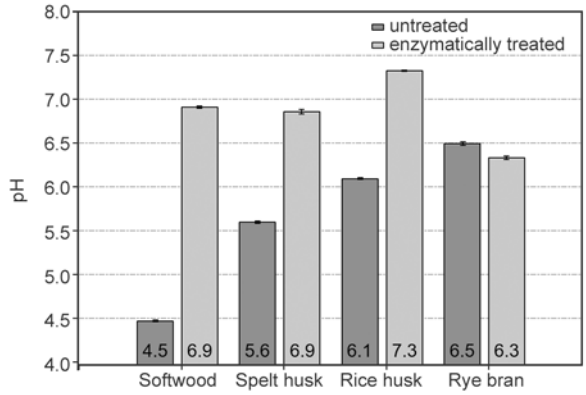

Figure 2. pH of microfibers before and after enzymatic treatment

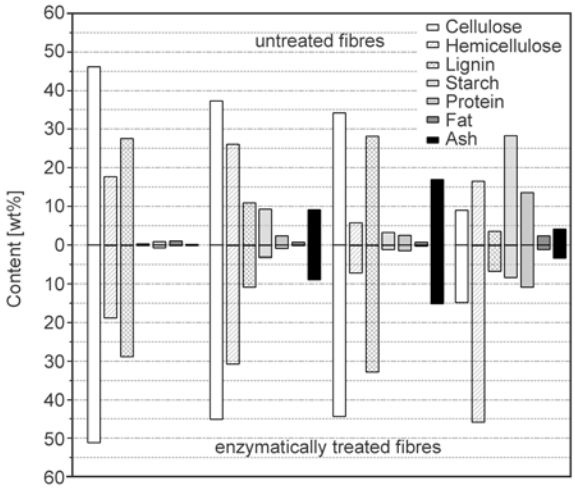

Figure 3. Chemical composition of microfibers before and after the enzymatic treatment

3.2. Chemical composition of microfibers

In natural fibers, crystalline cellulose micro-fibrils are embedded into an amorphous hemicellulose matrix encrusted with lignin that cross-links these polysaccharides. Therefore, the cellulose content and arrangement of the micro-fibrils is a decisive factor for the physical properties. Microfibers from grain husks have similar amounts of lignocellulosic compounds as standard softwood (Figure 3). Therefore, it is possible to assume that they may have similar reinforcing potential as standard wood fibers in WPC. Husks and, in particular, brans that cover the grains also consist of small amounts of starch, protein and fat. These components can also accumulate in form of particles on the surface of the grains during dehusking and dehulling processes that take place in the mills. In Figure 3 and Table 2, it is visible that the enzymatic treatment of the microfibers from husks and brans reduced the amount of starch approximately three-fold. The decrease of the protein content was most noticeable for microfibers made from spelt husks (60%), rice husks (35%) and rye brans (20%). The fats, which were already made up the smallest content in softwood microfibers, were almost completely removed. Significant reductions were obtained for microfibers from spelt husks (60%), rice husks (35%) and rye brans (45%). It can be also concluded that brans contain much lower amounts of cellulose than husks, which, in turn, makes them useless as a reinforcing material in composites. Consequently, they can only be applied as a filler.

3.3. Thermal gravimetric analysis

The weight loss of microfibers in correlation with temperature is illustrated in Figure 4. The diagram depicts the weight loss of up to 1 wt% of the initial value, which shows the beginning of the decomposition of microfibers. Figure 4 clearly verifies the achievement presented in Figure 3 and Table 2, namely that the enzymatic treatment considerably reduced the amounts of proteins and fats and, thus, improved the thermal stability of the microfibers. In the case of spelt and rice husks, the thermal stability was even higher than in the case of the reference softwood. In the case of all enzymatically treated microfibers, an initial weight loss of 1% was detected at approx. 20°C higher temperatures than for the untreated counterparts. This achievement is of significant value for thermoplastic composites pro-

Table 2. Chemical composition of microfibers [%]

	Softwood	Softwood after treatment	Spelt	Spelt after treatment	Rice	Rice after treatment	Rye	Rye after treatment
Cellulose	46.1	51.2	37.2	45.1	34.2	44.4	8.9	14.9
Hemicellulose	17.7	18.8	26.0	30.8	5.7	7.1	16.5	45.8
Lignin	27.6	28.9	10.8	10.8	28.1	32.8	3.5	6.7
Starch	0.2	0.1	9.2	3.2	3.2	1.2	28.3	8.3
Protein	0.8	0.8	2.3	0.9	2.5	1.6	13.5	10.9
Fat	0.9	0.2	0.6	0.2	0.6	0.4	2.3	1.3
Ash	0.1	0.1	9.1	8.9	16.9	15.2	4.0	3.3

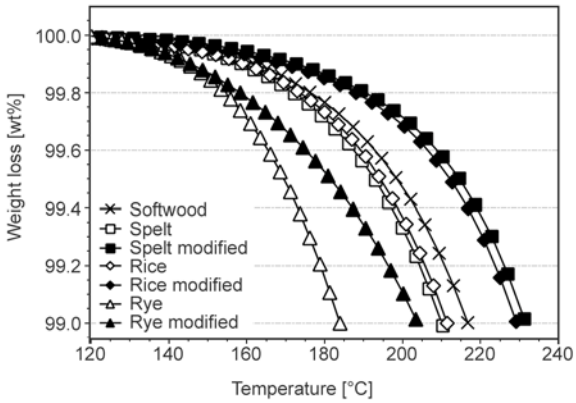

Figure 4. TGA curves of untreated and enzymatically treated microfibers

cessing, because the materials are subject to high pressures and temperatures which induce degradation of the low molecular weight compounds (proteins, fats) leading to deterioration of composite properties, odor emission and darkening of natural hue [30].

3.4. Aspect ratio of microfibers

Grain husks and brans were ground into particles sizes similar to those used for the reference softwood fibers, namely <600 μm. This particle size ensures that the melted composite material flows better during injection molding, and, therefore, enables injection molding of thin-walled parts. A 2D static analysis revealed that the reference material has a higher aspect ratio than microfibers from grain by-products (Figure 5). Higher aspect ratios provide better fiber-to-matrix stress transfer. This was verified in the results of flexural strength tests (Figure 8), where a correlation between a higher aspect ratio and flexural strength is evident. Microfibers from spelt husks had the highest aspect ratio of all used microfibers from grain husks. Microfibers from spelt husks had slightly higher aspect ratios, but since enzymes only work on the surface, to the higher aspect ratio can be attributed to the rinsing process instead of the enzymatic treatment itself, because it removed some of the finest particles.

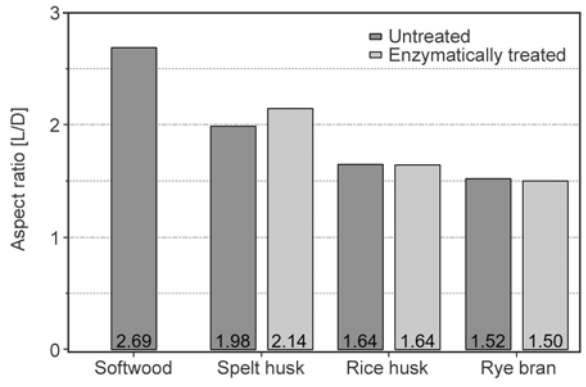

Figure 5. Aspect ratio of untreated and enzymatically treated microfibers

3.5. Bulk density of microfibers

The bulk density (Figure 6), which depends upon the fiber shape and chemical composition, confirmed that softwood have the most fibrous geometry among the investigated materials (Figure 5). In the case of softwood and spelt microfibers, it became clear that the rinsing phase of the enzymatic treatment may cause the finest particles to be flushed out, and, therefore, may contribute to increasing the portion of microfibers with a higher aspect ratio which remain after processing. Rice microfibers tend to be the heaviest due to their high silica content and lower aspect ratio. The microfibers from rye brans have a much lower bulk density after enzymatic treatment, which can be explained by the removal of starch and proteins. The remaining lignocellulosic particles are flake-shaped.

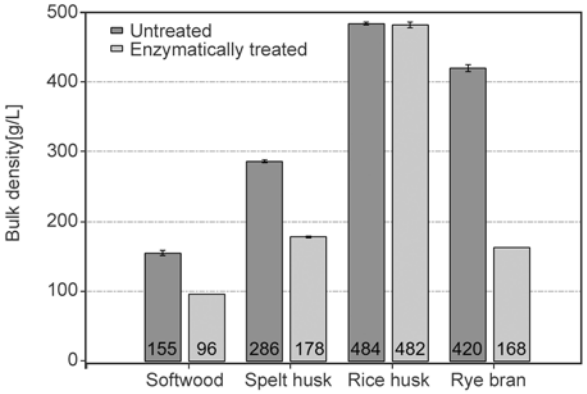

Figure 6. Bulk density of microfibers before and after enzymatic treatment

3.6. Density of biocomposites

Microfibers from grain by-products and softwood mainly consist of lignocellulose, thus, their density is similar. Accordingly, all manufactured composites reinforced with the above mentioned microfibers have shown density values in nearly the same range 1.05–1.07 g/cm^3. In contrast, the density of the PP matrix equals 0.91 g/cm^3.

The PP/GF density ranges between 1.03–1.22 g/cm^3 for standard fiber concentrations of 20–40 wt%. In the case of fiber concentrations of 40 wt%, this corresponds to a weight reduction of approx. 15% in

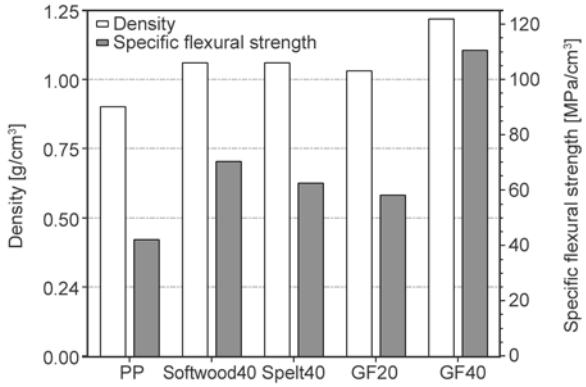

Figure 7. Density and specific flexural strengths of PP, WPC-40 wt% microfibers (Softwood and Spelt husk), PP-GF20 wt% and PP-GF40 wt% [31]

favor of lignocellulosic fibers. When comparing PP reinforced with 20 wt% GF to PP reinforced with 40 wt% of softwood, it is visible that an approx. 20% higher flexural strength of WPC can be achieved while obtaining a density which is only 3% higher. The light-weight potential of WPC composites and possibility of their complete energetic recyclability are essential features which account for their usage in automobiles and all applications where a reduction of mass is needed. Figure 7 illustrates densities and specific flexural strengths of native PP and its composites with 40 wt% softwood and spelt husk microfibers as well as 20 and 40wt% glass fibers (GF).

3.7. Mechanical properties

3.7.1. Flexural test

The Stress-strain curves presented in Figure 8 were measured in the flexural tests after averaging the 10 specimen curves for each material. The addition of softwood and spelt microfibers changed the material characteristics of the PP matrix from elastic to tough and less ductile. Reinforcing PP with microfibers leads to a visible decrease in strain. However, this is not exceedingly problematic, since a high ductility in not required in most engineering applications for composites. When comparing the curves of PP/Softwood and PP/Spelt, which have fibers with a similar chemical composition, it can be easily concluded that their geometry influences the mechanical properties of their composites. The higher aspect ratio of softwood fibers enabled an improved transfer of stresses from the matrix to the fiber, and, thus, higher strengths.

Figure 9 illustrates the flexural strength of PP and its biocomposites reinforced with microfibers. Flexural strength of PP can almost be doubled using standard softwood microfibers. The microfibers from spelt husks used in this study also resulted in an improvement of the flexural strength by approximately 74% for untreated and 58% for enzymatically treated ones. Both untreated and treated microfibers from rice husks increased the flexural strength by only 29%. The rye brans with their low cellulose content also did not contribute to a noticeable improvement. The results clearly show that a coupling between the non-polar matrix and polar fibers must be performed in order to obtain good reinforcement of PP using lignocellulosic fibers. Although this can be done using different methods and types of coupling agents, the use of MAH-g-PP waxes remains the most effective and simple. There is also an evident correlation between the volumetric average aspect ratio of the microfibers (Figure 5) and the flexural strengths of their biocomposites (Figure 8, 9).

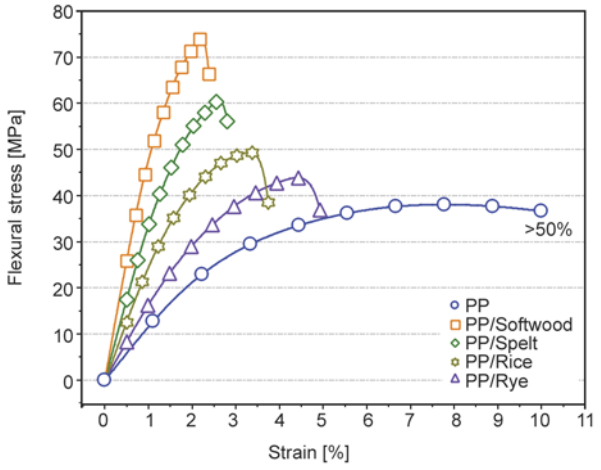

Figure 8. Flexural stress-strain curves of PP biocomposites reinforced with 40 wt% softwood and enzymatically treated microfibers from grain by-products that were compatibilized with MAH-g-PP

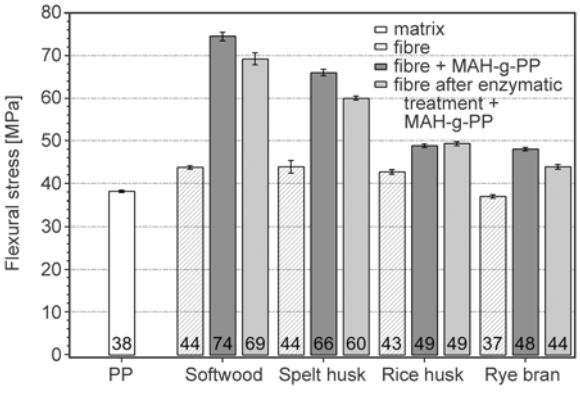

Figure 9. Flexural strength of PP biocomposites

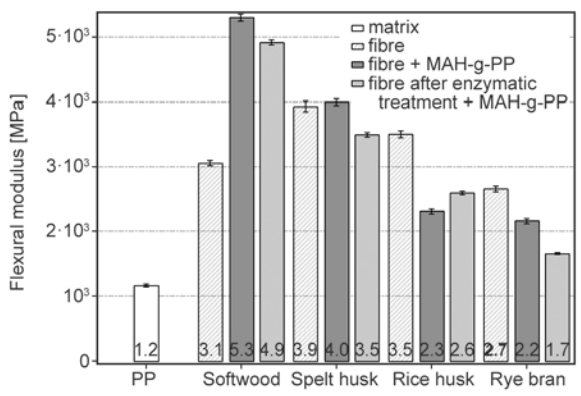

Figure 10. Flexural modulus of PP biocomposites

The flexural moduli of PP composites are illustrated in Figure 10. Here, the stiffness of the composites is not as strongly connected to the constraint of the matrix deformation. This depends on the stiffness of the fibers, their geometry and volume content in the composite, and, to some extent, on a good transfer of stresses from the matrix to the fiber. The obtained results clearly show that softwood microfibers help to improve the stiffness three-fold, and, without the application of MAH-g-PP, to almost five-fold the original value when coupling is applied. This parameter was increased for microfibers from spelt husks approximately four-fold. Here, no discernible difference was identified concerning the use of coupling and enzymatic treatment. Similarly, coupling and enzymatic treatment did not have any influence on the stiffness of composites filled with microfibers taken from rice husks and rye brans.

3.7.2. Notch impact strength

The crack propagation resistance evaluated in the notch Izod test, which is presented in Figure 11, was improved from 26 to 13% for composites reinforced

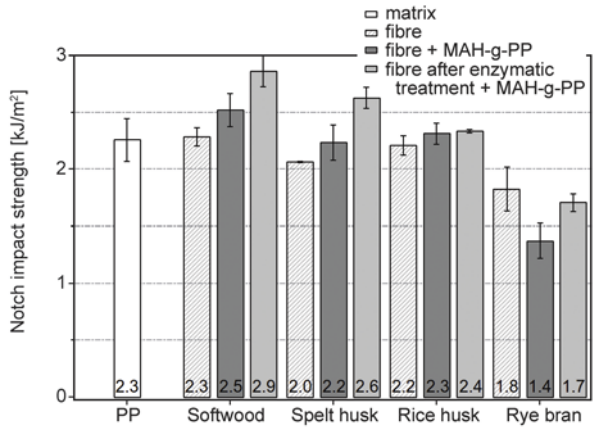

Figure 11. Notch impact strength of PP biocomposites in Izod test

with enzymatically treated softwood and spelt husk microfibers. It is a well-known fact that in order to increase the crack propagation resistance, fibers of an appropriate length must be used as reinforcement. The enzymatic treatment led to a slight improvement in impact strength compared to untreated microfibers. This might have been caused either by roughening the microfiber surface using xylanase, or by a higher aspect ratio of treated microfibers which resulted from flushing out finer particles during the rinsing stage of the enzymatic treatment process. In the case of microfibers with a low aspect ratio, they do not increase fracture surface area, and are not tough enough to absorb much energy, so the values of the impact strength can only be preserved or deteriorated.

3.8. Heat deflection temperature

Figure 12 shows that the creep under loading at higher temperatures can be significantly decreased. The heat deflection temperature was increased by the factor two for biocomposites with microfibers from spelt husks, and was only approximately 10°C lower than for the reference WPC material reinforced with softwood flour. Biocomposites reinforced with enzymatically treated microfibers exhibited slightly better performance. For microfibers from softwood a 12% increase was recorded, for those from spelt husks a 5% increase was achieved. Rice husks and rye brans, however, showed no improvement.

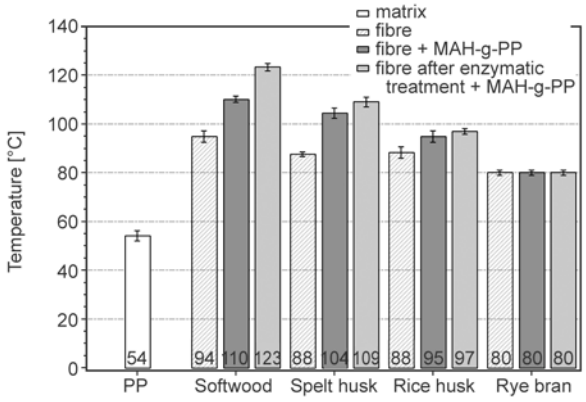

Figure 12. Heat deflection temperature of biocomposite materials

3.9. Olfactometry

The results of odor concentration measurements are presented in Figure 13. The most noticeable decline in odor emission for biocomposites with enzymati-

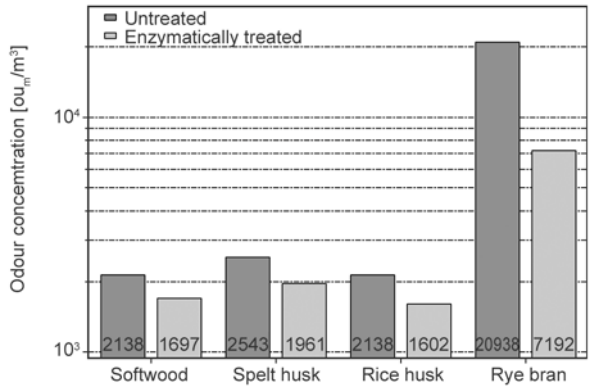

Figure 13. Odor concentration of biocomposites filled with untreated and enzymatically treated fibers

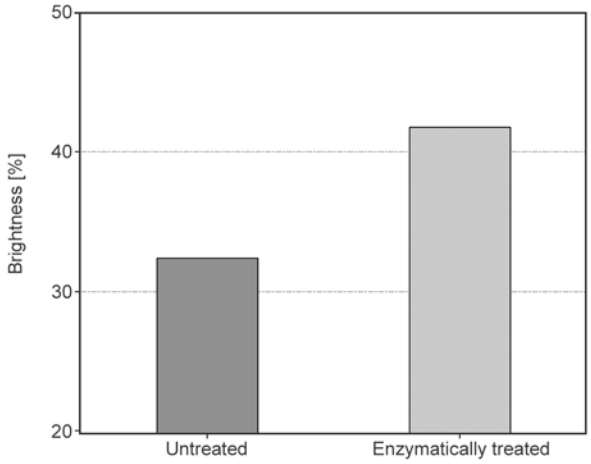

Figure 15. Average brightness of biocomposites filled with untreated and treated spelt husk fibers

cally treated fibers was reported for rye bran (more than two-fold); other microfibers also exhibited a decent decrease in odor emission. This confirmed the previously obtained results for the chemical composition investigation (Figure 3). Odor emission is noticeable at temperatures exceeding 50°C, and can be an important factor in automotive and furniture applications. Composites which exhibit unacceptably high emission rates despite otherwise good properties can be excluded from these kinds of applications. Thus, the enzymatic treatment of microfibers enables the application of grain husks instead of wood in WPC, making it possible to use them in the very same applications.

3.10. Brightness improvement

Treatment with enzymes led to significant increase in brightness of the microfibers. This, in turn, increased the brightness of injection molded parts. This can be important in the case of a lower pigment demand for in melt colorizing of final product, which helps to lower prices of end-product. The best results presented in Figure 14 and Figure 15 were obtained for microfibers from spelt husks. The removal of proteins and fats from the surface of microfibers (which decompose during plastic processing) led to an increase of brightness by approximately 10%.

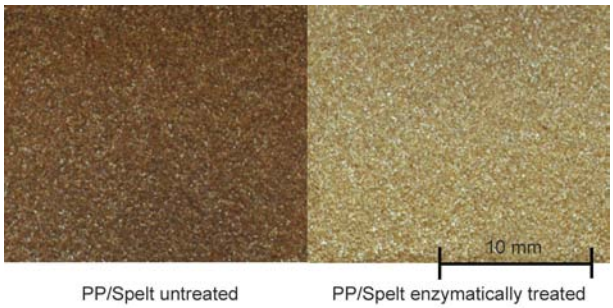

Figure 14. Brightness of biocomposites filled with untreated and treated spelt husk fibers

4. Conclusions

This research study has proven that grain by-products are a valuable source of lignocellulosic materials for microfiber processing. These can, in turn, be a substitute for wood flour in the production of thermoplastic biocomposites. One can conclude that only husks and hulls which contain lower amounts of fat, protein and starch are a good source for microfibers (Figure 3, 8–12). It has been shown that brans, which contain rests of grains, have more of these compounds, and, consequently, their biocomposites have inferior properties. In order to further improve their properties, an environmental friendly and selective processing with enzymes was proposed. Enzymatic treatment removed considerable amounts of starch, proteins and fats (Figure 3). Thus, the thermal stability of treated microfibers increased significantly (Figure 4). This, in turn, increased the brightness of the microfibers (Figure 14, 15), while simultaneously also leading to a decrease in odor in the composites (Figure 13). These features make the application of products made from biocomposites reinforced with microfibers from grain husks possible in household and automotive industries. The other aspect that shall be taken into account when using microfibers from grain by-products as reinforcement in WPC is their variable content of minerals, which is different depending on spices and varieties. In order to avoid faster wear of the processing equipment, namely the screws and barrels, only materials with lower mineral contents shall be selected (Figure 3). Therefore,

the appropriate selection of husks and their proper processing to fibrous material, as well as their additional enzymatic treatment can produce valuable microfibers that may be used as an effective substitution of wood flour in WPC. This, in turn, is a solution for the shortage of precious wood. The obtained results show improvement in terms of mechanical properties (flexural and impact strengths) to previous researches concerning PP reinforced with microfibers from grain by-products [29].

In sum, the enzymatic treatment process led to the following changes in microfibers from grain husks and brans:

- a three-fold decrease of the starch content, 20–60% decrease of the protein content and 35–60% decrease of content of fat,
- an increase of the thermal stability by about 20°C at 1 wt% loss,
- a 13–26% improvement of the notched impact strength for their biocomposites,
- a 5–12% increase of the heat deflection temperature for their biocomposites,
- a more than two-fold decrease of the odor emission for rye brans,
- a 10% increase of the brightness in biocomposites reinforced with microfibers from spelt husks.

Acknowledgements

The authors would like to express their appreciation to Novozymes, Univar Poland, Clariant Masterbatches, HSH Chemie Poland, JELU-WERK and the Institut für Lebensmittel- und Umweltforschung e. V. for supplying the enzymes, additives and reinforcing fibers. The authors would also like to thank Prachtgroup for the Arburg Allrounder 270 S 350–100 injection molding machine. This research study was carried out in the context of the project 'Enzymatic Treatment of Natural Microfibers Applied in Biocomposites' – grant no. 503-06-010-2617/4 funded by the National Science Center of Poland.

References

[1] Faruk O., Bledzki A. K., Fink H-P., Sain M.: Biocomposites reinforced with natural fibers: 2000–2010. Progress in Polymer Science, **37**, 1552–1596 (2012). DOI: 10.1016/j.progpolymsci.2012.04.003

[2] Bledzki A. K., Sperber V., Theis S., Gassan J., Nishibori S.: Holzgefüllte Thermoplasteals Alternative für Naturholz. Gummi Fasern Kunststoffe, **52**, 294–296 (1999).

[3] Reußmann T., Mieck P., Grützner R-E., Bayer R.: Recycling von Naturfaserverstärktem Polypropylen. Kunststoffe, **82**, 80–84 (1999).

[4] Buongiorno J., Raunikar R., Zhu S.: Consequences of increasing bioenergy demand on wood and forests: An application of the global forest products model. Journal of Forest Economics, **17**, 214–229 (2011). DOI: 10.1016/j.jfe.2011.02.008

[5] Bledzki A. K., Gassan J.: Composites reinforced with cellulose based fibres. Progress in Polymer Science, **24**, 221–274 (1999). DOI: 10.1016/S0079-6700(98)00018-5

[6] Faruk O., Bledzki A.: Wood plastic composite: Present and future. 'Wiley Encyclopaedia of Composites' (eds.: Nicolais L., Borzacchiello A., Lee S. M.) Wiley, vol 5, 3212–3232 (2012). DOI: 10.1002/9781118097298.weoc264

[7] Steglitz H., Oswald P.: WPC market analyses report. Krauss Maffei, München (2011).

[8] Food and Agricultural Organization of the United Nations, Online database. http://faostat3.fao.org (2014).

[9] Oplinger E. S., Oelke E. A., Kaminski A. R., Kelling K. A., Doll J. D., Durgan B. R., Schuler R. T.: Alternative field crops manual – Spelt. University of Wisconsin, Wisconsin (1990).

[10] Neeson R.: Organic spelt production. Climate and water research – NSW Government industry and Investment (2011).

[11] Kumar A., Mohanta K., Kumar D., Parkash O.: Properties and industrial applications of rice husk: A review. International Journal of Emerging Technology and Advanced Engineering, **2**, 86–90 (2012).

[12] Prasara J.: Comparative life cycle assessment of rice husk utilization in Thailand. PhD Thesis. RMIT University, Melbourne (2009).

[13] Sibakov J., Lehtinen P., Poutanen K.: Cereal brans as dietary fibre ingredients. 'Fibre-rich and wholegrain foods' (eds.: J. A. Delcour, K. Poutanen), Woodhead, Cambridge, 170–192 (2013). DOI: 10.1533/9780857095787.2.170

[14] Valde Coerts T., Ossendorp B. C.: Fenitrothion. '2004 Joint FAO/WHO Meeting on Pesticides Residues. Rome, Italy', 173–174 (2005).

[15] Niir Board: Products from waste. National Institute of Industrial Research, New Delhi, 249–256 (2000).

[16] Tabak J.: Biofuels. Facts on File Inc., New York (2009).

[17] Narra S.: Bioenergy production: Special emphasis on rice husks usage in India. 'Implementing Environmental and Resource Management' (eds.: Schmidt M., Onyango V., Palekhov D.) Springer-Verlag, Berlin-Heidelberg, 15–22 (2011). DOI: 10.1007/978-3-540-77568-3

[18] Novozymes: Cellulosic ethanol – Novozymes Cellic® HTec3 (application sheet). (2012).

[19] Merino S. T., Cherry J.: Progress and challenges in enzyme development for biomass utilization. Advances in Biochemical Engineering/Biotechnology, **108**, 95–120 (2007). DOI: 10.1007/10_2007_066

[20] Teter S.: A closer look at the enzymes that deconstruct biomass. Novozymes, Bagsvaerd (2009).
[21] Bledzki A. K., Mamun A. A., Bonnia N. N., Ahmad S.: Basic properties of grain by-products and their viability in polypropylene composites. Industrial Crops and Products, **37**, 427–434 (2012).
DOI: 10.1016/j.indcrop.2011.05.010
[22] Bledzki A. K., Mamun A. A., Volk J.: Physical, chemical and surface properties of wheat husk, rye husk and soft wood and their polypropylene composites. Composites Part A: Applied Science and Manufacturing, **41**, 480–488 (2010).
DOI: 10.1016/j.compositesa.2009.12.004
[23] Bledzki A. K., Mamun A. A., Volk J.: Barley husk and coconut shell reinforced polypropylene composites: The effect of fibre physical, chemical and surface properties. Composites Science and Technology, **70**, 840–846 (2010).
DOI: 10.1016/j.compscitech.2010.01.022
[24] Bledzki A. K., Mamun A. A., Jaszkiewicz A., Erdmann K.: Polypropylene composites with enzyme modified abaca fibre. Composites Science and Technology, **70**, 854–860 (2010).
DOI: 10.1016/j.compscitech.2010.02.003
[25] Sharma H. S. S., Whiteside L., Kernaghan K.: Enzymatic treatment of flax fibre at the roving stage for production of wet-spun yarn. Enzyme and Microbial Technology, **37**, 386–394 (2005).
DOI: 10.1016/j.enzmictec.2004.10.007
[26] Nierstrasz V., Warmoeskeren M.: Process engineering and industrial enzyme applications. in 'Textile processing with enzymes' (eds.: Cavaco-Paulo A., Gübitz G. M.) Woodhead, Cambridge, 123–131 (2003).
[27] Gašparovič L., Koreňová Z., Jelemenský L.: Kinetic study of wood chips decomposition by TGA. Chemical Papers, **64**, 174–181 (2010).
DOI: 10.2478/s11696-009-0109-4
[28] Damhus T., Kaasgaard S., Lundquist H., Olsen H. S.: Enzymes at work. Novozymes, Bagsvaerd (2008).
[29] Mamun A. A., Bledzki A. K.: Micro fibre reinforced PLA and PP composites: Enzyme modification, mechanical and thermal properties. Composites Science and Technology, **78**, 10–17 (2013).
DOI: 10.1016/j.compscitech.2013.01.013
[30] Gómez-Martínez D., Barneto A. G., Martínez I., Partal P.: Modelling of pyrolysis and combustion of gluten–glycerol-based bioplastics. Bioresource Technology, **102**, 6246–6253 (2011).
DOI: 10.1016/j.biortech.2011.02.074
[31] Albis Plastic GmbH datasheets: Altech PP-H A 2040-159 GF CP; and Altech PP-H A 2020 100 GF20, Glass reinforced PP (2014).

eXPRESS Polymer Letters Vol.8, No.10 (2014) 779–789
Available online at www.expresspolymlett.com
DOI: 10.3144/expresspolymlett.2014.80

Preparation and properties of multi-branched poly(D-lactide) derived from polyglycidol and its stereocomplex blends

A. Petchsuk[1], *S. Buchatip*[1], *W. Supmak*[1], *M. Opaprakasit*[2], *P. Opaprakasit*[3*]

[1]National Metal and Materials Technology Center, Thailand Science Park, 12120 Pathum Thani, Thailand
[2]Center of Excellence on Petrochemical and Materials Technology, Department of Materials Science, Faculty of Science, Chulalongkorn University, 10330 Bangkok, Thailand
[3]School of Bio-Chemical Engineering and Technology, Sirindhorn International Institute of Technology (SIIT), Thammasat University, 12121 Pathum Thani, Thailand

Received 10 March 2014; accepted in revised form 2 June 2014

Abstract. Multi-branched poly(D-lactide)s (*mb*PDLAs) with various structures are synthesized *via* ring-opening polymerization by using polyglycidol (PG) macro-initiators. Their chemical structures and thermal properties are controlled by adjusting feed ratios of D-lactide (DLA) and PG. The materials are blended with commercial linear poly(L-lactide) (*l*-PLLA) to form a stereocomplex structure. Effects of *mb*PDLAs structures and *l*-PLLA/*mb*PDLA ratios on the blends' thermal, mechanical, and rheological properties are evaluated. Mechanical properties of the stereocomplex blends, especially elongation at break and toughness, are dependent on the blend compositions, in which a 90:10 ratio exhibits the most desirable properties. The material also exhibits the lowest complex viscosity, which provides easy processing conditions. This is achieved by the incorporation of copolymers with multi-branched structures and an ability to form a much stronger stereocomplex structure.

Keywords: *polymer blends and alloys, polylactide, stereocomplex, multi-branched, polyglycidol*

1. Introduction

Polylactide or polylactic acid (PLA) is a degradable polymer that is widely used in many applications, especially packaging, biomedical, agricultural, and environmental fields, due to its biodegradability, biocompatibility, and its renewable monomer resources. Despite these excellent characteristics, its thermal stability, durability, impact strength, and heat deformation temperature are significantly low, which limit its use in certain applications [1, 2]. Various physical and chemical modifications have been employed to improve these properties, *e.g.* copolymerization with other monomers [3–11], or blending with other (co)polymers [5, 9, 10, 12–15].

Stereocomplexation is a promising technique to enhance PLA properties, by utilizing the strong interaction between its helical stereo-conformations, *i.e.*, poly(L-lactide) (PLLA) and poly(D-lactide) (PDLA). This PLLA/PDLA stereocomplex exhibits a unique crystalline structure and morphology [2, 10, 12, 16], which has a melting temperature (T_m) 50°C higher than its homopolymer counterparts. The stereocomplex structure has high potential to improve heat resistivity and mechanical properties (tensile strength, Young's modulus, and elongation at break) of the materials [17]. The structure can be obtained by either solution or melt blending methods. Recently, supercritical fluids

*Corresponding author, e-mail: pakorn@siit.tu.ac.th

[18], microwave [19], and nano-processing techniques [20–22] have been employed in the stereocomplex formation. Preparation, structures, properties, and applications of this structure have been extensively studied [17, 23–27]. Formation of stereocomplex structure is usually accompanied by homo-crystallization, predominantly when high molecular weight PLAs are employed [2, 10]. A complete stereocomplexation, without homo-crystallite, is obtained from an equimolar mixture of sufficiently-low molecular weight PLLA and PDLA.

Stereocomplexation is also observed in block copolymers of L-lactide (LLA) and D-lactide (DLA) during polymerization, or during solid state polymerization of small-sized PLLA and PDLA [24, 28–30]. Stereoblock PLA copolymers have been used as compatibilizers in an enhancement of stereocomplexation efficiency, by suppressing the homo-crystallite formation of large-sized PLLA and PDLA [24]. However, these stereoblock copolymers cannot be processed into fibers or films, because of their relatively low molecular weight. Recently, a preparation of high-molecular weight stereoblock copolymers by employing non-equimolar LLA/DLA ratios was reported [31]. A complete stereocomplex without homo-crystallite was obtained when PDLA compositions of at least 15% was employed. An effective but rather expensive process of radiation-induced crosslinking was also employed to enhance the stereocomplex formation and to lower processing temperatures of its low molecular weight blends [32]. Although various structural formation mechanisms and analyses of PLA stereocomplex have been proposed, insights into the improvement of their toughness and rheological properties have not been presented.

Inclusion of branch-structured polymers into brittle plastics leads to improvement in their mechanical properties, especially toughness. Multi-branched polymers possess lower chain entanglements, lower solution and melt viscosity, but higher thermal stability, compared to their linear-structured counterparts. Other unique characteristics, *i.e.*, their globular shape, and their large number of functional groups within a molecule, make these polymers suitable for various applications. The number and types of functional groups on these polymers can be modified to control their properties for specific applications [33]. Recently, multi-branched PLAs have been developed, and their possible applications have been assessed [34–38].

In this work, multi-branched poly(D-lactide)s (*mb*PDLAs), with different structures and properties, are prepared by employing polyglycidol (PG) as a macro-initiator. Depending on *mb*PDLAs structures, the stereocomplex can be achieved by blending with linear poly(L-lactide) (*l*-PLLA). The major advantages of these stereocomplex mixtures derived from the branched constituents are an enhancement in the blend's mechanical properties and a decrease in melt viscosity. The resulting blends have high potential for use as high performance materials with easy fabrication processes.

2. Experimental

2.1. Materials

l-PLLA ($\overline{M}_w$ = 178 000 g/mol) and D-lactide monomer (DLA) were supplied by PURAC (Netherlands). Tin(II) octoate catalyst, $Sn(Oct)_2$, was purchased from Wako (Japan). Glycidol was purchased from Aldrich (USA) and used as received. Ethyl acetate, chloroform, ethanol, and toluene solvents were purchased from Lab Scan (Thailand).

2.2. Synthesis of *mb*PDLAs

Polyglycidol (PG) is employed as a macro-initiator in the synthesis of *mb*PDLAs. PG was prepared by a ring-opening polymerization of glycidol under an inert atmosphere, using $Sn(Oct)_2$ catalyst at a polymerization temperature and time of 110°C and 3 h. Effect of catalyst contents on structures of PG was examined by varying the contents from 0.25–1.0 mol%. *mb*PDLAs were then synthesized *via* a ring-opening polymerization of DLA in a presence of $Sn(Oct)_2$ catalyst and PG macro-initiator, under an inert atmosphere at 120°C for 24 h [39, 40]. The products were purified by dissolving in chloroform and precipitating in an ethanol/hexane mixture, and then dried under vacuum at 50°C for 24 h. The DLA/PG molar ratios were varied from 5/1 to 50/1, to produce *mb*PDLAs with different structures. The resulting copolymers were coded according to the feed DLA/PG ratios, *e.g.*, *mb*PDLA051 was synthesized from a 5/1 ratio.

2.3. Stereocomplexation of *l*-PLLA and *mb*PDLAs

Stereocomplex blends of *l*-PLLA/*mb*PDLA were prepared by mixing THF solutions of the constituents at various weight ratios, *i.e.*, 90/10, 80/20, 70/30 and 50/50. The mixtures were then casted on a glass surface, in which the solvent was removed by evaporation in a vacuum oven at room temperature for 48 h. The resulting films were cut into rectangular shape with 50 mm gauge length and 15 mm width, according to ASTM D882, for mechanical tests.

2.4. Characterizations

Average molecular weights ($\overline{M}_n$, $\overline{M}_w$) and polydispersity (PDI) of *mb*PDLAs were measured using a Gel Permeation Chromatography (GPC), Waters e2695 with dual detectors: Viscotek Model 3580 Reflective Index detector and Model 270 differential viscometer detector comparative to mono-disperse polystyrene standards (4490–1 112 000 g/mol). The measurement was performed on PL gel 10 micron mixed B2 columns (Polymer Laboratories), at 35°C, using tetrahydrofuran eluent with a flow rate of 1.0 mL/min. The glass transition (T_g) and melting (T_m) temperatures of the copolymers were determined by Differential Scanning Calorimeter (DSC) on a DSC822e Mettler Toledo. The samples were scanned twice from –60 to 250°C with a heating and cooling rate of 20.0°C/min. Chemical structures of *mb*PDLAs were examined using an AVENCE^{III} 500 MHz digital Nuclear Magnetic Resonance spectrometer (AV-500, Bruker Biospin;), using $CDCl_3$ (for *mb*PDLAs) and D_2O (for PG) solvents.

Tensile properties of blend samples were measured at room temperature on a universal testing machine (Instron model 55R4502, Instron Corp., USA) with a 100 N load cell and a crosshead speed of 50 mm/min, The specimens were prepared as rectangular specimens (prepared by solvent casting) with 50 mm gauge length and 15 mm width, according to ASTM D882. Each reported value is an average of measurements carried out on at least 4 specimens. Rheological properties, *i.e.*, elastic modulus (G'), loss modulus (G''), and complex viscosity (η*), were measured on a strain-controlled rheometer (ARES, TA Inc., New Castle, USA) with a torque transducer capable of measurement over the range of 2–200 g·cm. Disc samples with a diameter of 25 mm and 1 mm thickness were prepared by hot-pressing. The strain amplitude for dynamic measurements was fixed at 5%. The measurements were conducted in a temperature range of 190–250°C, with a heating rate of 10°C/min at a frequency of 1 rad/s. Complex viscosity (η*) changes of the melts as a function of shear rate were conducted at a constant temperature of 230°C.

3. Results and discussion

3.1. Chemical structures and properties of *mb*PDLAs

PG macro-initiators are synthesized by varying the catalyst contents from 0.25–1.0 wt%. Figure 1a shows ^{1}H NMR spectrum of a PG sample, whose hydroxyl number is 340 mg KOH/g sample (according to standard test method D4274-05, test method C). Complex signals, appeared in the range of 3.3–3.8 ppm, correspond to methylene and methine protons, while a resonance located at 4.7 ppm is assigned to hydroxyl terminals. The integral ratio of methylene and methine/hydroxyl of 9/1 is observed. Detailed information on chemical structure of PG can be derived from ^{13}C NMR Inverse Gated spectra, in which complicated patterns of perfect dentritic (*D*), linear (*L*), and terminal (*T*) units can be identified. The assignments have been applied to

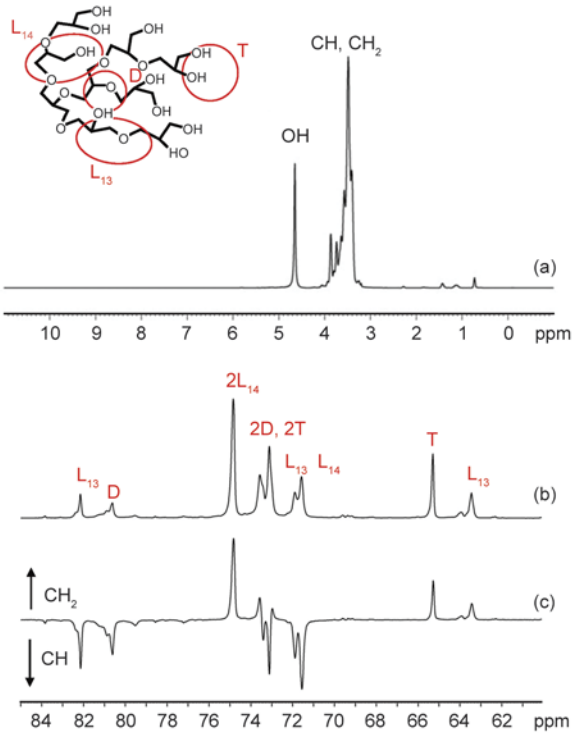

Figure 1. ^{1}H NMR (a), ^{13}C NMR (b), and ^{13}C NMR DEPT (c) spectra of PG synthesized from tin catalyst

the spectra of PG synthesized from anionic polymerization [41–44]. Similar spectral characteristics are observed in this study, in which a tin catalyst is employed, as shown in a ^{13}C NMR and a distortionless enhancement by polarization transfer (DEPT) spectra in Figure 1b and 1c, respectively. This reflects a formation of similar products. The advantage of this synthesis route is, however, its one-step process, in which branching structures of PG products can be manipulated by varying the catalyst contents.

GPC chromatograms of PG synthesized from various catalyst contents are compared in Figure 2. At 1.0 mol%, a mono-modal size distribution is observed with a molecular weight at peak (M_p) of 2100 g/mol. As the catalyst content decreases to 0.5 and 0.25 mol%, the results show bi-modal distribution with similar M_{p1} of 2000 g/mol, and a variation in M_{p2} from 11 500 to 24 800 g/mol, respectively. The relative intensity of the high-molecular weight fraction increases with the decrease in the catalyst contents. Although the polydispersity value (~3.4) is significantly high, compared to that obtained from anionic polymerization [41–44], this synthesis route is considered as an alternative approach when structural perfection may not be a strict requirement for most applications.

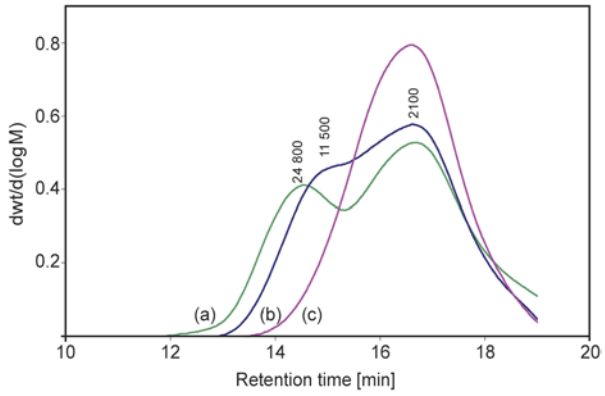

Figure 2. GPC chromatograms of PG synthesized at different catalyst contents: 0.25 (a), 0.5 (b), and 1.0 mol% (c)

The relatively larger-sized PG prepared from a catalyst content of 0.25 mol% is employed as a macroinitiator in the synthesis of *mb*PDLAs. ^1H NMR spectra of the resulting copolymers obtained from various PG/DLA ratios are shown in Figure 3. Characteristic signals of PG appear at 3.5–3.7 ppm (d, e), corresponding to methylene protons (–C**H**$_2$–CH–O) and methine proton (–CH$_2$–C**H**–O). The signal at 5.1–5.2 ppm (b) is assigned to methine [O=C–C**H**(CH$_3$)–O–] of lactate units. This confirms the presence of PDLA chains on the PG core. The integral ratios of the signals at 3.5–3.7 and 5.1–5.2 ppm reflect the PG/PDLA compositions in the copolymer chains. Average DLA length/ branch (DLA_n) is calculated from the integral ratio of $^bH/^cH$. Results on chain compositions and molecular weight of the copolymers are summarized in Table 1. Copolymers with $\overline{M}_w$ ranging from 35 000–80 000 g/mol are obtained. The chain compositions are significantly similar to the corresponding feed ratios, reflecting a high incorporation efficiency of lactate units. DLA compositions and molecular weight of the copolymers increase with an increase of the DLA/PG feed contents. DLA_n value increases with an increase in the feed ratios from 5/1 to 20/1. Although *mb*PDLA201 and *mb*PDLA501 show

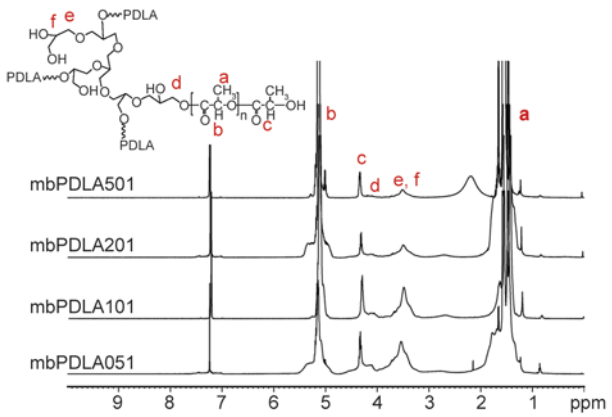

Figure 3. ^1H NMR spectra and signal assignments of *mb*PDLAs

Table 1. Synthesis conditions and properties of *mb*PDLAs

Samples	DLA/PG compositions		DLA_n	$\overline{M}_n$[b] [g/mol]	$\overline{M}_w$[b] [g/mol]	PDI
	in feed	in chain[a]				
l-PLLA	–	–	–	88 800	178 100	2.01
*mb*PDLA051	5/1	83/17	4	6 700	35 200	5.25
*mb*PDLA101	10/1	92/8	7	20 600	48 900	2.37
*mb*PDLA201	20/1	96/4	17	19 100	64 400	3.38
*mb*PDLA501	50/1	98/2	17	23 000	81 500	3.54

[a]^1H NMR, [b]GPC, DLA_n = average DLA length/branch, PDI = polydispersity index

Table 2. Thermal properties of *mb*PDLAs derived from DSC thermograms

Samples	1st scan			2nd scan		
	T_g [°C]	T_m [°C]	ΔH_m [J/g]	T_g [°C]	T_m [°C]	ΔH_m [J/g]
l-PLLA	–	179	44.7	58	174	45.4
*mb*PDLA051	18	–	–	29	–	–
*mb*PDLA101	36	90	11.9	37	–	–
*mb*PDLA201	50	125	32.5	49	–	–
*mb*PDLA501	46	140	36.2	44	135	14.1

similar DLAn values, a difference in their average molecular weights reflects different numbers of lactate branches per molecule. This, in turn, imposes strong effect on physical and mechanical properties of the copolymers, discussed later.

DSC thermograms of *mb*PDLAs are compared with *l*-PLLA in Figure 4. Their thermal properties derived from 1st heating scans are summarized in Table 2. *l*-PLLA exhibits cold crystallization in both of its 1st and 2nd heating scans, indicating that its crystallization is not complete at the applied DSC cooling rate, due to its long-chain structure. From the 1st heating cycles, all *mb*PDLAs exhibit melting characteristics without cold crystallization. This is likely because these samples are prepared from a solvent-casting technique, which allows high freedom of crystallization. T_m's of *mb*PDLAs shift toward higher temperatures, whose heat of fusion values (ΔH_m) also increases, with an increase in DLA block lengths and DLA contents of the chains. This indicates a strong influence of DLA sequences on crystalline structure of the copolymers.

In the 2nd heating scans, however, cold crystallization and melting characteristics of *mb*PDLAs are not observed, except *mb*PDLA501. This reflects the influences of the samples structures and their thermal history, in which the multi-branched structure retards crystallizability of molten *mb*PDLAs during DSC cooling and re-heating cycles. For the largest copolymer in the series (*mb*PDLA501), however, its sufficiently-long DLA sequences enable formation of crystalline domains upon re-heating. The results from both heating scans show that the copolymers have lower T_g than *l*-PLLA, due to their shorter DLA sequences. The T_g values increase with the copolymer's molecular weights.

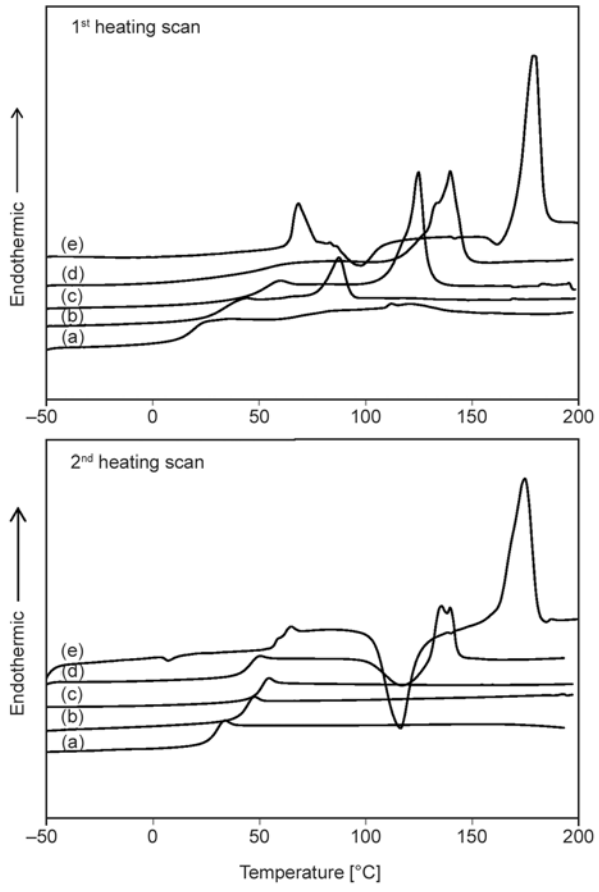

Figure 4. DSC thermograms of *mb*PDLAs synthesized at various DLA/PG molar ratios: (a) 5/1, (b) 10/1, (c) 20/1, (d) 50/1, and (e) *l*-PLLA

3.2. Thermal properties of *l*-PLLA/*mb*PDLA stereocomplex blends

Effects of *mb*PDLA structures and the blend compositions on properties of *l*-PLLA/*mb*PDLA stereocomplex are investigated. Figure 5 shows DSC thermograms (2nd heating scan) of blends (prepared at a 90/10 ratio) consisting of various *mb*PDLAs. This non-equimolar blend composition is employed to investigate interplay between crystallization behaviors of homo-crystallite and stereocomplex. Ther-

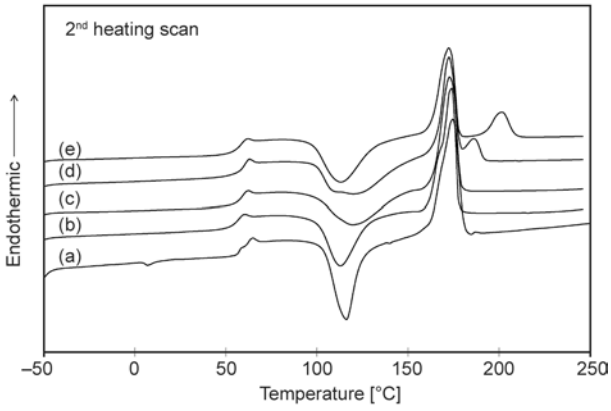

Figure 5. DSC thermograms of (a) *l*-PLLA and *l*-PLLA/*mb*PDLA501 stereocomplex blends (prepared at a 90/10 blend ratio) containing: (b) *mb*PDLA051, (c) *mbP*DLA101, (d) *mb*PDLA201, and (e) *mb*PDLA501

Table 3. Thermal properties (2nd heating scan) of *l*-PLLA and *l*-PLLA/*mb*PDLA501 stereocomplex blends containing various *mb*PDLAs at a 90/10 blend ratio.

Blend component	T_g [°C]	T_c [°C]	ΔH_c [J/g]	Homo-crystallite		Stereocomplex	
				T_m [°C]	ΔH_m [J/g]	T_m [°C]	ΔH_m [J/g]
l-PLLA	58	117	45.3	174	45.4	–	–
l-PLLA/*mb*PDLA051	55	113	35.3	174	39.4	–	–
l-PLLA/*mb*PDLA101	58	120	33.2	173	40.1	–	–
l-PLLA/*mb*PDLA201	59	120	36.2	172	34.6	186	6.6
l-PLLA/*mb*PDLA501	56	113	34.5	173	33.2	202	10.2

mal properties of all blends are summarized in Table 3. The glass transition and homo-crystallite melting characteristics are clearly observed in all samples, which remain unchanged regardless of size of *mb*PDLA components. Blends containing *mb*PDLAs with $\overline{M}_w$ higher than 60 000 g/mol, *i.e.*, *mb*PDLA201 and *mb*PDLA501, show an additional T_m of the stereocomplex structure at 186 and 210°C, respectively. This indicates that a critical length of DLA sequences is required to form the stereocomplex structure, whose structural strength is dependent on the copolymer sizes.

Cold crystallization is observed in *l*-PLLA and all blends. The heat of cold crystallization (ΔH_c) value of *l*-PLLA is similar to ΔH_m of its homo-crystallite, indicating an absence of melt crystallization, *i.e.*, the crystalline domains are mainly formed during the reheating process. The corresponding values for blends of small-sized *mb*PDLAs are lower than ΔH_m, despite the absence of the stereocomplex melting peak. This reflects that the DLA short sequences act as nucleating species promoting the formation of homo-crystallite during melt crystallization [45, 46]. In contrast, ΔH_c values of the blends containing large-sized *mb*PDLAs, which show stereocomplex peak, are slightly higher than ΔH_m of their homo-crystallite. This is likely because stereocomplex formation occurs rapidly during the melt crystallization, but the crystallization is not complete at the applied cooling rate as the blends contain high *l*-PLLA content. When the sample is reheated higher than T_g, chain rearrangements take place, resulting in the formation of homo-crystallites and additional stereocomplex structures.

In blends containing large-sized *mb*PDLAs, ΔH_m values of their stereocomplex endotherm increase with molecular weight of the *mb*PDLA component, whereas the corresponding values of the homo-crystallites significantly decrease. This is likely due to the suppression of homo-crystallization by the formation of the stronger stereocomplex structure. For blends consisting of small-sized *mb*PDLAs, however, ΔH_m remains constant as the suppression effect from the stereocomplex is negligible. All samples show a single T_g ranging from 55–59°C, indicating miscible blends.

Effect of blend compositions on thermal properties of the stereocomplex blends is examined. DSC thermograms (2nd heating scan) of blends containing *mb*PDLA501 at various blend ratios are compared in Figure 6. Cold crystallization is clearly observed in *l*-PLLA and *l*-PLLA-rich blends, along with the melting characteristic of homo-crystallite and stereocomplex. This reflects that the stereocomplex structure is formed at a much faster rate during the DSC cooling cycle, which retards formation of homo-crystallite in *l*-PLLA-rich blends [12]. In contrast, a 50:50 blend shows only the stereocomplex melting peak, with no cold crystallization, reflecting that no homo-crystallite domains are formed for an equimolar blend. Thermal properties of the blends are summarized in Table 4. T_m of homo-crystallite shifts to lower temperatures, whereas that of the stereocomplex slightly shifts toward higher temperatures, with

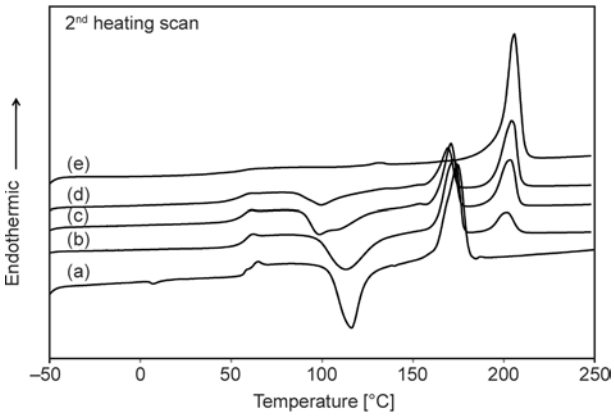

Figure 6. DSC thermograms (2nd heating scan) of (a) *l*-PLLA, and *l*-PLLA/*mb*-PDLA501 stereocomplex blends at various compositions: (b) 90/10, (c) 80/20, (d) 70/30 and (e) 50/50

Table 4. Thermal properties of *l*-PLLA/*mb*PDLA501 stereocomplex at various blend compositions

Blend ratios	T_g [°C]	T_c [°C]	ΔH_c [J/g]	Homo-crystallite		Stereocomplex	
				T_m [°C]	ΔH_m [J/g]	T_m [°C]	ΔH_m [J/g]
l-PLLA	58	117	45.3	174	45.2	–	–
90/10	56	113	34.5	173	33.2	202	10.2
80/20	55	99	25.8	169	24.5	204	20.4
70/30	53	100	11.1	162	18.2	205	28.6
50/50	54	–	–	–	–	206	54.3

an increase in the *mb*PDLA501 contents. The heat of fusion (ΔH_m) values also exhibit a similar trend, reflecting lower quality and contents of homo-crystallite, and vice versa for the stereocomplex. Single T_g is also observed in all blend samples, which decreases with an increase in the *mb*PDLA501 contents, reflecting a complete miscibility at all compositions. ΔH_c values of *l*-PLLA-rich blends are similar to that of ΔH_m values, also indicating that a cold crystallization mainly corresponds to homo-crystallite formation, whereas the stereocomplex is generated very fast during the melt crystallization.

3.3. Mechanical properties of *l*-PLLA/*mb*PDLA stereocomplex blends

Mechanical properties of the stereocomplex blends are evaluated in terms of tensile strength, modulus, and elongation at break, in which examples of stress-strain curves (4 replicates) of a *l*-PLLA/*mb*PDLA101 blend (90/10) are shown in Figure 7. Toughness is calculated from the area under the curves, which only represent the samples behaviors at low deformation rates, but not impact toughness. Table 5 summarizes mechanical properties of blends containing *mb*PDLA101, as a function of the

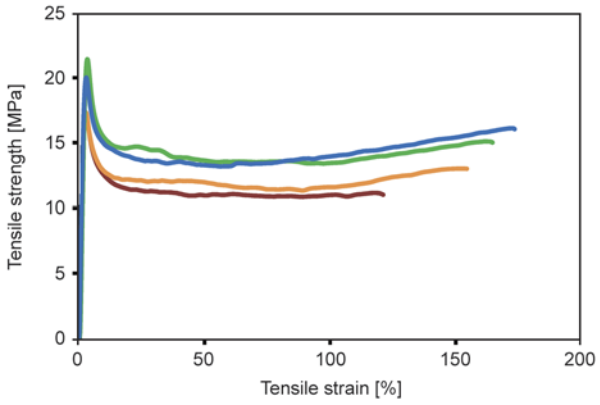

Figure 7. Stress-strain curves of *l*-PLLA/*mb*PDLA101 stereocomplex blend at a 90/10 composition (4 replicates)

Table 5. Mechanical properties of *l*-PLLA/*mb*PDLA101 stereocomplex blends, as a function of blend ratios

Blend ratios	Tensile strength [MPa]	Young's modulus [MPa]	Elongation at break [%]	Toughness [mJ/mm^3]
100/0	22.4±1.3	1269±69	13.8±2.1	1.7±0.5
95/5	17.2±1.6	1065±131	16.9±3.2	1.7±0.6
90/10	19.8±2.4	1134±58	144.9±29.1	19.0±5.1
80/20	18.2±2.1	1004±99	13.1±4.1	1.4±0.6
70/30	17.7±0.9	964±41	16.2±1.0	1.9±0.4

Table 6. Mechanical properties of *l*-PLLA and *l*-PLLA/*mb*PDLA (90/10) stereocomplex blends consisting of different *mb*PDLAs

Blend component	Tensile strength [MPa]	Young's modulus [MPa]	Elongation at break [%]	Toughness [mJ/mm^3]
l-PLLA	22.4±1.3	1269±69	13.8±2.1	1.7±0.5
*mb*PDLA051	16.9±1.0	998±83	63.4±22.1	8.6±2.9
*mb*PDLA101	19.8±2.4	1134±58	144.9±29.1	19.0±5.1
*mb*PDLA201	32.1±2.2	1120±62	76.3±17.0	13.3±2.8
*mb*PDLA501	30.3±0.9	1631±189	97.7±28.4	26.1±7.7

blend contents. Slight decreases in all properties are observed with an inclusion of *mb*PDLA101, except those of the 90/10 blend, whose elongation at break and toughness are largely increased without sacrificing much of the tensile strength and modulus. This reflects a strong influence of an optimum blend ratio on the improvement of the blends mechanical properties.

Enhancements in tensile strength and modulus of the blends are also feasible by varying *mb*PDLAs sizes. Table 6 summarizes mechanical properties of stereocomplex blends of different *mb*PDLAs, prepared at the same composition (90/10). The blend consisting of *mb*PDLA501 exhibits higher tensile strength and modulus than those of *l*-PLLA, whereas those of smaller *mb*PDLAs show slight drops in the values. This reflects that a critical molecular weight value of *mb*PDLA is required in the formation of appropriate stereocomplex structure, which in turns imposes a large influence on the enhancement of their mechanical properties.

3.4. Rheological properties of *l*-PLLA/*mb*PDLA stereocomplex blends

Rheology behaviors of stereocomplex blends containing different *mb*PDLAs, prepared at a 90/10 ratio, are examined at a fixed strain of 5%. Figure 8 shows results on complex viscosity (η*), storage modulus (G'), loss modulus (G''), and tan δ of the

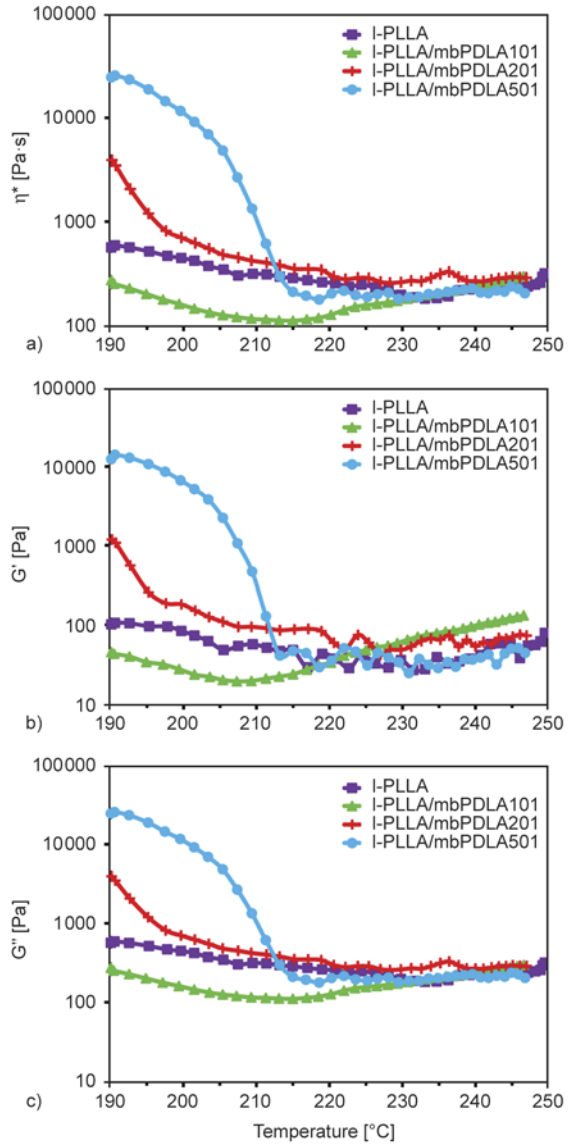

Figure 8. Temperature dependence of complex viscosity (η*) (a), storage moduli (G') (b) and loss moduli (G'') (c) of stereocomplex blends containing different *mb*PDLAs

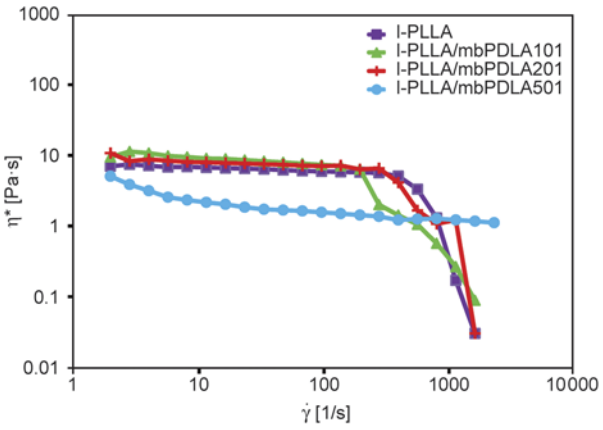

Figure 9. Steady shear viscosity of stereocomplex blends containing different *mb*PDLAs at a 90:10 blend composition

blends, as a function of temperature. At temperatures below their stereocomplex's T_m, the blends consisting of *mb*PDLA501 and *mb*PDLA201 show high η*, G' and G'' values, due to the presence of the stereocomplex structure in a glassy state. An incorporation of small-sized *mb*PDLA101 leads to a reduction in the values, compared to *l*-PLLA, as this acts as a plasticizer. When the chain length of *mb*PDLAs increases, the value sharply increases, where an increase of 1 and 2 orders of magnitude is observed in *mb*PDLA201 and *mb*PDLA501, respectively. This reflects a formation of stronger interaction, *i.e.*, hydrogen bonding, between the 2 stereoconstituents [2, 47, 48]. A sharp decrease in the values is observed when the structure melts. This behavior is not seen in blends consisting of smaller *mb*PDLAs, due to the absence (or low content) of stereocomplex structure, as previously discussed.

The steady shear rheology behaviors, as a function of shear rate, of blends containing different *mb*PDLAs (90/10 blend compositions) are shown in Figure 9. The experiments are conducted at 230°C, above T_m of the stereocomplex. Typical non-Newtonian behavior is observed in all samples. At low shear rates, the shear viscosity of stereocomplex blends are comparable to that of *l*-PLLA, except that of *mb*PDLA501, which is about 1 order of magnitude lower. This is due to the influence of its branched component, which possesses the required arm length. At higher shear rates (>200 1/s), the shear thinning behavior is clearly evidenced, except for that of *mb*PDLA501. The results also indicate that this behavior of the blends is observed earlier (at lower shear rates) than that of *l*-PLLA, in which the inclusion of *mb*PDLAs with shorter arm lengths shows a sudden drop in the viscosity at lower rates. Interestingly, the stereocomplex blend of *mb*PDLA501 does not exhibit shear-thinning characteristics in this shear rate range (<10,000 1/s), probably because of its sufficiently-long arm lengths that enable effective chain entanglements, and its strong interaction between the 2 enantiomeric structures. Given its excellent mechanical property, the *l*-PLLA/*mb*PDLA501 blend show high potential for industrial use, as this rheological property also leads to easy processing conditions.

4. Conclusions

Multi-branched PDLAs (*mb*PDLAs) derived from polyglycidol (PG) core are successfully used to

enhance mechanical properties and processing conditions of commercial linear-structured PLLA (*l*-PLLA). Chemical structures of *mb*PDLAs are controlled by adjusting the feed ratio of DLA monomer to the PG macro-initiator, which in turns leads to a variation in the copolymers thermal and physical properties. The *mb*PDLAs structures and blend compositions impose strong effects on physical and mechanical properties, *i.e.*, T_g, T_m, toughness, tensile strength, modulus, and elongation at break, of the *l*-PLLA/*mb*PDLAs stereocomplex blends. The stereocomplex with a blend ratio of 90/10 exhibits the most desirable properties, in which the highest elongation at break value is gained whereas tensile strength and moduli are comparable to *l*-PLLA. The material also exhibits the lowest complex viscosity, which provides easy processing conditions. This is achieved by the incorporation of copolymers with multi-branched structures and an ability to form a much stronger stereocomplex structure.

Acknowledgements

This research is partially supported by a grant of the National Metal and Materials Technology Center, and the National Research Council of Thailand (NRCT). The authors thank PURAC (Netherlands) for the supply of PLLA and DLA samples. W.S. is grateful for a scholarship from the Center of Excellence in Material Science, Construction, and Maintenance Technology, Thammasat University.

References

[1] Dorgan J. R., Lehermeier H., Mang M.: Thermal and rheological properties of commercial-grade poly(lactic acid)s. Journal of Polymers and the Environment, **8**, 1–9 (2000).
DOI: 10.1023/A:1010185910301

[2] Fukushima K., Kimura Y.: Stereocomplexed polylactides (Neo-PLA) as high-performance bio-based polymers: Their formation, properties, and application. Polymer International, **55**, 626–642 (2006).
DOI: 10.1002/pi.2010

[3] Opaprakasit M., Petchsuk A., Opaprakasit P., Chongprakobkit S.: Effects of synthesis conditions on chemical structures and physical properties of copolyesters from lactic acid, ethylene glycol and dimethyl terephthalate. Express Polymer Letters, **3**, 458–468 (2009).
DOI: 10.3144/expresspolymlett.2009.56

[4] Namkajorn M., Petchsuk A., Opaprakasit M., Opaprakasit P.: Synthesis and characterizations of degradable aliphatic-aromatic copolyesters from lactic acid, dimethyl terephthalate and diol: Effects of diol type and monomer feed ratio. Express Polymer Letters, **4**, 415–422 (2010).
DOI: 10.3144/expresspolymlett.2010.52

[5] Opaprakasit M., Kongtong W., Petchsuk A., Opaprakasit P.: Processability enhancement of poly(lactic acid-*co*-ethylene terephthalate) by blending with poly(ethylene-*co*-vinyl acetate), poly(3-hydroxybutyrate-*co*-3-hydroxyvalerate), and poly(butylene succinate). Polymer Bulletin, **67**, 275–290 (2011).
DOI: 10.1007/s00289-010-0421-8

[6] Nguyen T-H., Tangboriboonrat P., Rattanasom N., Petchsuk A., Opaprakasit M., Thammawong C., Opaprakasit P.: Polylactic acid/ethylene glycol triblock copolymer as novel crosslinker for epoxidized natural rubber. Journal of Applied Polymer Science, **124**, 164–174 (2012).
DOI: 10.1002/app.35088

[7] Petchsuk A., Submark W., Opaprakasit P.: Development of crosslinkable poly(lactic acid-*co*-glycidyl methacrylate) copolymers and their curing behaviors. Polymer Journal, **45**, 406–412 (2013).
DOI: 10.1038/pj.2012.159

[8] Lasprilla A. J. R., Martinez G. A. R., Lunelli B. H., Jardini A. L., Filho R. M.: Poly-lactic acid synthesis for application in biomedical devices – A review. Biotechnology Advances, **30**, 321–328 (2012).
DOI: 10.1016/j.biotechadv.2011.06.019

[9] Liu H., Zhang J.: Research progress in toughening modification of poly(lactic acid). Journal of Polymer Science Part B: Polymer Physics, **49**, 1051–1083 (2011).
DOI: 10.1002/polb.22283

[10] Tsuji H.: Poly(lactide) stereocomplexes: Formation, structure, properties, degradation, and applications. Macromolecular Bioscience, **5**, 569–597 (2005).
DOI: 10.1002/mabi.200500062

[11] Zhou H., Lawrence J. G., Bhaduri S. B.: Fabrication aspects of PLA-CaP/PLGA-CaP composites for orthopedic applications: A review. Acta Biomaterialia, **8**, 1999–2016 (2012).
DOI: 10.1016/j.actbio.2012.01.031

[12] Opaprakasit P., Opaprakasit M.: Thermal properties and crystallization behaviors of polylactide and its enantiomeric blends. Macromolecular Symposia, **264**, 113–120 (2008).
DOI: 10.1002/masy.200850418

[13] Avérous L.: Biodegradable multiphase systems based on plasticized starch: A review. Journal of Macromolecular Science Part C: Polymer Reviews, **44**, 231–274 (2004).
DOI: 10.1081/MC-200029326

[14] Datta R., Henry M.: Lactic acid: Recent advances in products, processes and technologies – A review. Journal of Chemical Technology and Biotechnology, **81**, 1119–1129 (2006).
DOI: 10.1002/jctb.1486

[15] Lee S., Lee J. W.: Characterization and processing of biodegradable polymer blends of poly(lactic acid) with poly(butylene succinate adipate). Korea Australia Rheology Journal, **17**, 71–77 (2005).

[16] Ikada Y., Jamshidi K., Tsuji H., Hyon S. H.: Stereocomplex formation between enantiomeric poly(lactides). Macromolecules, **20**, 904–906 (1987).
DOI: 10.1021/ma00170a034

[17] Tsuji H., Ikada Y.: Stereocomplex formation between enantiomeric poly(lactic acid)s. XI. Mechanical properties and morphology of solution-cast films. Polymer, **40**, 6699–6708 (1999).
DOI: 10.1016/S0032-3861(99)00004-X

[18] Purnama P., Kim S. H.: Stereocomplex formation of high-molecular-weight polylactide using supercritical fluid. Macromolecules, **43**, 1137–1142 (2010).
DOI: 10.1021/ma902536p

[19] Purnama P., Kim S. H.: Stereocomplex formation of polylactide using microwave irradiation. Polymer International, **63**, 741–745 (2014).
DOI: 10.1002/pi.4581

[20] Arikawa Y., Serizawa T., Mukose T., Kimura Y., Akashi M.: Characterization of poly(lactide)s nanotubes consist of poly(lactide)s stereocomplex hollow particles. in '55th Society of Polymer Science Japan Symposium on Macromolecules' Toyama, Japan, vol 55, 4040–4046 (2006).

[21] Kim S. H., Tan J. P. K., Nederberg F., Fukushima K., Yang Y. Y., Waymouth R. M., Hedrick J. L.: Mixed micelle formation through stereocomplexation between enantiomeric poly(lactide) block copolymers. Macromolecules, **42**, 25–29 (2009).
DOI: 10.1021/ma801739x

[22] Kondo K., Kida T., Ogawa Y., Arikawa Y., Akashi M.: Nanotube formation through the continuous one-dimensional fusion of hollow nanocapsules composed of layer-by-layer poly(lactic acid) stereocomplex films. Journal of the American Chemical Society, **132**, 8236–8237 (2010).
DOI: 10.1021/ja1020537

[23] Brizzolara D., Cantow H-J., Diederichs K., Keller E., Domb A. J.: Mechanism of the stereocomplex formation between enantiomeric poly(lactide)s. Macromolecules, **29**, 191–197 (1996).
DOI: 10.1021/ma951144e

[24] Fukushima K., Chang Y-H., Kimura Y.: Enhanced stereocomplex formation of poly(L-lactic acid) and poly (D-lactic acid) in the presence of stereoblock poly(lactic acid). Macromolecular Bioscience, **7**, 829–835 (2007).
DOI: 10.1002/mabi.200700028

[25] Takasaki M., Ito H., Kikutani T.: Development of stereocomplex crystal of polylactide in high-speed melt spinning and subsequent drawing and annealing processes. Journal of Macromolecular Science Part B: Physics, **42** B, 403–420 (2003).
DOI: 10.1081/MB-120021570

[26] Zhang J., Sato H., Tsuji H., Noda I., Ozaki Y.: Infrared spectroscopic study of $CH_3\cdots O{=}C$ Interaction during poly(L-lactide)/poly(D-lactide) stereocomplex formation. Macromolecules, **38**, 1822–1828 (2005).
DOI: 10.1021/ma047872w

[27] Zhang J., Tashiro K., Tsuji H., Domb A. J.: Investigation of phase transitional behavior of poly(L-lactide)/poly(D-lactide) blend used to prepare the highly-oriented stereocomplex. Macromolecules, **40**, 1049–1054 (2007).
DOI: 10.1021/ma061693s

[28] Fukushima K., Hirata M., Kimura Y.: Synthesis and characterization of stereoblock poly(lactic acid)s with nonequivalent D/L sequence ratios. Macromolecules, **40**, 3049–3055 (2007).
DOI: 10.1021/ma070156k

[29] Fukushima K., Kimura Y.: A novel synthetic approach to stereo-block poly(lactic acid). Macromolecular Symposia, **224**, 133–143 (2005).
DOI: 10.1002/masy.200550612

[30] Yui N., Dijkstra P. J., Feijen J.: Stereo block copolymers of L- and D-lactides. Die Makromolekulare Chemie, **191**, 481–488 (1990).
DOI: 10.1002/macp.1990.021910303

[31] Hirata M., Kimura Y.: Thermomechanical properties of stereoblock poly(lactic acid)s with different PLLA/PDLA block compositions. Polymer, **49**, 2656–2661 (2008).
DOI: 10.1016/j.polymer.2008.04.014

[32] Quynh T. M., Mitomo H., Yoneyama M., Hien N. Q.: Properties of radiation-induced crosslinking stereocomplexes derived from poly(L-lactide) and different poly(D-lactide). Polymer Engineering and Science, **49**, 970–976 (2009).
DOI: 10.1002/pen.21309

[33] Seiler M.: Hyperbranched polymers: Phase behavior and new applications in the field of chemical engineering. Fluid Phase Equilibria, **241**, 155–174 (2006).
DOI: 10.1016/j.fluid.2005.12.042

[34] Liu J., Lou L., Yu W., Liao R., Li R., Zhou C.: Long chain branching polylactide: Structures and properties. Polymer, **51**, 5186–5197 (2010).
DOI: 10.1016/j.polymer.2010.09.002

[35] Numata K., Srivastava R. K., Finne-Wistrand A., Albertsson A-C., Doi Y., Abe H.: Branched poly(lactide) synthesized by enzymatic polymerization: Effects of molecular branches and stereochemistry on enzymatic degradation and alkaline hydrolysis. Biomacromolecules, **8**, 3115–3125 (2007).
DOI: 10.1021/bm700537x

[36] Shao J., Sun J., Bian X., Cui Y., Li G., Chen X.: Investigation of poly(lactide) stereocomplexes: 3-armed poly(L-lactide) blended with linear and 3-armed enantiomers. Journal of Physical Chemistry B, **116**, 9983–9991 (2012).
DOI: 10.1021/jp303402j

[37] Andersson S. R., Hakkarainen M., Inkinen S., Södergård A., Albertsson A-C.: Customizing the hydrolytic degradation rate of stereocomplex PLA through different PDLA architectures. Biomacromolecules, **13**, 1212–1222 (2012).
DOI: 10.1021/bm300196h

[38] Inkinen S., Stolt M., Södergård A.: Effect of blending ratio and oligomer structure on the thermal transitions of stereocomplexes consisting of a D-lactic acid oligomer and poly(L-lactide). Polymers for Advanced Technologies, **22**, 1658–1664 (2011).
DOI: 10.1002/pat.1654

[39] Gottschalk C., Wolf F., Frey H.: Multi-arm star poly(L-lactide) with hyperbranched polyglycerol core. Macromolecular Chemistry and Physics, **208**, 1657–1665 (2007).
DOI: 10.1002/macp.200700168

[40] Ouchi T., Ichimura S., Ohya Y.: Synthesis of branched poly(lactide) using polyglycidol and thermal, mechanical properties of its solution-cast film. Polymer, **47**, 429–434 (2006).
DOI: 10.1016/j.polymer.2005.11.039

[41] Kainthan R. K., Muliawan E. B., Hatzikiriakos S. G., Brooks D. E.: Synthesis, characterization, and viscoelastic properties of high molecular weight hyperbranched polyglycerols. Macromolecules, **39**, 7708–7717 (2006).
DOI: 10.1021/ma0613483

[42] Sunder A., Hanselmann R., Frey H., Mülhaupt R.: Controlled synthesis of hyperbranched polyglycerols by ring-opening multibranching polymerization. Macromolecules, **32**, 4240–4246 (1999).
DOI: 10.1021/ma990090w

[43] Tokar R., Kubisa P., Penczek S., Dworak A.: Cationic polymerization of glycidol: Coexistence of the activated monomer and active chain end mechanism. Macromolecules, **27**, 320–322 (1994).
DOI: 10.1021/ma00080a002

[44] Vandenberg E. J.: Polymerization of glycidol and its derivatives: A new rearrangement polymerization. Journal of Polymer Science: Polymer Chemistry Edition, **23**, 915–949 (1985).
DOI: 10.1002/pol.1985.170230401

[45] Schmidt S. C., Hillmyer M. A.: Polylactide stereocomplex crystallites as nucleating agents for isotactic polylactide. Journal of Polymer Science Part B: Polymer Physics, **39**, 300–313 (2001).
DOI: 10.1002/1099-0488(20010201)39:3<300::AID-POLB1002>3.0.CO;2-M

[46] Tsuji H., Takai H., Saha S. K.: Isothermal and non-isothermal crystallization behavior of poly(L-lactic acid): Effects of stereocomplex as nucleating agent. Polymer, **47**, 3826–3837 (2006).
DOI: 10.1016/j.polymer.2006.03.074

[47] Opaprakasit P., Opaprakasit M., Tangboriboonrat P.: Crystallization of polylactide and its stereocomplex investigated by two-dimensional Fourier transform infrared correlation spectroscopy employing carbonyl overtones. Applied Spectroscopy, **61**, 1352–1358 (2007).
DOI: 10.1366/000370207783292235

[48] Zhang J., Sato H., Tsuji H., Noda I., Ozaki Y.: Differences in the $CH_3\cdots O{=}C$ interactions among poly(L-lactide), poly(L-lactide)/poly(D-lactide) stereocomplex, and poly(3-hydroxybutyrate) studied by infrared spectroscopy. Journal of Molecular Structure, **735–736**, 249–257 (2005).
DOI: 10.1016/j.molstruc.2004.11.033